Simultaneous Inversion of 3D Velocity Structure, Hypocenter Locations, and Reflector Geometry in Cascadia

Leiph Alexander Preston

A dissertation submitted in partial fulfillment of the
requirements for the degree of

Doctor of Philosophy

University of Washington

2003

Program Authorized to Offer Degree: Department of Earth and Space Sciences

UMI Number: 3111122

INFORMATION TO USERS

The quality of this reproduction is dependent upon the quality of the copy submitted. Broken or indistinct print, colored or poor quality illustrations and photographs, print bleed-through, substandard margins, and improper alignment can adversely affect reproduction.

In the unlikely event that the author did not send a complete manuscript and there are missing pages, these will be noted. Also, if unauthorized copyright material had to be removed, a note will indicate the deletion.

UMI®

UMI Microform 3111122

In presenting this dissertation in partial fulfillment of the requirements for the Doctoral degree at the University of Washington, I agree that the Library shall make its copies freely available for inspection. I further agree that extensive copying of the dissertation is allowable only for scholarly purposes, consistent with "fair use" as prescribed in U.S. Copyright Law. Requests for copying or reproduction of this dissertation may be referred to Proquest Information and Learning, 300 North Zeeb Road, Ann Arbor, MI 48106-1346, to whom the author has granted "the right to reproduce and sell (a) copies of the manuscript in microform and/or (b) printed copies of the manuscipt made from microform."

Signature_____

Date____10/3/03_____

University of Washington

Graduate School

This is to certify that I have examined this copy of a doctoral dissertation by
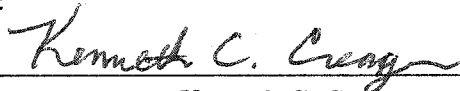
Leiph Alexander Preston

and have found that it is complete and satisfactory in all respects,
and that any and all revisions required by the final
examining committee have been made.
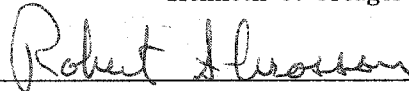
Chair of Supervisory Committee:
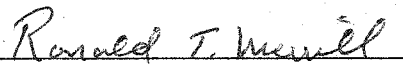
_____
Kenneth C. Creager

Reading Committee:

_____
Kenneth C. Creager

_____
Robert S. Crosson

_____
Ronald T. Merrill

Date: Oct, 1, 2003

University of Washington

Abstract

Simultaneous Inversion of 3D Velocity Structure, Hypocenter Locations, and Reflector
Geometry in Cascadia

Leiph Alexander Preston

Chair of the Supervisory Committee:
Professor Kenneth C. Creager
Department of Earth and Space Sciences

We develop and apply a non-linear inversion of direct and wide-angle reflection travel times
for 3-D P-wave velocity structure, earthquake hypocenters, and reflector geometry under
NW Washington focusing on the structure of the subducting Juan de Fuca plate. The
first-arrival travel times are derived from both active-source experiments and from local
earthquakes. The reflection arrivals were picked from data collected during the 1998 Wet
SHIPS active-source experiment, which consisted of air-gun sources within the inland water-
ways of NW Washington and SW British Columbia to land-based stations. Our inversion
procedure reduces the well-known trade-off between reflector position and the velocities
above it by the combination of simultaneous inversion and adequate crossing paths. We
interpret the wide-angle reflector as the Moho of the subducting Juan de Fuca slab. The
relocated intraslab earthquakes separate into two groups: those located up-dip of the 45km
reflector depth contour generally lie below the reflector in material whose velocity exceeds
7.7km/s, placing them within the subducting mantle, while those down-dip of this contour
occur within material whose velocities are 6.8–7.5km/s, placing them within subducted
oceanic crust. We interpret these groups of earthquakes as resulting from serpentine dehy-
dration in the subducted mantle and the basalt to eclogite transformation in the subducted
crust. We have performed velocity checkerboard, slab velocity resolution, and parameter
sensitivity tests to estimate our ability to resolve the relationship among the reflector, in-
traslab hypocenters, and slab velocity structure. These tests indicate we have the necessary

resolvability and can distinguish the relative locations among the velocities, reflector, and intraslab hypocenters within the subducting slab to $\pm 2km$. The occurrence of events within the subducted mantle geometrically allows for larger magnitude earthquakes than could occur if they were confined to the oceanic crust. Additionally, the large amplitude of the reflected arrivals relative to direct arrivals suggests that slab reflections should be included in strong ground motion studies. The release of fluids attendant with the basalt to eclogite transformation have observable consequences which may be related to recent discoveries of slow slip events, tremor events, and a serpentinized mantle wedge.

Contents

List of Figures

viii

List of Tables

Acknowledgments

This dissertation would not have been possible except through the help of many people. I would like to especially thank my research adviser, Ken Creager, for all of his time, energy, patience, and talent that he has awarded me with over the years here as a graduate student. His guidance has and will prove invaluable. I would also like to thank Bob Crosson for his insightful conversations and experience, Tom Pratt for all those hours spent up at IRIS teaching me the ways of reflection seismology, and Ron Merrill, Anne Trehu and Tom Jarboe for making this possible. Ron Merrill's understanding and ability to teach his understanding of complex geophysical problems will always be an inspiration for me.

In addition, I would like to thank Neill Symons for providing the tomography code, the foundation for this work. Also, I thank all the many people who made the SHIPS experiments possible, including M. A. Fischer, T. Parsons, R. A. Hyndman, K. C. Miller, C. N. Snelson, D. C. Mosher, T. L. Pratt, R. Ramachandran, G. D. Spence, U. S. ten Brink, C. S. Weaver, and B. C. Zelt. Serious and not-so-serious discussions with fellow students and friends Guy Medema, Tom van Wagoner, Qing Xu, and Ares Ouzounis also proved very helpful.

My mom and grandparents are also very dear to me and without their support and love over the years, none of this would be possible. And last, but certainly not least, I thank my wife, Sonya, for her patience, love, support and understanding through this sometimes very tiring and stressful time.

Chapter 1

Introduction

On February 28, 2001, the magnitude 6.8 Nisqually earthquake shook western Washington from a depth of more than 50km within the subducting Juan de Fuca plate. Although fortunately causing comparatively little damage itself, the Nisqually event is only one of several damaging intraslab earthquakes that have struck western Washington in the past 150 years since historical records have been kept. Due to the obvious seismic hazard these earthquakes pose to the heavily populated Puget Sound region, a firm understanding of the processes that cause these events is necessary to form a sound seismic hazards policy within the region. As a consequence of their depth, standard explanations as to their cause, based on shallow seismicity, break down. Dehydration embrittlement, which asserts that volatiles released during metamorphic dehydration reactions reduce the effective normal stress across faults allowing slip, is a leading hypothesis that explains the cause of intraslab seismicity generally less than 150km depth. One of the main purposes of this study is to help elucidate the physical mechanisms responsible for intraslab earthquakes through a model we have produced from a simultaneous inversion for 3-D P-wave velocity structure, hypocenter locations, and wide-angle slab-derived reflector geometry. Accordingly, our primary goal from the modeling perspective is to determine the precise interrelationship among the slab wave speeds, intraslab earthquakes, and the reflector position, i.e. where within the subducting plate are the intraslab events occurring — within the subducted crust or mantle or both.

We combine first-arrival travel-time data from four active-source experiments and from hand-picked local earthquakes with secondary-arrival travel times, consistent in travel time and slowness with wide-angle reflections from the subducting Juan de Fuca slab, to solve for 3-D velocity structure, earthquake hypocentral locations, and reflector geometry (Chapter 2). We find that the intraslab earthquakes separate into two groups based on the depth of the reflector. Events which lie up-dip of the 45km reflector depth contour occur at or below the reflector, while those that lie down-dip of this contour primarily occur at or above the reflector (Chapter 3). We interpret the reflector as the subducted oceanic Moho, placing the up-dip events within the subducted mantle, consistent with serpentine dehydration, and the down-dip events within the subducted oceanic crust, consistent with the basalt to eclogite dehydration reaction (Chapter 5). Our interpretations require precise knowledge of the interrelationship among the velocities, intraslab earthquakes, and reflector. We perform standard velocity checkerboard tests as well as more specific hypothesis tests to investigate this interrelationship (Chapter 4). These tests reveal that we have the necessary velocity resolvability in the slab and that we can resolve the relative locations between the reflector and intraslab earthquakes to about ±2km.

1.1 Intraslab Earthquake Hazards

Due to the absence of megathrust events in the written record in Cascadia, it is not surprising that intraslab events have caused the greatest seismic damage here thus far. However, even in areas that have experienced great megathrust events, intraslab events have often been more damaging, despite their generally smaller seismic moment magnitude (M_0), especially in the western hemisphere [Kirby, 1999]. For example, in Peru in 1970 a $M_w 7.9$ intraslab earthquake killed 50,000 people mainly from a landslide triggered by the earthquake, whereas a nearby M7.5 megathrust earthquake killed 250 in 1940. Likewise, a M7.7 Chilean intraslab event in 1939 killed nearly 28,000, while the largest historically recorded earthquake, a $M_w 9.5$ Chilean megathrust event in 1960, killed 2231 inhabitants.

So why do intraslab events often cause more damage than equivalent or larger magnitude

megathrust events on the same subduction zone? One reason is simply due to where intraslab events occur relative to megathrusts. Megathrust earthquakes occur on the interface between the down-going oceanic lithosphere and the overriding plate. The rupture zone is typically offshore away from human habitation. In contrast, intraslab events occur deeper within the subducting plate, placing them directly underneath population centers. Secondly, *Choy and Boatwright* [1995] and *Choy et al.* [2001] found that intraslab events often have larger seismic energy to moment ratios than megathrust events. Since the seismic energy released during an earthquake is more directly related to ground shaking, and thus damage, than moment, which is a measure of total slip on a fault, this could additionally explain the apparent incongruence. Although not true for all subduction zones, Cascadia exhibits a third cause for increased seismic hazard from intraslab events: intraslab events occur on time scales of one major event every few decades, whereas no interplate thrust has occurred in the 150 years records have been kept in the region. Indeed, paleoseismic studies indicate the last megathrust in Cascadia occurred in the year 1700 with a recurrence interval on the order of 300–600 years [*Atwater and Hemphill*, 1997; *Satake et al.*, 1996]. For more information, the processes and hazards associated with intraslab earthquakes in Cascadia and similar subduction zones are examined in a collection of papers edited by *Kirby et al.* [2002].

1.2 Juan de Fuca Plate

The Juan de Fuca plate is the largest of three microplates that comprise the Cascadia subduction system (Figure 1.1). It is subducting on average at ~40 mm/yr in approximately a northeastward direction (N55°E), with subduction velocity increasing from the south to north [*Wilson*, 2002]. Along the Washington and Oregon coast, subduction is oblique, but a 35° bend in the deformation front causes near normal subduction along the coast of SW British Columbia. The plates that comprise the Cascadia subduction system are some of the youngest, and thus warmest, plates in the world, being about 10 Ma upon subduction (Figure 1.2). The plate age upon subduction is nearly constant along the coast
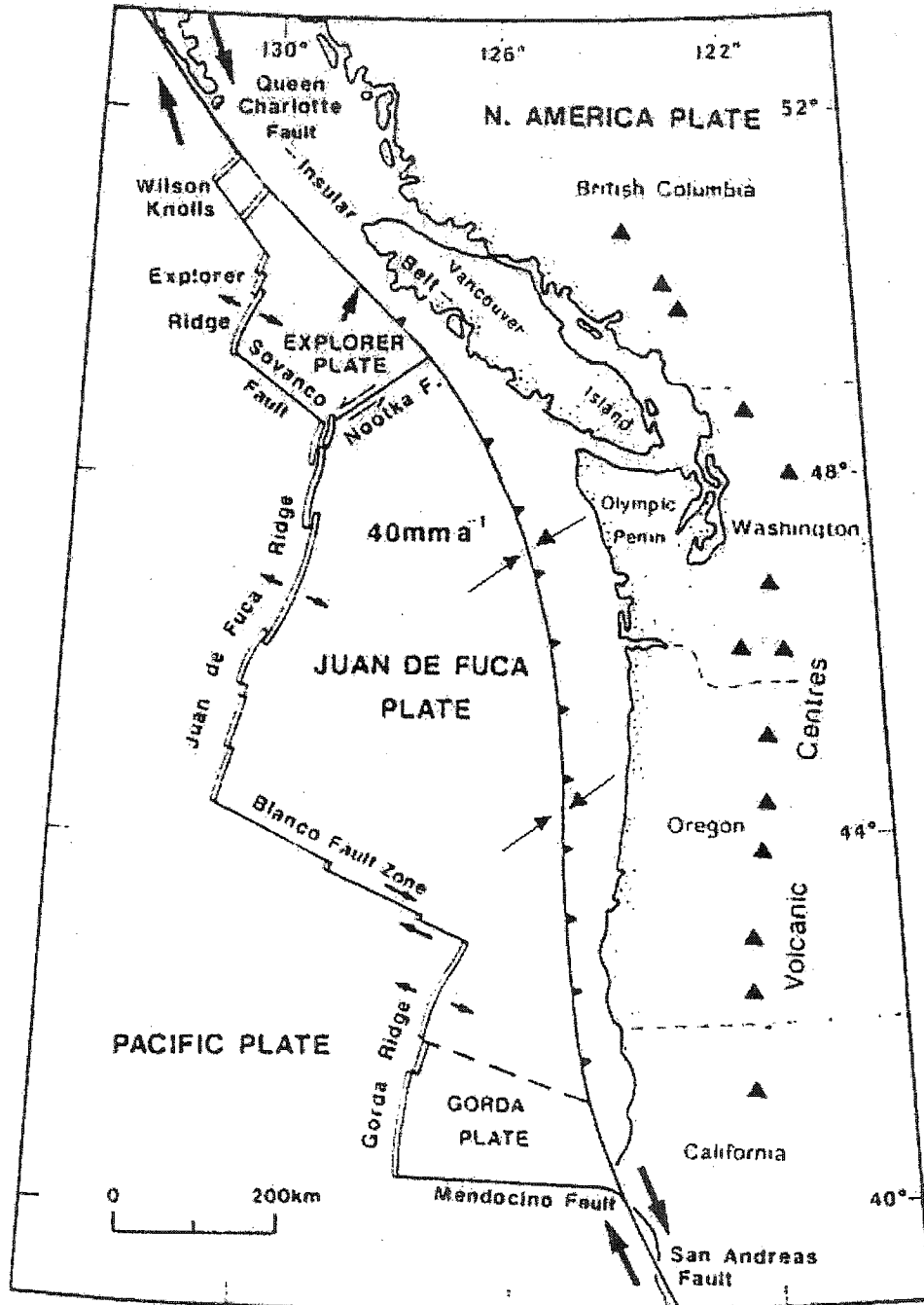
Figure 1.1: Tectonic map of Cascadia. Modified from *Dragert et al.* [1994].
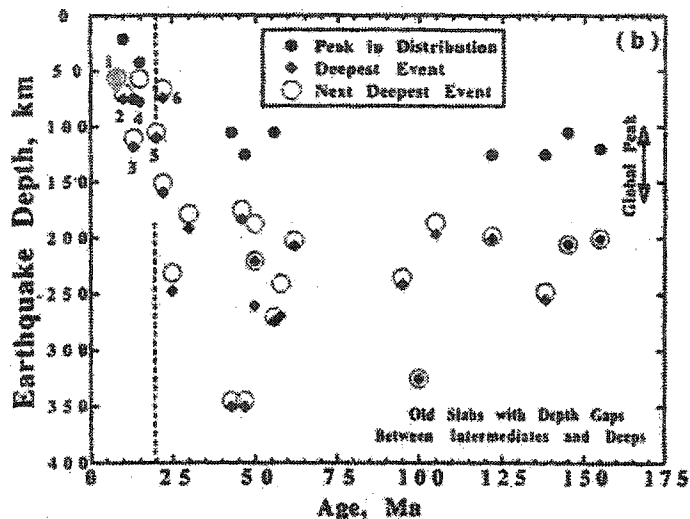
Figure 1.2: Cascadia (grey) plate age vs. maximum intraslab earthquake depth in comparison to other subduction zones. 1: Cascadia; 2: S Chile; 3: S. Mexico; 4: Ecuador; 5: Luzon; 6: SW Japan. Modified from *Kirby et al.* [1996].

of Washington and northern Oregon, but decreases in age both in southern Oregon and along Vancouver Island [*Wilson*, 2002].

1.3   Cascadia Intraslab Earthquakes

Intraslab earthquakes extend down to about 60km depth in most regions of Cascadia [*Ludwin et al.*, 1991] (Figure 1.3), consistent with other warm subduction zones (Figure 1.2). Seismicity rates reveal three general provinces: under the Olympic Peninsula, SW British Columbia, and Oregon. Under the Olympic Peninsula, seismicity rates are relatively high but limited in magnitude during the past 30 years to <M5. This province is bounded on the north and south by regions of higher moment release. The southern boundary forms a lineament of seismicity aligned approximately parallel to the relative plate motion direction (Figure 1.3) and contains the largest magnitude events including the M7.1 1949 Olympia, M6.5 1965 SeaTac, M_w5.8 1999 Satsop, and the most recent M_w6.8 2001 Nisqually events. These large events occur at the base of the smaller neighboring seismicity (Figure 1.4),
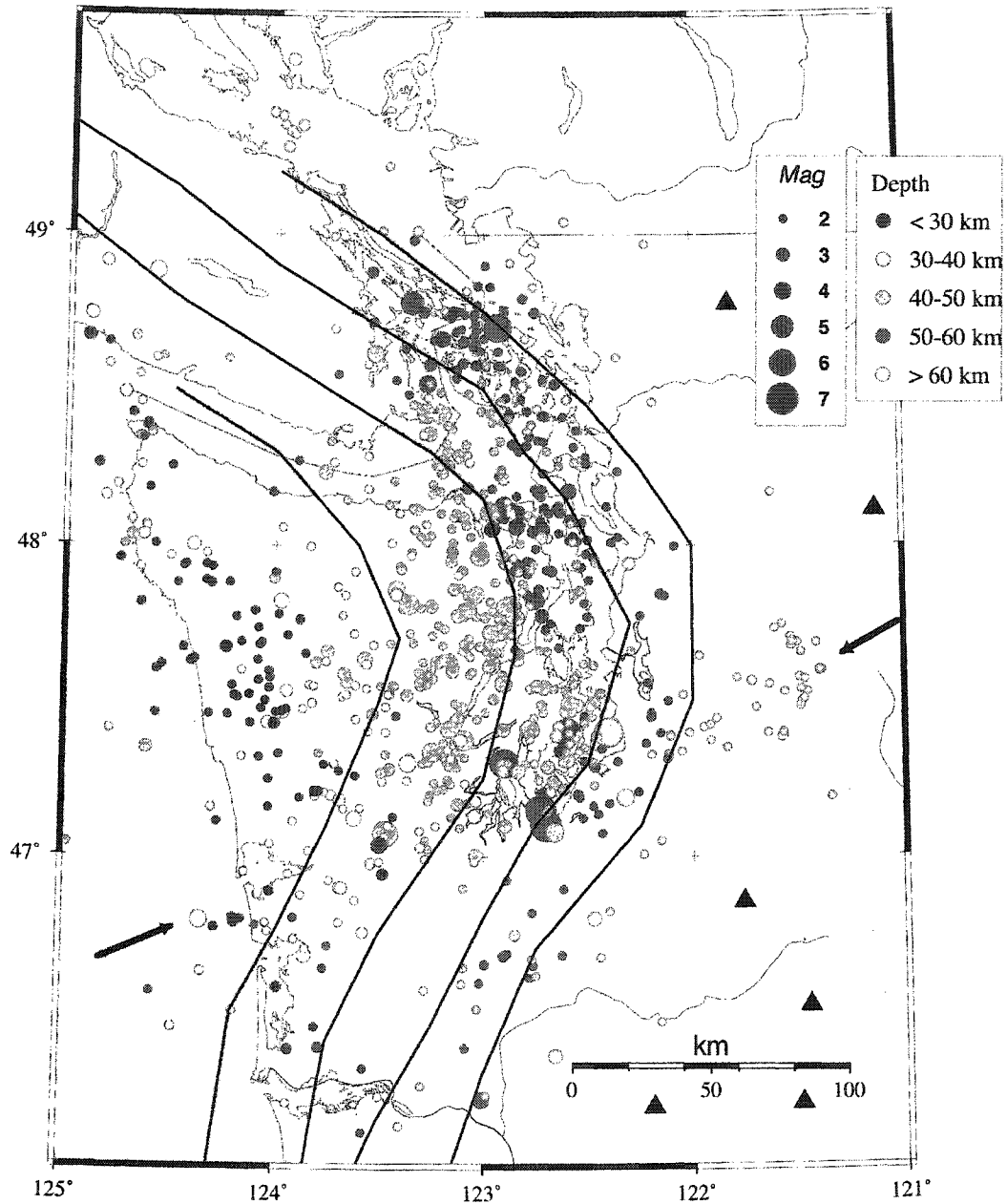
Figure 1.3: Catalog intraslab hypocenters (coded by depth bins and magnitude) and slab contours compiled from *Crosson and Owens* [1987]. Arrows de-mark the seismic lineament which contains the largest and deepest events in Cascadia.
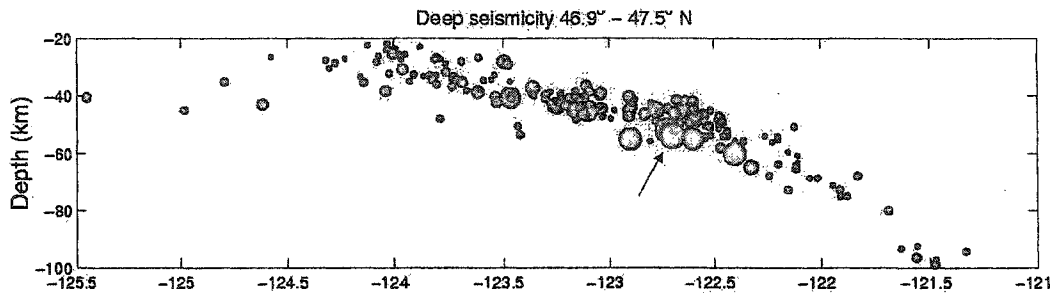
Figure 1.4: Cross-section of Pacific Northwest Seismograph Network catalog intraslab events between 46.9°N and 47.5°N. Event magnitude is indicated by the size of the circle. Note that the largest events, including the 2001 M6.8 Nisqually event (arrow), lie at the base of the microseismicity.

suggesting that these events may be controlled by a different mechanism than the smaller events. Besides containing the largest events, this lineament also contains the very deepest events in Cascadia down to ~100km depth [*Ludwin et al.*, 1991]. South of this lineament, seismicity rates decrease dramatically into SW Washington, nearly vanishing in Oregon. To the north into British Columbia, the seismicity rate drops off compared to the Olympic Peninsula. Unlike under the Olympics, where the intraslab seismicity forms a continuous band from about 25km to 60km depth, in British Columbia the intraslab seismicity splits into two distinct bands: a shallow up-dip band of relatively poorly located offshore but very active seismicity and a deeper down-dip band separated by a region of relative quiescence [*Rogers et al.*, 1990] (Figure 1.5).

Several questions concerning the intraslab events arise from these observations. Why are seismicity rates under the Olympic Peninsula so high? What causes the seismic lineament which contains the largest events? Why are the large events so localized spatially and does this mean we should not worry about large events occurring outside these regions? Why are the largest events at the base of the microseismicity? Why do virtually no events occur under Oregon? Should we expect this pattern to continue or should we prepare for large events there? What is the meaning of the split in seismicity into bands in British Columbia? We do not propose to answer all these questions in this work, but hope to at least provide
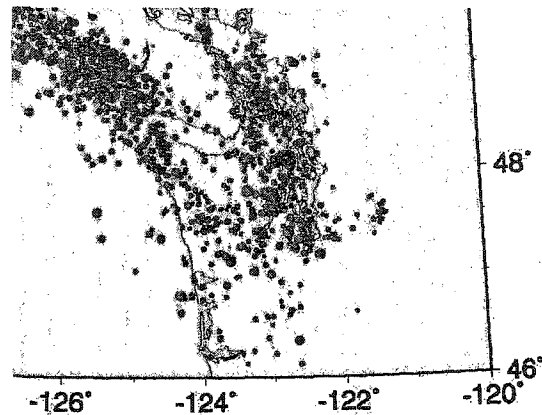
Figure 1.5: Distribution of northern Cascadia intraslab earthquakes compiled from the Geological Survey of Canada and the Pacific Northwest Seismograph Network. From *Rogers and Crosson* [2002].

some partial answers to these questions and build onto the base of knowledge necessary for eventual understanding of intraslab earthquakes.

1.3.1 Previous Studies

Several studies of intraslab seismicity and their relation to the subducting lithosphere have been conducted in northern Cascadia, but unfortunately they lead to equivocal interpretations. Slab contours (Figure 1.3) were compiled from receiver function studies and intraslab hypocenter depths and demonstrate a clear up-warp of the subducting lithosphere under the Olympics approximately coincident with the high seismicity rates [*Crosson and Owens*, 1987]. Intraslab earthquake focal mechanisms are widely scattered but generally demonstrate in-plane tension [*Ma et al.*, 1996]. Unfortunately, lack of precise depth control in these studies makes interpretation of the relationship between the seismicity and slab unclear. Under southwest Washington, *Parsons et al.* [1998] interpreted intraslab seismicity as occurring within the subducted mantle from results of a 2-D E-W active-source experiment, albeit using network hypocenter locations. Results from the deepest band of seismicity in Canada from a receiver function study and double difference relative relocations place the intraslab earthquakes primarily in the subducted crust with the largest events clearly oc-

curring in the subducted mantle [*Cassidy and Ellis*, 1993; *Cassidy and Waldhauser*, 2002].

1.4 Why This Work is Needed

Although excellent tomographic studies of the shallow structure in western Washington have been completed [*Symons*, 1998; *Brocher et al.*, 2001; *van Wagoner et al.*, 2002], the deep structure has yet to be properly explored. From a seismic hazards perspective, the intraslab earthquakes within Cascadia cannot afford to be ignored. The 1998 Wet SHIPS (Seismic Hazards Investigation in Puget Sound) offered an exceptional opportunity to study in detail the structure under NW Washington and SW British Columbia with multiple criss-crossing paths. The addition of high-quality local earthquake travel times to the active source data extends our view to include the deep structure in Western Washington down to 60km depth. Supplementing this rich data set, we have also collected data from wide-angle reflections off the subducting Juan de Fuca plate, allowing precise location of the slab relative to the velocity structure and earthquakes in the slab. To accomplish this synthesis of active-source, earthquake and reflection data, we have developed a new method for simultaneously inverting these data for our fully 3-D structural model of Western Washington. This diverse and rich data set and simultaneous inversion procedure permit us to gain an unprecedented view of the shallow structure of an active subduction system and to further our understanding of the processes that control intraslab earthquake nucleation.

Chapter 2

Method

We have developed a method of incorporating travel times of first arrivals from earthquake and man-made sources as well as times of reflected waves in a self-consistent simultaneous inversion procedure. 3-D velocity structure is constrained along ray paths of first arrivals [e.g. *Thurber*, 1992] and reflected waves. Earthquake locations and the reflector geometry are relocated according to the local spatial time derivatives and regularization constraints. The model consists of three components: 3-D slowness structure, earthquake locations (space and time), and reflector geometry. The slowness structure is constrained to be a smooth continuous function of position, parameterized by a 3-D grid with 4km horizontal and 2km vertical node spacing. Earthquake locations consist of latitude, longitude, depth and origin time with a weak stabilization constraint minimizing relocations. The reflector geometry is constrained to be a smooth, continuous 2-D function of position, parameterized by a 2-D grid of depth values with 4km node spacing. Tri-linear interpolation of the model is used for the purposes of the finite-difference travel-time [*Vidale*, 1990; *Hole and Zelt*, 1995] and 3-D ray-path calculations. Travel times from first and reflected arrivals are simultaneously inverted to minimize the misfit to the observed values and regularization constraints. This procedure is non-linear because ray paths depend on model parameters, but stably converges after about 10 iterations. The active-source experiments provide good constraint on the upper crust, where velocity variations are large, while earthquakes at a variety of depths constrain deeper structure if upper crustal structure is well known. The advantage of this method is that in areas well constrained by first arrivals where velocities

are well determined, it allows for better absolute placement of the reflector. Conversely, in areas poorly constrained by first arrivals, reflected ray paths can help constrain the velocity.

2.1 Data

2.1.1 First Arrivals

First-arrival travel times are derived from earthquakes and active sources. The active source data consist of 2100 travel-time picks from the 1991 Western Cascade Line [*Miller et al.*, 1997], 5000 from the 1995 onshore-offshore SW Washington experiment [*Parsons et al.*, 1998], 80,500 from the 1998 Wet SHIPS experiment [*Brocher et al.*, 1999, 2001; *van Wagoner et al.*, 2002; *Trehu et al.*, 2002; *Ramachandran*, 2001], and 3600 from the 1999 Dry SHIPS experiment [*Brocher et al.*, 2000] (Figure 2.1). The bulk of the first-arrival travel times and all of the reflection travel times are derived from the 1998 Wet SHIPS experiment. This experiment consisted of about 30,000 marine airgun sources (6500 in^3 total volume per shot) with 100m spacing, conducted within the inland waterways of NW Washington and SW British Columbia, and over 200 land-based stations ($\sim$20km spacing), designed principally to explore the shallow tectonic structure and its associated hazards. Well over 1,000,000 travel times have been picked [*Brocher et al.*, 2001] from this experiment. Nearly 90% of the direct-arrival data have error estimates of 0.05s. However, error estimates are as low as 0.01s and as high as 0.8s, but only 14 observations have errors estimated $>$0.2s.

Earthquakes incorporated in this study consist of a high-quality, manually picked subset of the regional Pacific Northwest Seismograph Network (PNSN) that were primarily analyzed by Neill Symons [*Symons*, 1998] and supplemented by Tom van Wagoner [*van Wagoner et al.*, 2002]. Earthquakes were selected to minimize redundancy by selecting from the PNSN catalog the events with the highest number of P-picks within each region. The times were repicked to provide a uniform picking and error estimate standard for the travel-time picks. Error estimates range from 0.01s to 0.5s with a mean of 0.05s. We include 1433 earthquakes corresponding to 27,600 picks (Figure 2.2). The aforementioned data were ac-
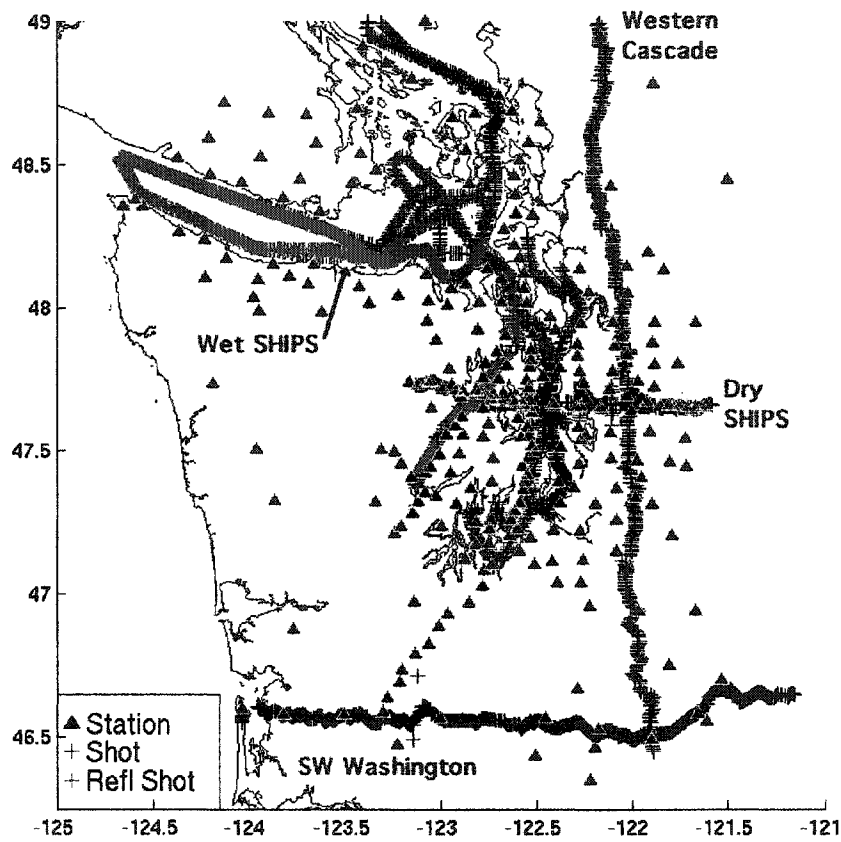
Figure 2.1: Source-Receiver geometry for fixed sources (black +), receivers (triangles), and wide-angle reflection sources (red +). The various experiments are labeled accordingly. Western Cascade: [*Miller et al.*, 1997]; SW Washington: [*Parsons et al.*, 1998]; Wet SHIPS: [*Brocher et al.*, 1999]; Dry SHIPS: [*Brocher et al.*, 2000]
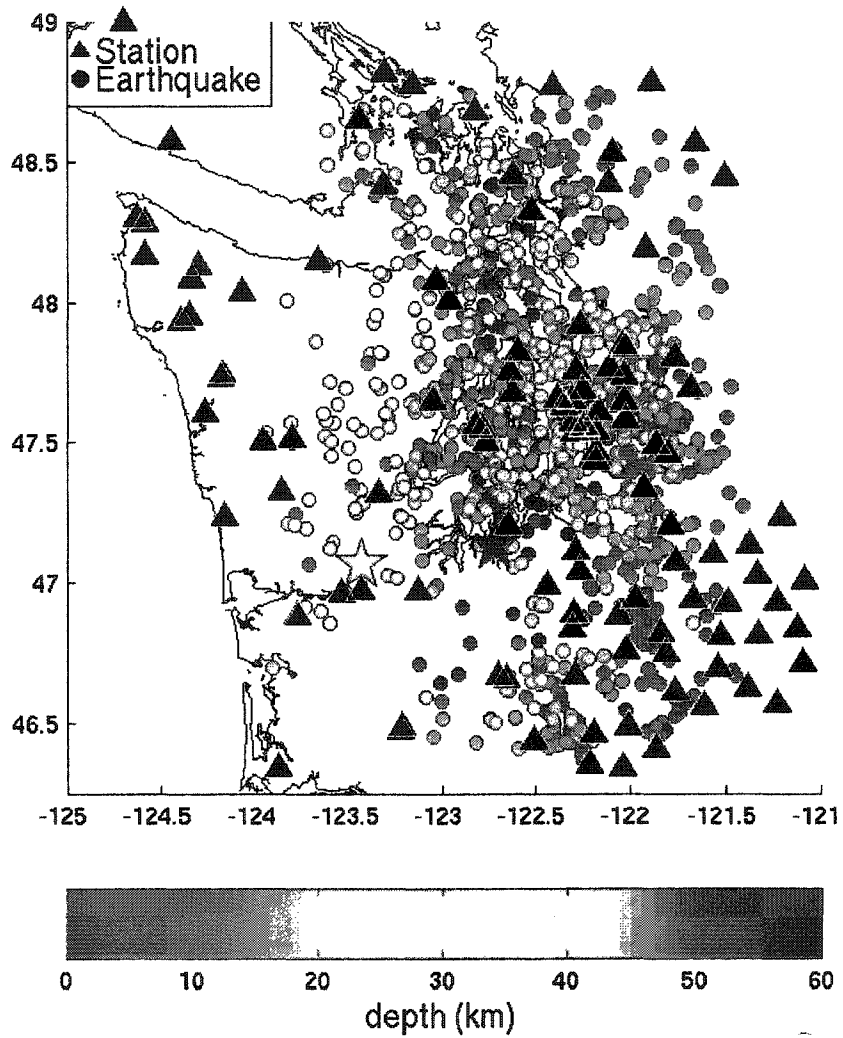
Figure 2.2: Source-Receiver geometry for earthquake sources (circles), receivers (triangles). Depth of earthquakes are color-coded according to the color bar. The M_w 6.8 Nisqually (right) and M_w 5.8 Satsop (left) events are highlighted by the large stars.

cepted unmodified and at face value. See the above references for more information on how respective data sets were collected and analyzed. All sources and receivers are contained within our study region: 121°W to 125°W longitude, 46.25°N to 49°N latitude, and the surface to 78km depth. Latitude and longitude coordinates are converted to Cartesian (x,y) coordinates via the UTM (Universal Transverse Mercator) transformation [*U.S. Geological Survey*, 2001] relative to our local origin at 125°W, 46.25°N. Approximately 20% of the 1433 events are interpreted to occur within the subducting Juan de Fuca plate (Figure 3.4 and warm colors in Figure 2.2). The slab related seismicity consists entirely of intraslab earthquakes, i.e. no events interpreted to be interplate thrusts have been recorded in Cascadia [*Ma et al.*, 1996]. Our data include the 1999 M5.8 Satsop and 2001 M6.8 Nisqually intraslab events. Most other intraslab events within our study have magnitudes between M3.0 and M4.5. The bulk of the remaining events occur within the upper 30km of the overriding North American plate underneath the Puget Lowlands. Some earthquakes are associated with Mt. St. Helens and Mt. Rainier seismic zones. Virtually no earthquakes occur within the core of the Olympic Mountain accretionary complex. Due to quality control procedures, no earthquakes are located west of the Washington coastline.

2.1.2   Wide-Angle Reflections

The travel times for the reflections were entirely handpicked from the 1998 Wet SHIPS experiment (Figure 2.3). Clear secondary arrivals are apparent on record sections from stations located throughout the Wet SHIPS study region (Figure 2.5), producing reflection points scattered over a broad region underlying the Olympic Peninsula (Figure 2.4). These arrivals are most clearly seen from shots on line 4 (Straits of Juan de Fuca) to hard rock sites on the Olympic Peninsula and Cascade foothills (Figure 2.1). Some bedrock sites, such as station 10060 near Mt. Rainier, show clear reflections beyond 240km offset. Soft soil sites, namely those lying within the Puget Lowlands, show limited to no reflector arrivals. Also notable, shots from line 3 within Hood Canal to stations along the northern shores of the Olympic Peninsula show clear reflector arrivals. The bulk of the slab reflection data lie between 100km and 150km offset (Figure 2.3). No reflection arrivals related clearly to
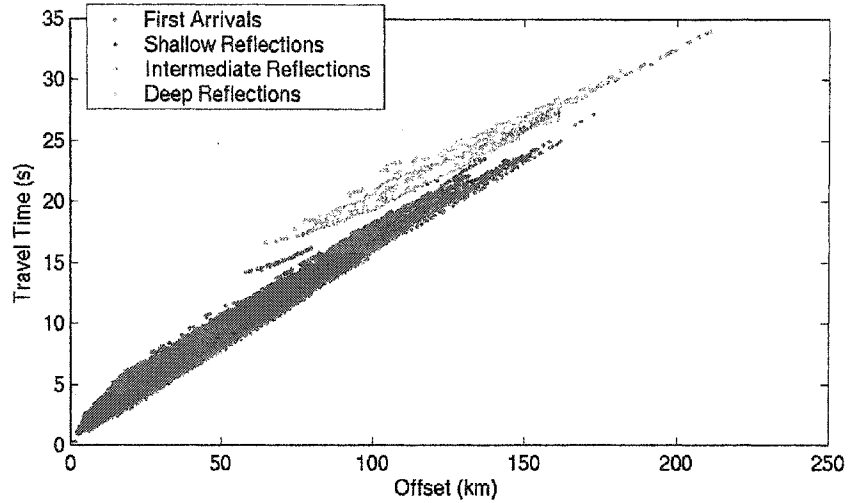
Figure 2.3: Offset (km) vs. observed time for first arrivals (blue), reflections bouncing <35km depth (maroon), those bouncing between 35km and 45km depth (green) and those bouncing >45km depth (cyan)
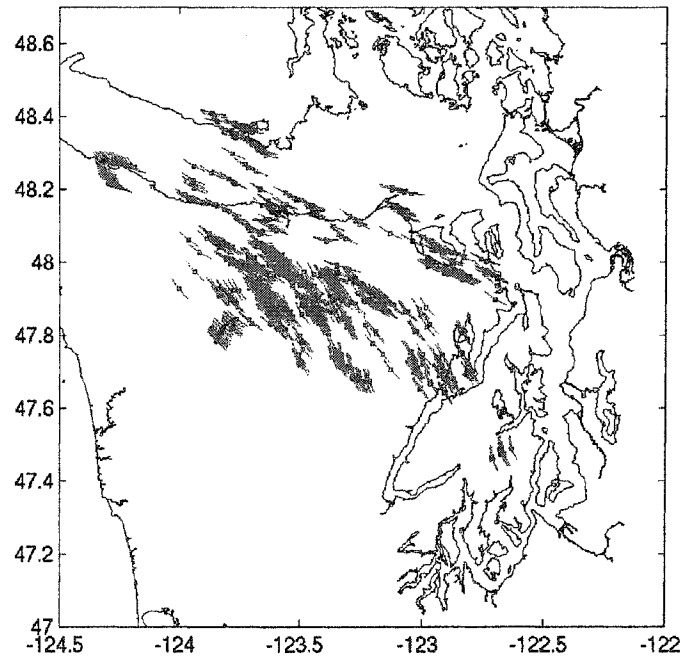
Figure 2.4: Distribution of reflector bounce points (squares) with incoming and outgoing ray azimuth directions.
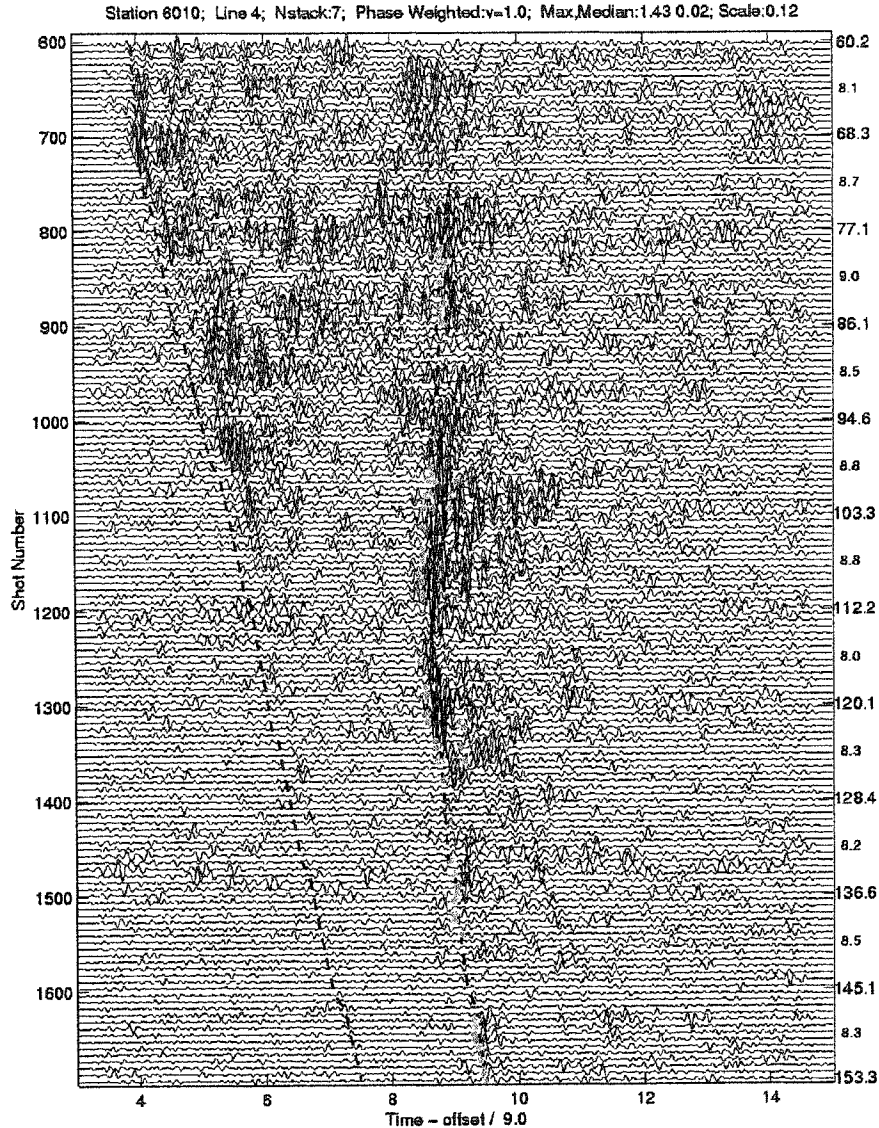
Figure 2.5: Reduced travel-time record section for a station in the NE Olympic Peninsula from shots in the Strait of Juan de Fuca. Traces are seven-fold phase-weighted stacks with an effective trace separation of 350m at the midpoint. Shot numbers are shown along the left and offset (km) (large numbers) and change in offset (km) (small numbers) on the right. Reduced travel time is in seconds. The dashed lines are predicted times for the first arrival (left) and slab reflection (right) based on our model. Green dots are picks made on the reflection and possible other secondary arrivals.
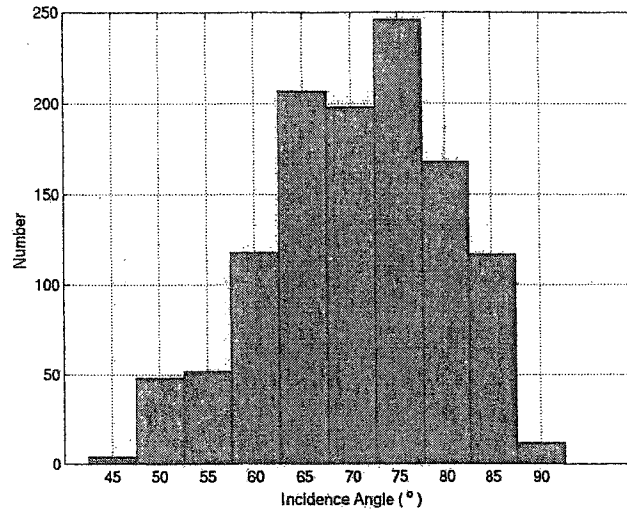
Figure 2.6: Distribution of reflection ray incidence angles relative to reflector surface normals.

the slab are found closer than 50km offset, indicating that the observed arrivals are wide-angle reflections. Indeed, 3-D ray tracing indicates incidence angles of 60° to 85° relative to the slab for the majority of reflections (Figure 2.6). An increase in velocity from 7km/s to 8km/s, as would be expected across the oceanic Moho, yields a critical angle of ~60°, which accords well with the interpretation that the vast majority of our observations are post-critical. It would be especially desirable to have reflector data in the vicinity of the Nisqually earthquake. Unfortunately, the 8000 series stations (NE-SW trending line of stations south of the Nisqually epicenter in Figure 2.1), which would have yielded this information, had very poor signal to noise and we were unable to discern any clear slab reflections from these stations.

Initial assessments of the reflection data were made from processed record sections. Once a shot group was identified as indicating reflected arrivals, the data were scrutinized in greater detail on a waveform-by-waveform basis. Waveforms were bandpass filtered between 1Hz and 14Hz. We applied a seven-fold phase-weighted slant (8 or 9km/s reducing velocity) stack [*Schimmel and Paulssen*, 1997] to shot-ordered seismograms for an effective separation between stacked traces of 700m at the source. The phase-weighted stacks greatly improved

the signal to noise, making for cleaner picks.

According to our picking criteria, an arrival had to be coherent at least across several stacked traces in order to be considered a high-quality pick. Despite coherency, the fact that reflections are secondary arrivals complicated the picking process. Other secondary arrivals interfere with the reflected arrivals, making picking difficult, if not impossible, on some sections. In fact, we picked many arrivals that later were identified as non-reflection picks. Many of these other secondary arrivals were identified as PP, but others are most likely local reverberations of the reflected arrival, while others preceeding the reflection may be associated with the plate interface or the E-reflector identified in LITHOPROBE data [e.g. *Nedimovic et al.*, 2002], although attempts to associate these arrivals with another single reflector failed. The character of the reflected arrivals themselves could at times hinder proper identification. The reflected waveforms often change rapidly over short (<5km) spatial scales (Figure 2.5). Reflected amplitudes can vary from ten times signal-to-noise to imperceptible within the noise over as short as 3km change in offset. Large variations in amplitudes would be expected for rays incident near the critical angle, since slight changes in slab dip or velocity contrast can cause rays to become pre-critical where the theoretical reflection coefficient rapidly becomes much smaller than 1 [e.g. *Aki and Richards*, 1980]. Polarities (first motions), although poorly resolved for most reflected arrivals, vary nearly as rapidly as amplitudes with complete reversals over spatial scales less than 2km (Figure 2.7). This appears to be a near-source effect since we also observe similar polarity and waveform variations on first arrivals, possibly due to small-scale sea bottom scattering or triplication interference effects. One especially difficult characteristic of the reflections was their fairly rapid (few km length scale) variations in horizontal slowness on single record sections. Locally, the reflected arrivals often show nearly constant horizontal slowness values. However, the horizontal slowness can abruptly change, often with the appearance of imbricated arrivals. The difficulty in these circumstances is deciding which arrival is truly the first onset of the reflection. The reflected waveforms are often fairly impulsive with a small pulse directly preceding the maximum amplitude arrival, which is then followed by a decaying series of pulses that persists for about 0.5s.
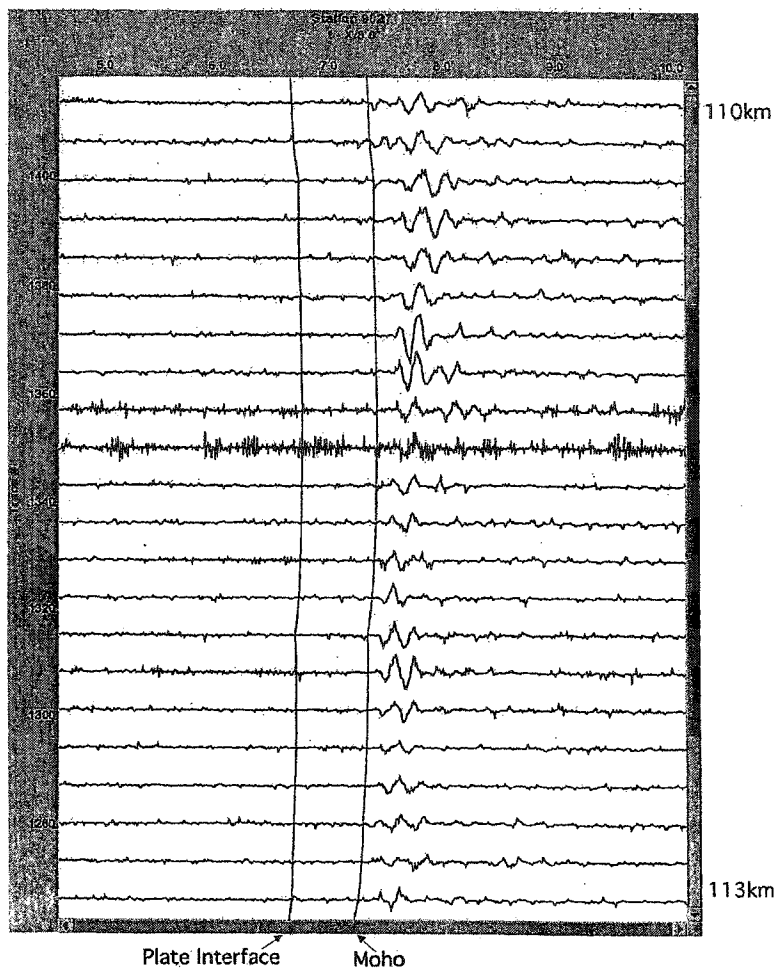
Figure 2.7: Record section from shots on line 4 in the Strait of Juan de Fuca to a station (9027) on the northern Olympic Peninsula. Reduced travel time (8km/s), shot number and offset distance shown along the top, left and right axes respectively. Traces represent seven-fold phase-weighted stacks, giving an effective trace separation of 350m at the mid point. Shown are the wide-angle reflector waveforms. Predicted times for reflections off the "Plate interface" and slab "Moho" (lines) show the large-amplitude wide-angle reflections, and no evidence for reflections off the plate interface. First arrivals are very weak and off the left edge of the figure. Interestingly, the particular data shown in this section were not included in the model calculation. Note the indication of first motion down polarity in the lower portion of the figure and up polarity in the top.

We place each pick into one of three quality categories. Picks with clear, impulsive arrivals are given a quality of 1 and have associated picking errors of <0.05s. Quality 2 picks have low-level noise or some other small arrival preceding the reflection and have picking error estimates of <0.1s. Reflection picks of quality 3 (<0.2s error) are clearly discernible arrivals, but the exact onset is clouded by a mid level of noise or interfering arrivals. Quality 3 picks can also include picks where severe imbrication of the reflector waveform has made accurate determination of the onset time difficult. Nearly 80% of the reflection picks fit into category 1 or 2 qualities.

2.2   Calculated Travel Times and Ray Paths

Travel times are calculated for all source-receiver pairs using a slightly modified version of the Vidale-Hole 3-D finite-difference eikonal travel-time calculator [*Vidale*, 1988, 1990; *Hole*, 1992; *Hole and Zelt*, 1995]. This finite-difference method requires an equally spaced 3-D grid, which for our implementation is set at 2km spacing. Provided an arbitrary point, i.e. "source", which does not have to lie on a grid point, first-arrival travel times are determined to every node in the grid. This is a true first-arrival time calculator, correctly accounting for possible head waves and diffracted waves. The amplitude of the wave corresponding to the times is not determined, so it is impossible to know if a given time at a node would be truly observable. We invoke seismic reciprocity and calculate this travel-time grid once for every station. We do not, however, use these calculated times directly.

To examine errors we calculated travel times using three methods for a constant velocity gradient model. We compared times calculated from the finite-difference (FD) code, calculated by integrating along the ray path, and predicted analytically for a constant velocity gradient. We calculated the ray-path time by first determining the ray paths by following the FD travel-time gradient from source to receiver and then calculating the time with $\sum p(x_i, y_i, z_i) \Delta s$ along the ray path, s, where $p(x_i, y_i, z_i)$ is the trilinearly interpolated slowness at (x_i, y_i, z_i) and Δs is the length of the ray segment [e.g. *Lay and Wallace*, 1995]. For fairly small velocity gradients ($0.1km/s/km$) the RMS error for FD (FD minus analytical

times) was nearly 0.05s with a bias that depended on source location relative to grid nodes. With $\Delta s = 0.2$km, the RMS error for the ray tracing time was < 0.01s with a positive bias, as expected. Larger velocity gradients increased RMS errors for both methods but the ray path method errors were always substantially smaller than those of the FD method. Thus, we adopt the ray tracing scheme to determine our calculated times.

Most regions of the model have velocity gradients $< 0.1km/s/km$ but gradients near the surface exceed $0.5km/s/km$ in several regions and approach $0.2km/s/km$ in the vicinity of the reflector (Figure 3.6). Due to the short paths through these regions of steep velocity gradients, travel-time errors due to these gradients are expected to be small.

2.2.1   Reflection Travel Times and Bounce Points

The reflected ray path consists of two segments: a source to reflector leg and a reflector to receiver leg. Assuming each leg is a first arrival path, we calculate separate travel times for each segment. This entails using both the source and receiver points as "sources" within the Vidale-Hole code. The two complete travel-time grids, one for the source and one for the receiver, are summed to give a single-scattering travel-time grid. Each node of this grid contains the travel time of a "ray" scattering off that point.

This travel-time grid is interpolated to the reflector surface which is defined by depth values at (x,y) nodes. According to Fermat's Principle [e.g. *Aki and Richards*, 1980] ray paths of reflected or turning rays intersect this surface at stationary points on this 2-D travel-time grid, e.g. local minima, maxima, or saddle points. For the models and ray geometries of our experiment, the reflected arrivals all represent local minima. However, since the FD calculator only finds first arrival times, it is possible that the time calculated at the reflector surface corresponds to a ray that penetrated beneath the reflector or to a head wave that travels along the surface, both of which are incorrect for a reflected arrival. We minimize the possibility of both errors by downwardly propagating the velocities immediately above the reflector to beneath the reflector, thus eliminating the vertical velocity gradient below the reflector. Velocities above the reflector are unaffected and are identical to that used by the

remaining data, i.e. fixed sources and earthquakes. Prior to instigating this correction, the vast majority of reflection data behaved properly. Only 5% of the data indicated underside incidence while another 5% arrived at nearly grazing incidence. Following adoption, none of the data demonstrated underside incidence but approximately 5% still were at grazing incidence (Figure 2.6). This, however, would be expected at long offsets and indeed this is the case. Upon examination of a few of the grazing incidence cases, the ray path appeared to be truly grazing incidence reflected arrivals and did not loiter near the reflector surface over extended distances as would be expected for head waves. To determine an accurate estimate of the reflection travel time, we integrate slowness along the reflection ray path. We trace the ray paths from the reflection point to the source and from the reflection point to the receiver.

The reflector surface is allowed to extend vertically outside of the box defined in Section 2.1 in order to remain smooth, but reflection points are not permitted outside of our box. Reflection travel times to grid nodes outside of the box are given a value such that these points could never be minimum times.

2.3   Inverse Procedure

Our data consist of travel times of first arrivals from known and unknown source locations and of reflected arrivals from known source locations. We utilize an iterative inverse procedure where we find incremental changes in model parameters based on travel-time residuals (observed minus calculated), $\delta t = \begin{bmatrix} \delta t_f & \delta t_x & \delta t_r \end{bmatrix}^T$. Our model space is parameterized by slowness ($1/v_P$), u, at each of $n_x \times n_y \times n_z$ nodes in a left-handed Cartesian grid (x: east; y: north; z: down) with a spacing of dx, dy, dz. Particularly, u consists of 76 x-nodes, 80 y-nodes, and 44 z-nodes covering a range of 304km E-W, 320km N-S and from -8km to 78km in depth with 4km spacing horizontally and 2km vertically. Hypocentral parameters, e, consist of the position in x, y, z and origin time for each of our 1433 (n_e) events. The reflector, r, is parameterized by depths (z) at each of the $n_x \times n_y$ Cartesian nodes with spacing dx and dy. Thus, our model on the ith iteration is $\mathbf{m}^i = \begin{bmatrix} \mathbf{u}^i & \mathbf{e}^i & \mathbf{r}^i \end{bmatrix}^T$. However, since we

are performing an iterative procedure, we are solving for $\delta m = \begin{bmatrix} \delta u & \delta e & \delta r \end{bmatrix}^T$ and obtain $m^{i+1} = m^i + \delta m$. In total, we are solving for $n_x * n_y * n_z + 4 * n_e + n_x * n_y (= 279,332)$ parameters. We follow the standard inversion procedure by numerically solving the linear set of constraint equations:

$$A \, \delta m = \delta t \tag{2.1}$$

where A is the $m \times n$ data matrix representing the linearized forward problem, δm is the $n \times 1$ vector of model unknowns and δt is the $m \times 1$ vector of observations. A describes how model perturbations, δm, affect travel-time residuals, δt (observed times minus calculated times for model m^i). The full problem can be rewritten in matrix form, breaking A down into its components:

$$V^{-1/2} \begin{bmatrix} \Lambda_0 & 0 & 0 \\ \Lambda_x & B & 0 \\ \Lambda_r & 0 & R \end{bmatrix} \begin{bmatrix} \delta u \\ \delta e \\ \delta r \end{bmatrix} = V^{-1/2} \begin{bmatrix} \delta t_f \\ \delta t_x \\ \delta t_r \end{bmatrix} \tag{2.2}$$

Λ_0, Λ_x, and Λ_r are determined from ray paths for active sources, earthquakes and reflections respectively. Each element of the respective Λ receives its proportion (in a trilinear sense) of the length of the ray path (km) for that observation that comes within one node of its position. All other node points are set to a value of zero. The matrix of earthquake positional derivatives, B, consists of n_e submatrices each corresponding to the time derivatives with respect to position (x, y, z, and t) at the earthquake hypocenter [*Lay and Wallace*, 1995]. Units for B are s/km for position and dimensionless for origin time. For the reflector surface, time derivatives are calculated with respect to z position at the reflection points (s/km). The values of the derivatives are then proportionately distributed (in a bilinear sense) to the four nodes surrounding the reflection point.

The data are normalized according to their estimated error. V is a diagonal matrix with each diagonal element containing the estimated variance for the appropriate observation. Thus, $V^{-1/2}$ scales each observation by its estimated standard error (σ), i.e. $V_{ii}^{-1/2} = 1/\sigma_i$ (no sum). Additionally, once we had obtained a model, we reweighted each datum depending on its residual variance relative to the variance of the group of data to which it belonged (active source, earthquake, or reflection), e.g. residuals derived from earthquakes were only compared to the variance of the earthquake data as a whole. For observations whose

standard deviations ($\epsilon_i = |\delta t_i| / \sigma_i$, no sum) were less than three times the group standard deviation ($\epsilon_g = \sqrt{\left(\sum \delta t_i^2 / \sigma_i^2\right) / N_g}$, where the sum is over the N_g observations in the group), no reweighting was done. For observations whose standard deviations were between three and five times the group standard deviation, we used a cosine taper for the reweighting, and for those whose standard deviations were greater than 5 times the group standard deviation, the observation was given a weight of zero, i.e.

$$\mathbf{V}_{ii}^{-1/2} = \omega_i / \sigma_i \quad \text{(no sum)} \qquad \text{where} \qquad \omega_i = \begin{cases} 1 & \epsilon_i / \epsilon_g \leq 3 \\ \cos^2(\frac{\pi}{2} \frac{\epsilon_i - 3\epsilon_g}{2\epsilon_g}) & 3 < \epsilon_i / \epsilon_g < 5 \\ 0 & \epsilon_i / \epsilon_g \geq 5 \end{cases} \qquad (2.3)$$

By following this procedure, we desire to remove observations that have unreasonably large errors that may be due to picking errors or incorrect phase identification, while still retaining valid data, which hold structural information. This procedure down-weighted about 3800 data, including nearly 1200 data that were effectively removed from the problem (zero weight).

2.3.1 Regularization

To stabilize the solution to Equation 2.2, we augment it with the following a priori regularization constraints:

$$\begin{bmatrix} \nu \mathbf{L_u} & 0 & 0 \\ 0 & \beta \mathbf{H} & 0 \\ 0 & 0 & \gamma \mathbf{L_r} \\ & \mathbf{C} & \end{bmatrix} \begin{bmatrix} \delta \mathbf{u} \\ \delta \mathbf{e} \\ \delta \mathbf{r} \end{bmatrix} = \begin{bmatrix} -\nu \mathbf{L_u} \mathbf{u}^{i-1} \\ \beta \, \delta \mathbf{h} \\ -\gamma \mathbf{L_r} \mathbf{r}^{i-1} \\ \mathbf{C}(\mathbf{m_c} - \mathbf{m}^{i-1}) \end{bmatrix} \qquad (2.4)$$

$\mathbf{L_u}$ represents the smoothing operator for the slowness structure. We define,

$$\mathbf{R_u}^2 = \left\| \mathbf{L_u}(\delta \mathbf{u} + \mathbf{u}^{i-1}) \right\|^2 \approx \frac{1}{V} \int \int \int \left[\nabla^2 \mathbf{u} \right]^2 dV \qquad (2.5)$$

where

$$\nabla^2 \mathbf{u} = \frac{\delta^2 \mathbf{u}}{\delta \mathbf{x}^2} + \frac{\delta^2 \mathbf{u}}{\delta \mathbf{y}^2} + \eta^2 \frac{\delta^2 \mathbf{u}}{\delta \mathbf{z}^2} \qquad (2.6)$$

is the discretized anisotropic 3-D laplacian and V is the model volume. η represents an anisotropic smoothness parameter which allows us to produce models rougher (or smoother) in the vertical dimension relative to the horizontal dimensions. We expect there to be more

structural variation in the vertical dimension than horizontal so we use a value of 0.25 in our inversions. Because we want the model to be smooth and not just the perturbations, we seek:

$$\mathbf{L_u u^i = L_u(u^{i-1} + \delta u) = 0}$$

so,

$$\mathbf{L_u \delta u = -L_u u^{i-1}} \tag{2.7}$$

To stabilize the hypocenter relocation portion of the problem, we require that the perturbations to the earthquake positions be small, where $\mathbf{H}$ is defined as,

$$\mathbf{H^2 = \sum_{j=1}^{n_e} \delta x_j^2 + \delta y_j^2 + \zeta^2 \delta z_j^2 + \xi^2 \delta t_j^{orig\,2}} \tag{2.8}$$

where ζ (dimensionless) reweights the depth component, allowing application of our a priori assumption that the epicentral positions are better known than the depths, and ξ (km/s) rescales the origin time component into consistent units, giving $\mathbf{H}$ units of km. Our implementation uses $\zeta = 0.5$ (more depth variation than epicentral) and $\xi = 3km/s$ (less origin time variation than spatial). By setting δh in Equation 2.4 to be zero, we seek solutions which minimize hypocenter perturbations relative to the previous iteration. Alternatively, we can require perturbations from some preferred positions be small, in which case δh would consist of the differences between the present position and the preferred position. In our inversions, we use δh $= 0$, but found that relocated hypocentral positions were largely independent of which method we choose, given the relatively small weight these equations were given in our scheme (see below).

The reflector surface is regularized similarly to the velocity structure. We implement two operators to regularize the reflector surface: $\mathbf{L_{Rlap}}$ and $\mathbf{L_{Rx}}$, where from Equation 2.4

$$\mathbf{L_r = \begin{bmatrix} L_{Rlap} \\ \kappa L_{Rx} \end{bmatrix}} \tag{2.9}$$

The first represents the standard discrete 2-D laplacian in order to force the surface to be smooth. Our bias, based on earthquake locations, was that the reflector surface is nearly planar. Requesting the reflector surface be smooth in a laplacian sense, i.e. $\frac{\delta^2 r}{\delta x^2} + \frac{\delta^2 r}{\delta y^2}$, is

insufficient to achieve a nearly planar surface. To embed our assumption into the problem, we added the second operator which measures the torquing of the surface via the second order surface derivative $\frac{\delta^2 r}{\delta x \delta y}$. The discrete form is derived from the fact that $\frac{\delta^2 r}{\delta x \delta y} = \frac{d}{\delta x}(\frac{\delta r}{\delta y})$. The discretized form of this equation is

$$D_{xy}(x,y) = \frac{r_{x+1,y+1} - r_{x+1,y-1} - r_{x-1,y+1} + r_{x-1,y-1}}{4\,\Delta x\,\Delta y}.$$

Applying the above operator to the reflector gives us the desired nearly planar surface. We define

$$\mathbf{R_r}^2 = \left\|\mathbf{L_{Rlap}}(\delta\mathbf{r} + \mathbf{r}^{i-1})\right\|^2 + \kappa^2 \left\|\mathbf{L_{Rx}}(\delta\mathbf{r} + \mathbf{r}^{i-1})\right\|^2$$

$$\approx \frac{1}{A}\int\int\left(\frac{\delta^2\mathbf{r}}{\delta x^2} + \frac{\delta^2\mathbf{r}}{\delta y^2}\right)^2 + \kappa^2\left(\frac{\delta^2\mathbf{r}}{\delta x\,\delta y}\right)^2 dA \tag{2.10}$$

where A is the reflector surface area and κ weights the cross-derivative term relative to the 2-D laplacian term and in our inversion has the value of 25 (dimensionless). Like the slownesses, we want the reflector model itself to be smooth, not the perturbations.

The fourth row of Equation 2.4 allows us to impose a priori constraints on the model parameters. In our implementation, we force the deepest layer of the velocities to be 8.1 km/s by setting the appropriate terms of $\mathbf{m_C}$ to 1/8.1, and setting the appropriate diagonal elements of $\mathbf{C}$ to 10,000 km/s (strong weighting) and all other elements to zero. In addition, we impose weaker constraints on the depth of the reflector on the northern and southern edges (based on *Crosson and Owens* [1987]) and at one point on the eastern edge coincident with the deepest earthquakes in Cascadia. To implement these constraints, the appropriate terms of $\mathbf{m_C}$ are set to the desired depth and the appropriate diagonal elements of $\mathbf{C}$ to 3 km^{-1} (weak weighting) and all other elements to zero. The reflector depth constraints are very weak and do not affect the reflector surface where constrained by travel-time data; these a priori constraints only affect the extrapolation of the reflector surface.

Five trade-off parameters, $\alpha, \nu, \beta, \gamma$ and κ, are used to determine how important each of the regularization terms are to the overall inversion. α (dimensionless, Equation 2.11) is the overall weighting parameter for the regularization. Scaling α larger causes a smoother velocity structure, smoother reflector surface, and less hypocentral relocations. For all our

inversions ν has a value of 1 $km^2/(s/km)$. β (km^{-1}) weights the hypocenter regularization relative to model smoothness and is given a value of $10^{-5}km^{-1}$. γ $(0.002\ km^2/km)$ determines the relative weighting given to the reflector laplacian smoothing and, additionally weighted by κ (25, dimensionless), the cross-derivative operators. By adjusting these parameters, one can accomplish a wide range of model appearances and behavior. Unfortunately, this forces some subjective judgment on the final outcome of the model. This can be minimized by recognizing realistic limits on resolution and in errors, which can be determined more objectively by performing resolution and error analyses (Chapter 4).

2.3.2 Inversion

The data and regularization portions from Equations 2.2 and 2.4 of the problem are combined and give the general form:

$$\left[\begin{array}{c} \hat{\mathbf{A}} \\ \alpha\hat{\mathbf{L}} \end{array}\right]\delta\mathbf{m} = \left[\begin{array}{c} \hat{\delta\mathbf{t}} \\ \alpha\hat{\delta\mathbf{l}} \end{array}\right] \tag{2.11}$$

From this equation we are minimizing:

$$\left[\hat{\mathbf{A}}\,\delta\mathbf{m} - \hat{\delta\mathbf{t}}\right]^{\mathbf{T}}\left[\hat{\mathbf{A}}\,\delta\mathbf{m} - \hat{\delta\mathbf{t}}\right] + \alpha^2\left[\hat{\mathbf{L}}\,\delta\mathbf{m} - \hat{\delta\mathbf{l}}\right]^{\mathbf{T}}\left[\hat{\mathbf{L}}\,\delta\mathbf{m} - \hat{\delta\mathbf{l}}\right] \tag{2.12}$$

By the definition of χ^2,

$$\chi^2 = \sum_{i=1}^{N}\left[\frac{t_i^{obs} - t_i^{calc}}{\sigma_i}\right]^2 \tag{2.13}$$

which is dimensionless and $<\chi^2>= N$. Identifying χ^2 with the first term of Equation 2.12 and expanding the second gives

$$\chi^2 + \alpha^2\left\{\nu^2\left\|\mathbf{L_u}(\delta\mathbf{u} + \mathbf{u}^{i-1})\right\|^2 + \beta^2\left\|\delta\mathbf{e} - \delta\mathbf{h}\right\|^2 + \gamma^2\left\|\mathbf{L_{Rlap}}(\delta\mathbf{r} + \mathbf{r}^{i-1})\right\|^2 + \right.$$

$$\left. \gamma^2\kappa^2\left\|\mathbf{L_{Rx}}(\delta\mathbf{r} + \mathbf{r}^{i-1})\right\|^2 + \left\|\mathbf{C}(\delta\mathbf{m} - (\mathbf{m_C} - \mathbf{m}^{i-1}))\right\|^2\right\} \tag{2.14}$$

Renaming and collecting terms we get:

$$\chi^2 + \alpha^2\left\{\nu^2\mathbf{R_u}^2 + \beta^2\mathbf{H}^2 + \gamma^2\mathbf{R_r}^2 + \mathbf{K}^2\right\} \tag{2.15}$$

This equation forms the basis for the trade-off analysis. It is instructive to look at the units of each of these terms. χ^2 is unitless, because we have scaled the data by their estimated

errors; $\mathbf{R_u}$ is the laplacian of the slowness structure which has units of $(s/km)/km^2$; $\mathbf{H}$ is in km; $\mathbf{R_r}$ is composed of two second order operators, both of which have units of km/km^2; $\mathbf{K}$ contains the external model constraints and is dimensionless.

If we collapse our two element Equation 2.11, we get the standard inverse equation:

$$\mathbf{A}\,\delta\mathbf{m} = \delta\mathbf{b} \tag{2.16}$$

Traditionally, one rearranges and solves for $\delta\mathbf{m}$ in a least squares sense [e.g. *Parker*, 1994],

$$\delta\mathbf{m} = (\mathbf{A^T A})^{-1}\mathbf{A^T}\delta\mathbf{b} \tag{2.17}$$

This, however, involves finding $(\mathbf{A^T A})^{-1}$ which becomes increasingly difficult as the number of model parameters grows and eventually proves impractical except for the most powerful computers, due mainly to memory constraints. Typically, velocity tomography problems such as ours have a sparse ($< 1\%$ non-zero) $\mathbf{A}$ but $\mathbf{A^T A}$ is in general not sparse. This requires storage of n^2 (n is the number of model parameters) numbers in order to perform the inversion. In our case, n is on the order of 280,000, which is prohibitively high for direct inversion or for Singular Value Decomposition methods. Thus, we employ the Conjugate Gradient Least Square (CGLS) algorithm [*Paige and Saunders*, 1982], which iteratively solves the above equation indirectly. $\mathbf{A}\,\delta\mathbf{m} - \delta\mathbf{b} = \varepsilon_1$ will, in general, never equal zero but will approach some minimum value. $(\mathbf{A^T A})\delta\mathbf{m} - \mathbf{A^T}\delta\mathbf{b} = \varepsilon_2$ will, however, approach zero as ε_1 approaches its minimum value. The CGLS method uses the latter equation and iteratively approximates $\delta\mathbf{m}$ that minimizes ε_2. The solution, $\delta\mathbf{m}$, is considered sufficiently accurate when ε_2 reaches some minimum threshold value determined by the user, which we typically set at 0.025% of the entrant ε_2.

Once we obtain the solution, $\delta\mathbf{m}$ is added to the previous model, $\mathbf{m}^{i-1}$, to obtain the updated model, $\mathbf{m}^i$. Since the earthquakes are free to move within the inversion, some events may wander outside the defined box. This could occur either because of instabilities in a particular earthquake or because the event would be best positioned outside of the box. Instabilities could be a transient effect due to an improper location in an intermediate step of the iterative inversion process, or to inconsistencies in the data that do not allow stable

location. In order to avoid throwing away earthquakes that are only transiently unstable, we move earthquakes that relocated outside the box back into the box. If the same earthquake repeatedly attempts to move outside the box, it is assumed the earthquake is more than just transiently unstable and removed after a prescribed number of attempts. Only 4 earthquakes were discarded by this method. Reflection bounce points that locate outside the box or on the edges of the box are discarded. No reflection data were discarded by this procedure.

Following the determination of a new model, theoretical travel times and their corresponding residuals for the new model are calculated. The size of the model is calculated via $\left|\delta\mathbf{b^i}\right|^2$. We want

$$\left|\delta\mathbf{b^i}\right|^2 < \left|\delta\mathbf{b^{i-1}}\right|^2 \qquad (2.18)$$

and if this were a purely linear problem, this would always be true. However, this is a highly non-linear problem and it is possible for the above statement to be false following any single inversion for $\delta\mathbf{m}$. To circumvent this possibility, we use $\mathbf{m^i} = \mathbf{m^{i-1}} + \gamma\delta\mathbf{m}$ where γ is a number between 0 and 1. $\gamma = 1$ is used unless Equation 2.18 is not satisfied, in which case γ is repeatedly halved until Equation 2.18 is satisfied or γ becomes too small, at which point the inversion fails and terminates the run. Typically, when Equation 2.18 is not satisfied initially, γ must be halved only once to satisfy the condition. This procedure ensures that each subsequent model is better than the preceding ones.

The non-linearity of the system necessitates the iterative repetition of above steps in toto to arrive at the solution we seek. If the problem were strictly linear, one iteration would completely solve the problem. The non-linearity derives from the fact that $\mathbf{A}$ depends upon the model parameters. Any single $\delta\mathbf{m}$ from any one iteration only approaches the solution. As more iterations are performed, in general, $|\delta\mathbf{m}|^2$ should decrease as $\mathbf{m}$ incrementally approaches the solution to the underlying non-linear problem. Convergence is determined when the sizes of the components of $\delta\mathbf{m}$, i.e. $\delta\mathbf{u}$, $\delta\mathbf{e}$, and $\delta\mathbf{r}$, compute to less than their respective threshold convergence criteria. These respective limits have been set somewhat arbitrarily at RMS($\delta\mathbf{u}$) $< 0.0095 s/km$, RMS($\delta\mathbf{e}$) $< 300m$ and $0.3s$ and RMS($\delta\mathbf{r}$) $< 600m$.

Chapter 3

Results

As discussed in Chapter 2, we solve for a smooth velocity structure, smooth reflector geometry and hypocentral locations using a nonlinear inverse procedure. The purpose of this chapter is to elucidate the results of this inversion. We find that the reflector, although it approximately parallels the relocated intraslab seismicity, divides the seismicity into two groups. Those earthquakes up-dip of the 45km reflector depth contour occur below the reflector, while those down-dip of this contour occur primarily above the reflector. Although a detailed discussion of the interpretation is given in Chapter 5, we will briefly outline the interpretation so that the results can be fit into a physical framework. We interpret the wide-angle reflector as the subducted oceanic Moho. The up-dip intraslab earthquakes are occurring within the subducted mantle, associated with serpentine dehydration, while the down-dip events are occurring primarily within the subducted crust, associated with the basalt to eclogite transformation.

3.1 Trade-Off and Variance Reduction

Solutions to this nonlinear tomography-hypocenter-reflector problem are non-unique and, therefore, how the "best" model is chosen is somewhat subjective. Typically, one of the major trade-offs in tomography problems is the smoothness of the velocities relative to the data misfit. Our problem consists of several trade-off parameters that are used to

regularize the various parameters relative to the data misfit as outlined in Sections 2.3.1 and 2.3.2. The controlling parameter, however, is α in Equation 2.15, which scales all the others. We plot the χ^2 misfit versus the model size, $\|m\|^2$ (portion of Equation 2.15 in curly braces) (Figure 3.1). If accurate data error estimates have been used, then χ^2/N should equal 1, but it is not unusual for error estimates to be overly optimistic, producing χ^2/N values greater than 1. An appropriate value for the trade-off parameter should come from a portion of the curve with reasonable curvature, since the flatter or steeper portions of the curve indicate that it is far from an equitable trade-off between the model size and misfit. Our chosen trade-off parameter corresponds to the star in Figure 3.1 and lies in a region with good curvature. The model corresponding to the next smaller value of α, although it fits the data better, is noticeably rougher, producing many features that we considered unrealistic. However, comparison of this rougher model to our preferred one, reveals that our interpretations are unaffected by our choice of models. Our preferred model has $\chi^2/N = 2.3$ for the data overall. However, breaking up χ^2/N into its constituent parts yields 2.3, 2.6, and 1.1 for the fixed-source, earthquake, and reflection data respectively.

Although having overly optimistic error estimates can cause χ^2/N values to exceed 1, another possibility is the presence of small scale structure in the real earth that is unmodeled. To investigate the severity of this possibility we subdivide the data into three groups based on the estimated error and plot the distribution of weighted residuals (Figure 3.2). Although there is a tendency for the residuals from observations with small error estimates to have a broader distribution, as would be expected if we are not modeling small scale structure, the trend is mild, only varying by half a standard deviation between the group with the smallest and largest error estimates. Thus, we conclude that although we certainly are not modeling the small scale structure that we possibly could, much of the larger than expected values from χ^2/N is attributable to overly optimistic error estimates.

Often, variance reduction is used to express the effectiveness of a model to explain structure. However, this number depends strongly on what reference or starting model is used in the comparison. To evaluate the effect of a 3-D model to a 1-D model, we compare the variance of the starting 1-D model to the best 3-D model.
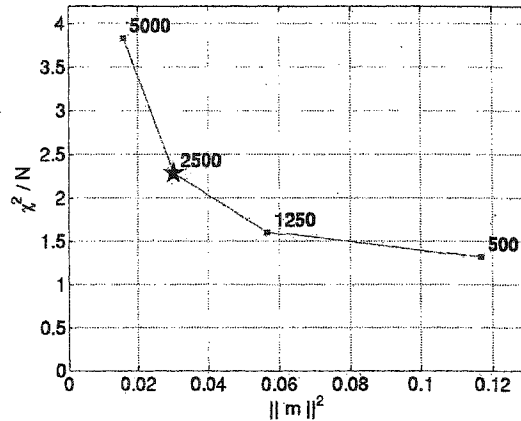
Figure 3.1: Trade-off curve. Values of α are shown next to each point. The star corresponds to our chosen trade-off parameter.

For the starting model, we used the 1-D P-wave velocity model that is used to routinely locate earthquakes within western Washington by the PNSN [Crosson, 1976]. Starting hypocentral locations consist of catalog positions and times derived from the starting velocity model and station corrections. The initial location for the reflector surface is a horizontal surface at 20km depth. The initial velocity and hypocentral positions are reasonable for our study region and, thus, variance reductions can be meaningful. However, as we will see, a horizontal reflector at 20km depth is completely inappropriate for the wide-angle reflection data and, therefore, the variance reduction for the reflections are meaningless. Table 3.1 gives the root mean square (RMS) travel-time residuals and variance reductions, where appropriate, broken down into the three data types. Visually, the large variance reduction can be seen by comparing the residual times for the starting model versus the final model (Figure 3.3).

Table 3.1: RMS residuals and variance reductions for final model

	RMS(s)	Variance Reduction
Active Source	0.09	98.7%
Earthquake	0.12	91.0%
Reflection	0.08	NA
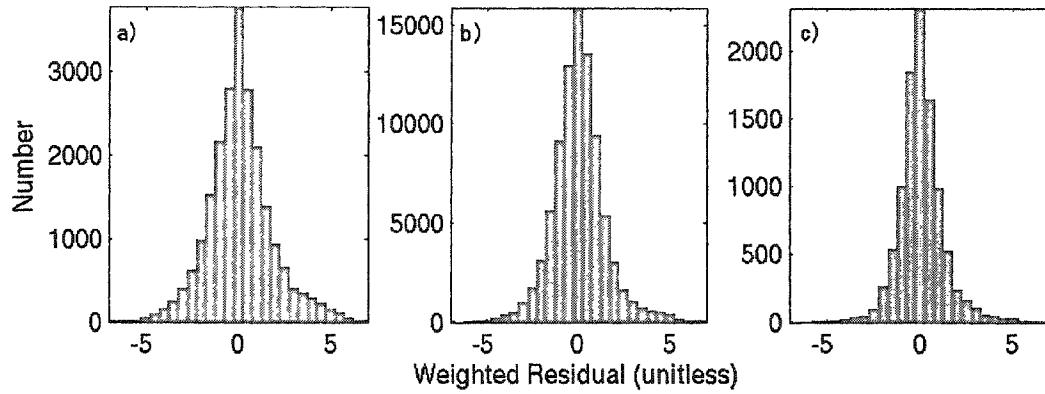
Figure 3.2: Distribution of weighted residuals grouped by estimated error: a) <0.04s, b) ≤0.08s and ≥0.04s and c) >0.08s.
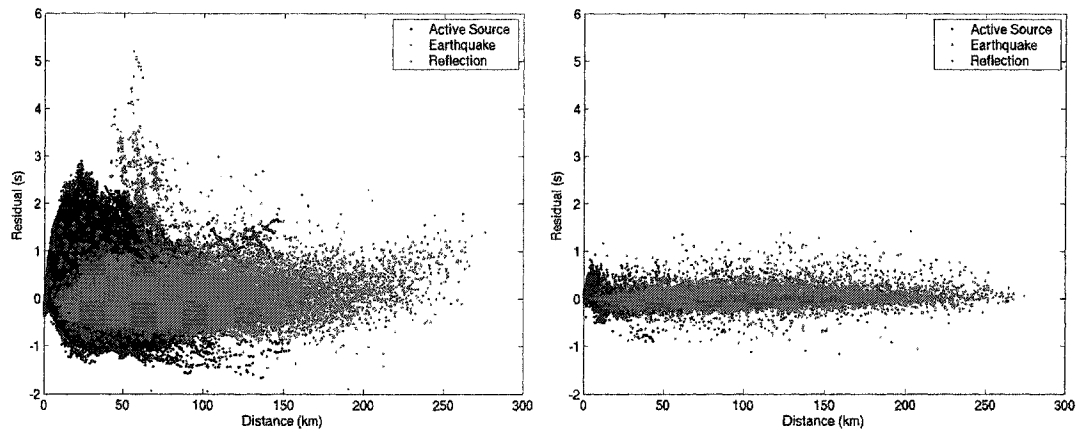
Figure 3.3: Residual vs. offset for starting model (left) and final model (right) coded according to first arrivals (black), earthquakes (blue) and reflections (magenta).

3.2 North-American Plate Structure

The goal of this study is to describe the interrelationships among the velocities, seismicity and wide-angle reflector in reference to the subducting Juan de Fuca plate. Accordingly, we focus little on the shallow structure and only give a brief synopsis of the results. For a more detailed discussion of the shallow structure in NW Washington see *Symons* [1998],*Brocher et al.* [2001], and *van Wagoner et al.* [2002]. We observe the same large-scale structure as they describe. Within the top 10km, the Puget Lowlands are dominated by several sedimentary basin structures, most notably the Seattle Basin (Figures 3.11 and 3.12). These basins have very low seismic velocities in our model — around 3–4km/s — and little seismicity. Beneath the basin structures is a high velocity region (∼7km/s) which has been interpreted as the Crescent (Siletzia) terrane, a volcanic sequence which is widespread in the Cascadia forearc (Figures 3.13 and 3.14) [e.g. *Trehu et al.*, 1994]. The shallow North American plate seismicity is concentrated within these high velocity rocks. The Olympic Mountains sit on top of a very low velocity core with velocities as low as 5.5km/s at 20km depth under the heart of the peninsula. The Olympic core rocks have been interpreted as composed of metasediments scraped from the subducting Juan de Fuca plate and obducted on to the North American plate [e.g. *Brandon and Calderwood*, 1990]. This low velocity region, which has been interpreted as metasediments being dragged down with the subducting lithosphere, extends to the top of the subducting lithosphere and appears to underthrust the higher velocity Crescents under Puget Sound [*Crosson, personal communication*]. Very few earthquakes occur within these low velocity rocks.

3.3 Reflector Geometry

The constrained portion of the reflector surface (Figure 3.4 and 3.5) shows many of the same characteristics as previous studies have suggested (Section 1.3.1 and Figure 1.3). Reflector contours demonstrate a shallow, approximately east-dipping (∼15°) surface under the central portion of the Olympic Peninsula and bend around to closely follow the SW
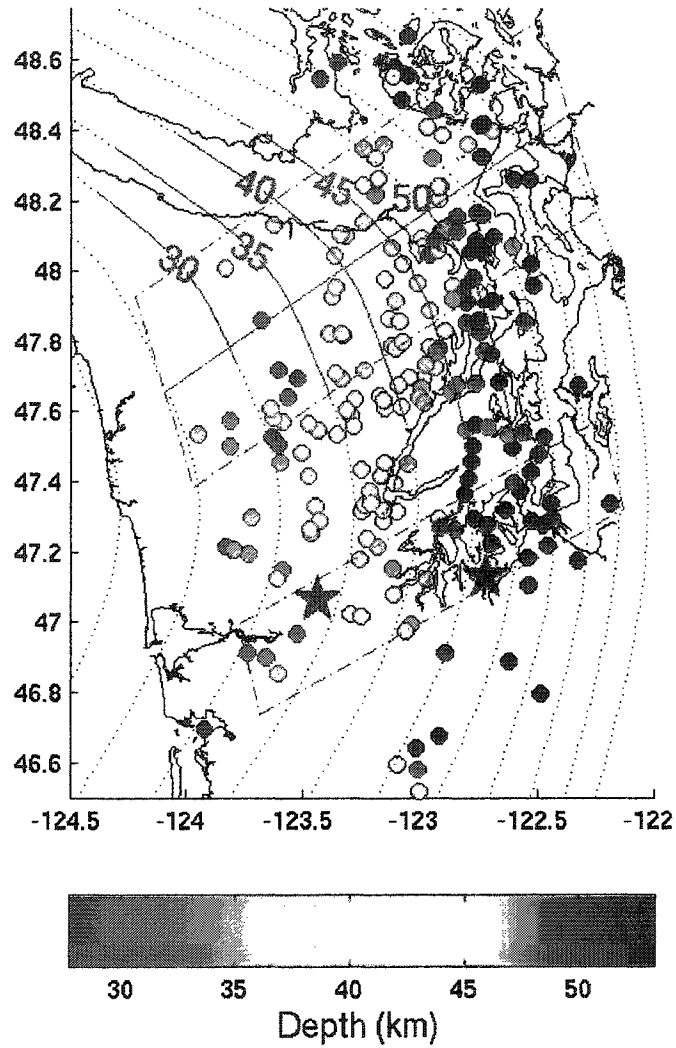
Figure 3.4: Reflector depth contours (km) solid where constrained, dotted where extrapolated and relocated intraslab earthquakes (circles) coded according to depth (color bar). The Nisqually (right) and Satsop (left) events are highlighted by the large stars. Also outlined are cross-sections aligned parallel to the relative plate motion (55°azimuth [Wilson, 2002]) shown in Figures 3.6, 3.9 and 3.10.

British Columbia coastline in the north. Depth to the subducted Moho (reflector) is about 30km in the farthest up-dip constrained region just east of the Washington coastline to over 50km under Puget Sound. To extrapolate the reflector beyond our data coverage, we have constrained the reflector to approximate the depth contours of the slab in Figure 1.3 at the northern and southern edges of our model. We use the locations of the deepest earthquakes in Cascadia (Figure 1.3) to constraint an approximate depth of the reflector on the eastern edge of the model. These constraints do not affect the portion of the reflector constrained by data, but only the extrapolated portions. Unfortunately, the constrained portion of the reflector does not extend far enough south to encompass the Nisqually event (Figure 3.4).

3.4 Intraslab Earthquakes Relative to the Reflector

One of the main goals of this research is to determine the relationship between the locations of the intraslab earthquakes and the structural elements of the subducting slab. An ideal reference for this comparison is the wide-angle reflector which we have interpreted as the subducting Moho. In Figure 3.5, the relocated intraslab earthquakes are shown relative to the reflector surface. We have divided the events into three categories: those occurring more than 2km beneath the reflector, those occurring within 2km either side of the reflector and those occurring more than 2km above the reflector. The group which lies within 2km of the reflector we consider ambiguous based on error analysis (Section 4.4.2). Seismicity rates clearly decrease to the northwest, especially in the shallower portions of the slab. However, a distinct pattern appears in the relative location of the intraslab earthquakes to the reflector up- and down-dip (parallel to cross sections in Figures 3.6, 3.9 and 3.10). Where the reflector is shallower than 40km depth, there are no unambiguous events which occur above the reflector. In a similar manner, there are no unambiguous events occurring beneath the reflector where the reflector is deeper than 50km. Between the depth contours of 40km and 50km there are a mix of event types.
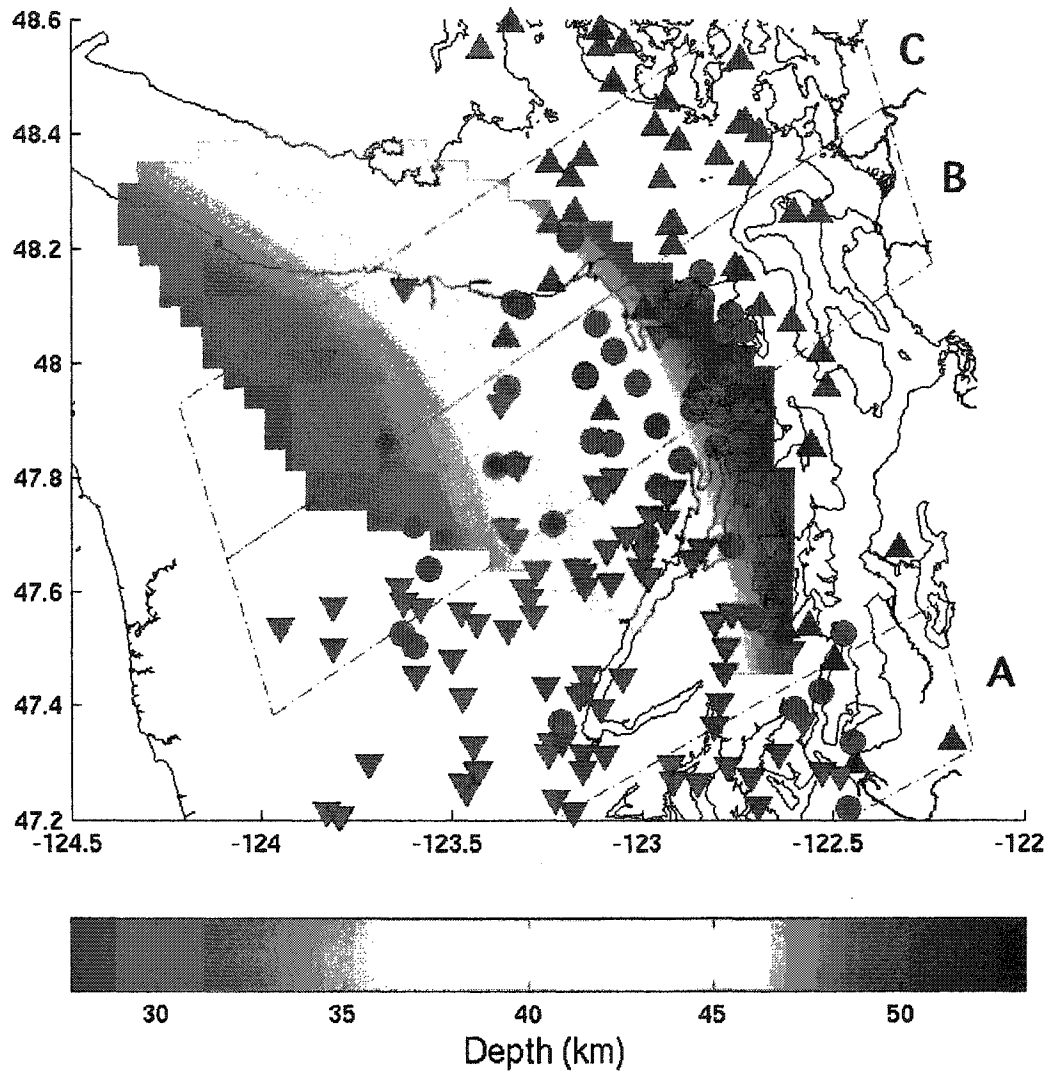
Figure 3.5: Intraslab earthquakes relative to the reflector. The constrained portion of the reflector is shown by the shaded surface coded according to the color bar. Intraslab events are divided into three categories: those more than 2km beneath the reflector (blue downward triangles), those within 2km of the reflector (magenta circles), and those more than 2km above the reflector (red upward triangles). Also outlined are cross-sections aligned parallel to the relative plate motion shown in Figures 3.6, 3.9 and 3.10.
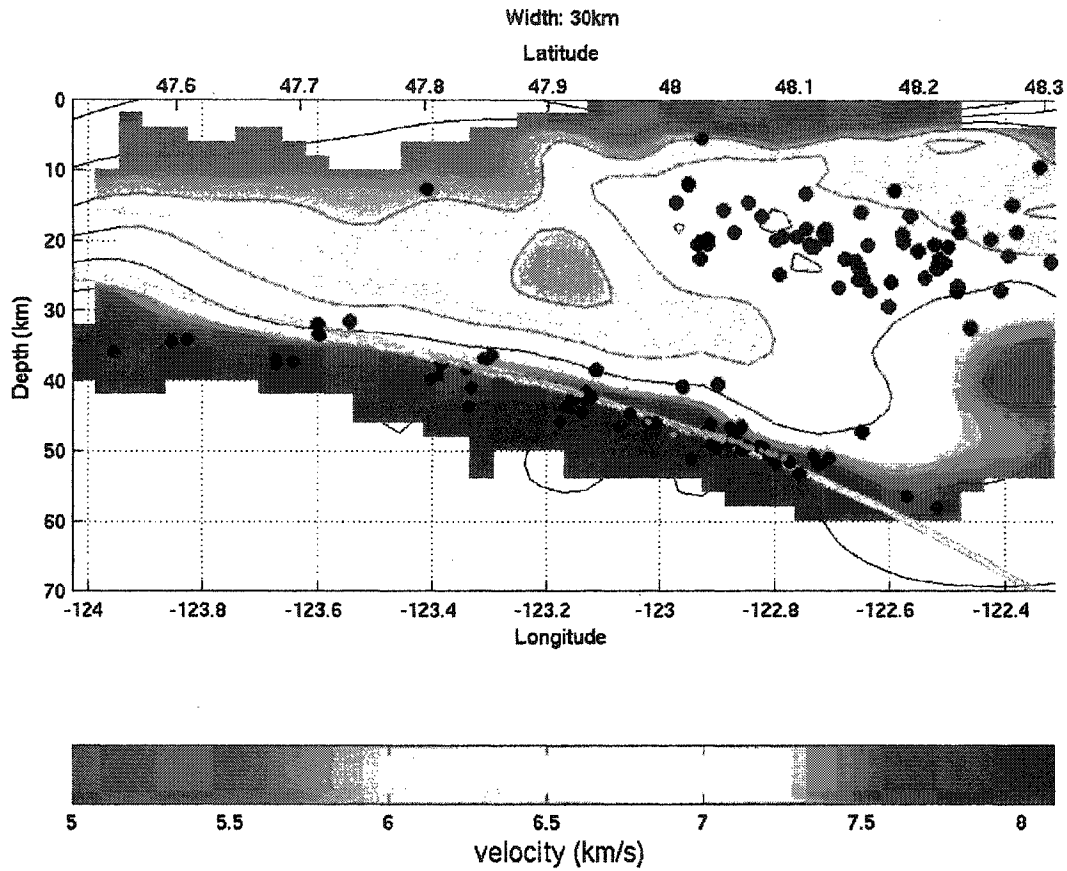
Figure 3.6: Cross-section (30km width) through the Olympic Peninsula aligned parallel to the relative plate motion direction (central boxes in Figures 3.4 and 3.5 (B)). P-wave velocity model is colored according to the color bar at bottom and is only shown where constrained. Contours are at 0.5km/s intervals. Black dots represent relocated seismicity. The reflector surface (thick cyan line) and reflection bounce points (green dots) are also indicated. Since this is a diagonal cross-section, both latitude (top axis) and longitude (bottom axis) are given. There is no vertical exaggeration in any of the cross-sections.

3.5 Deep Structure

A 30km wide cross section aligned parallel to the relative plate motion direction passing through the middle of the Olympic Peninsula, where the bulk of our reflection and intraslab earthquake data occur, demonstrates the main features of the model (Figure 3.6). The shallow structure is dominated by the low velocity Olympic core in the west and high velocity Crescent terrane in the east. In the vicinity of the slab, velocity gradients become very strong and velocity contours roughly parallel the reflector and intraslab earthquakes. Nowhere within our model does there appear a low-velocity zone associated with the subducting crust. In fact, velocities increase strongly with depth throughout the constrained region generally starting several kilometers above the reflector. The reflector traverses ~7km/s velocities up-dip at 30km depth to near 8km/s down-dip at 55km depth (Figure 3.7). The intraslab earthquakes generally lie below the reflector in the up-dip direction. They are confined to a narrow zone approximately 4–6km thick, which nearly parallels the reflector but is slightly inclined toward it at greater depth. It becomes ambiguous down-dip whether these events are occurring at the very top of the mantle or within the base of the oceanic crust. The velocities in which these earthquakes occur are from lower to mid 7km/s range up-dip to greater than 8km/s down-dip, the majority occurring in velocities >7.5km/s (Figure 3.8). This mantle band of earthquakes is the predominate type of intraslab event in our data set. Earthquakes that clearly occur above the reflector begin at about 40km depth and extend to over 50km depth. These events are more diffuse spatially than the mantle events, occupying a nearly 8km thick zone. They occur in velocities between upper 6km/s and low to mid 7km/s range (Figure 3.8).

Velocities at earthquakes that lie beneath the reflector are generally >7.5km/s. Despite the fact that we constrained the velocity to be 8.1km/s at the base of the model, error and resolution analysis indicate we do resolve 8km/s velocities in this region (see Section 4.3). In the down-dip portion of Figure 3.6 (or equivalently under Puget Sound in the depth sections Figures 3.15 and 3.16) beneath the Crescent terrane is a large region of velocities near 7km/s even at depths greater than 40km. No North American Moho has ever been
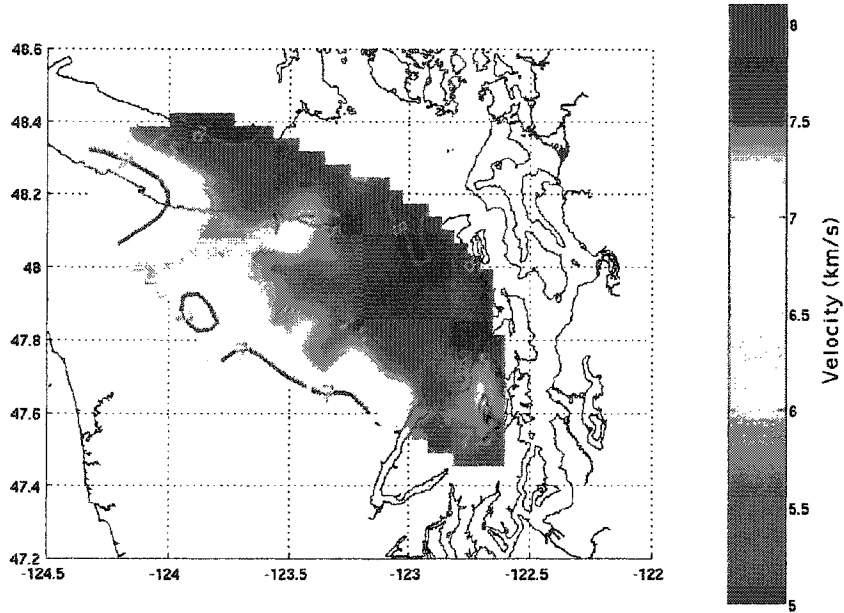
Figure 3.7: Model P-wave velocity at the reflector surface coded according to color bar at right and contoured at 0.5km/s intervals.
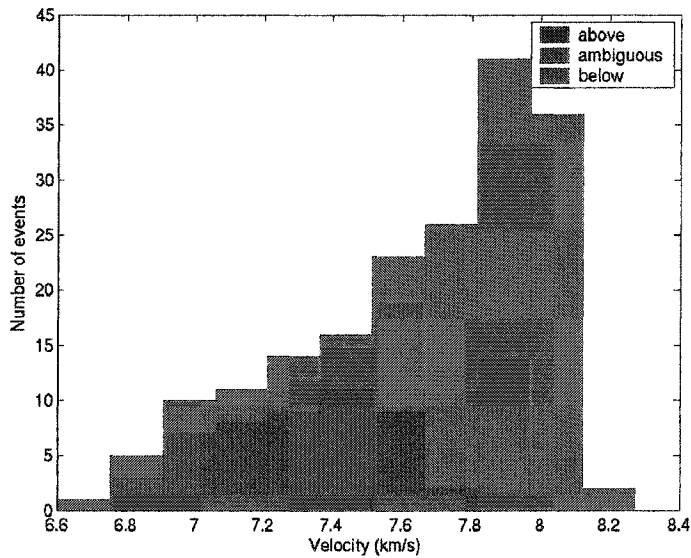
Figure 3.8: Stacked histogram showing the velocity distributions of the three categories of intraslab events described in Figure 3.4.

observed in this section of the Cascadia forearc so the exact location of the forearc mantle wedge is unknown. Velocities throughout this region are too low to be normal mantle rocks, thus, perhaps this indicates a serpentinized mantle wedge for this area as has been hypothesized in other places in Cascadia (see Section 5.6).

Cross sections to the north and south of this main section show many of the same characteristics but with some variations. Farther south, the constrained region of the slab only covers the most down-dip regions and eventually disappears, making inferences on the relative placement of the earthquakes to the reflector tenuous. However, velocities indicate roughly the same division of events as in the north. Most notably, the Nisqually and Satsop events occur in velocities near 8km/s which would place the Satsop quake below the slab Moho, and the Nisqually right at the slab Moho following the same prescription as under the Olympic Peninsula (Figure 3.9). To the north of our main cross section, the primary problem is the scarcity of earthquakes, especially in the up-dip direction (Figure 3.10). Although it seems clear that at least some, if not the majority, of the intraslab events are occurring above the reflector, apparently within the subducted oceanic crust, very few events actually occur in a region where we have reflection data, so the extrapolation may be inappropriate. One very clear difference in the northern section over the main section is that the low velocity Olympic core rocks have been displaced by relatively high velocity material that comes very near the surface, causing a virtually zero velocity gradient from about 15km depth down to the top of the slab. *Ramachandran* [2001] interpreted this shallow structure as Crescent terrane brought close to the surface under the Strait of Juan de Fuca.

Another view of the interrelationships among the velocities, reflector and intraslab earthquakes is demonstrated by Figures 3.7 and 3.8. Although mentioned previously, the generality that the up-dip velocities at the reflector are closer to 7km/s and the down-dip velocities are near 8km/s becomes clear. The velocity contours grossly resemble the depth contours of Figure 3.4, as evidenced by the observation that the 7.5km/s contour on the reflector closely mimics the 40km depth contour, albeit with some high wavenumber structure. Histograms of the velocities where the intraslab earthquakes occur coded according to the definition

given in Section 3.4 also demonstrate the nearly bimodal distribution of the events (Figure 3.8). The up-dip events that occur clearly beneath the reflector peak in distribution between 7.6 and 8.1km/s, whereas the down-dip events that occur unambiguously above the reflector lie in between 7 and 7.5km/s. The ambiguous events, as expected, occupy the full range of observed velocities.
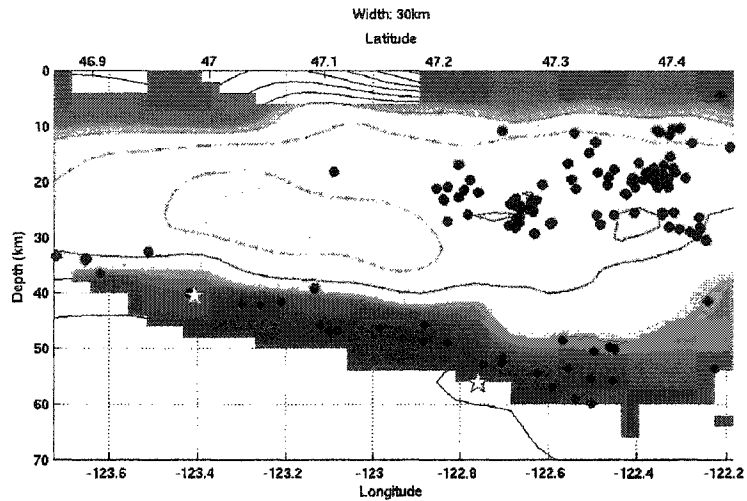
Figure 3.9: Cross-section aligned parallel to relative plate motion (southernmost boxes in Figures 3.4 and 3.5 (A)). Uses same notation as Figure 3.6 except no reflector is shown since it is not constrained here. The Nisqually (right) and Satsop (left) events are indicated by the stars.
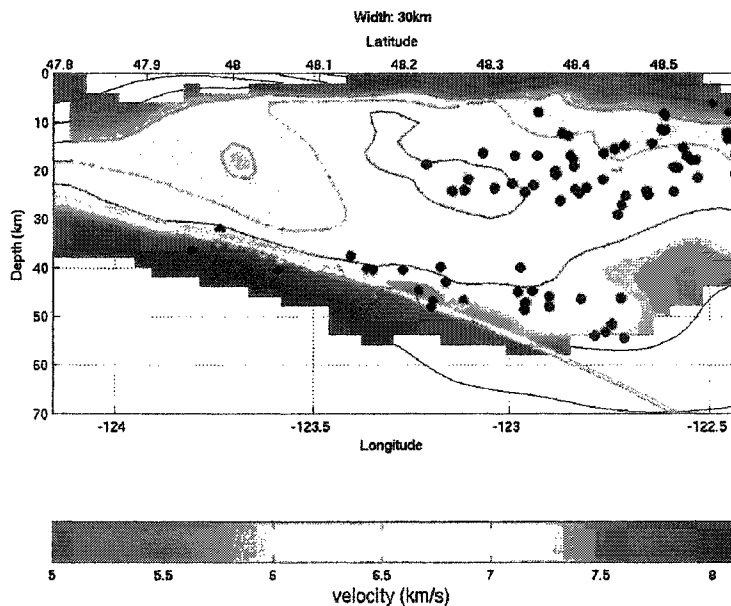
Figure 3.10: Cross-section aligned parallel to relative plate motion (northern boxes in Figures 3.4 and 3.5 (C)). Uses same notation as Figure 3.6.
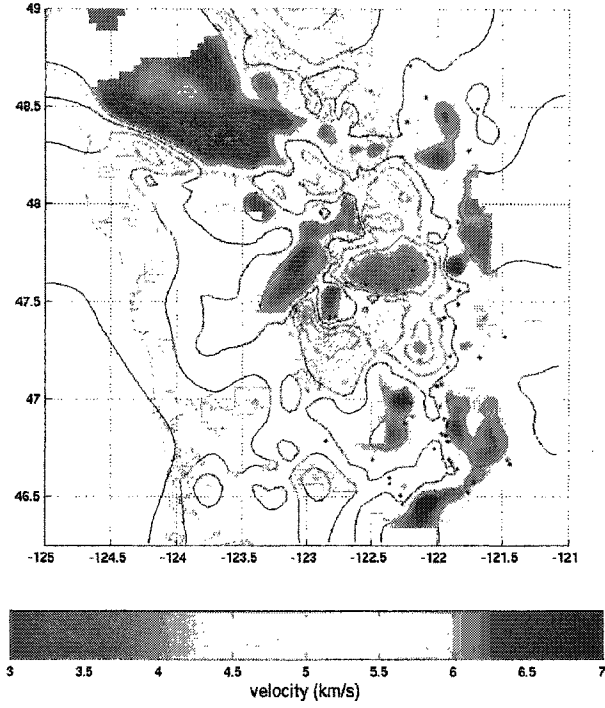
Figure 3.11: 5km depth section
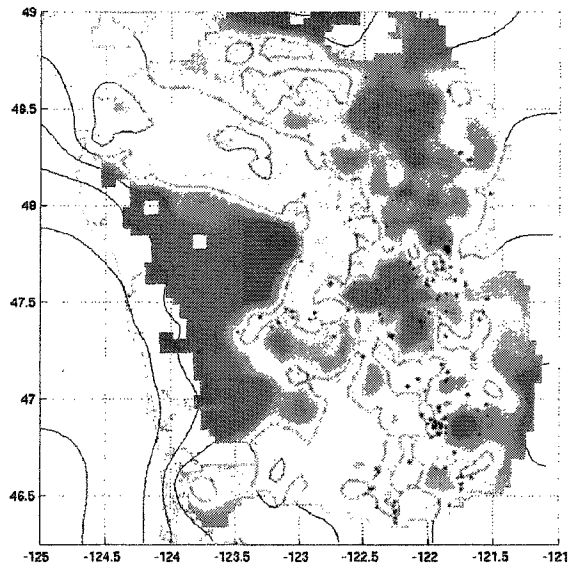
Figure 3.12: 10km depth section. See Figure 3.13 for color bar.
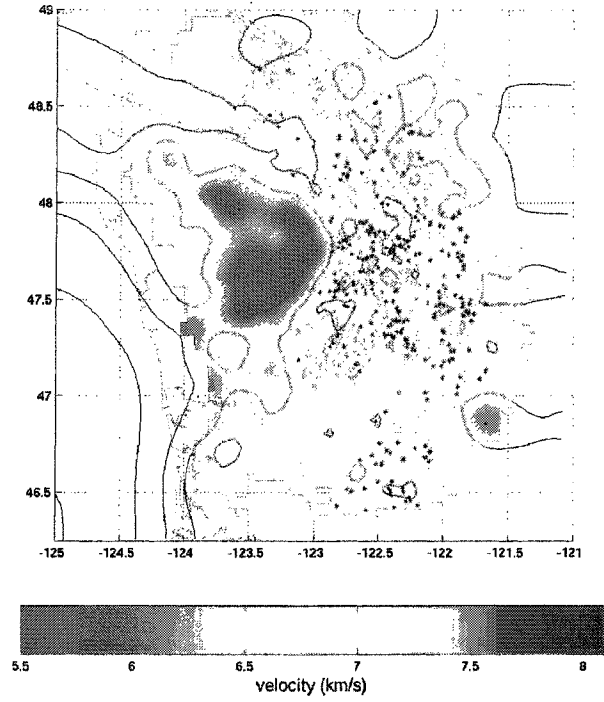
Figure 3.13: 20km depth section
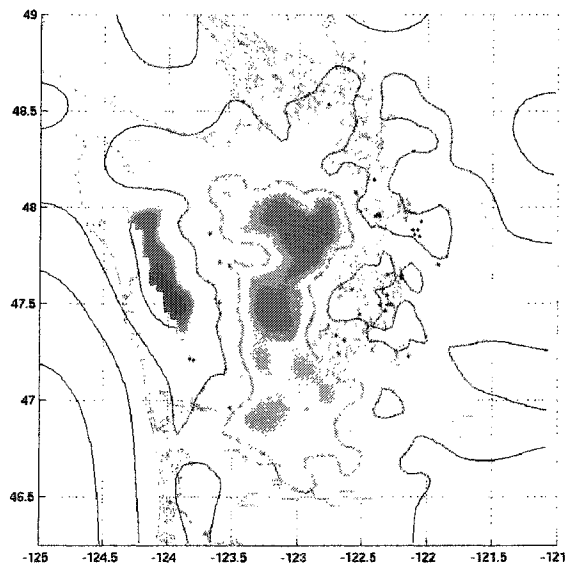
Figure 3.14: 30km depth section. See Figure 3.13 for color bar.
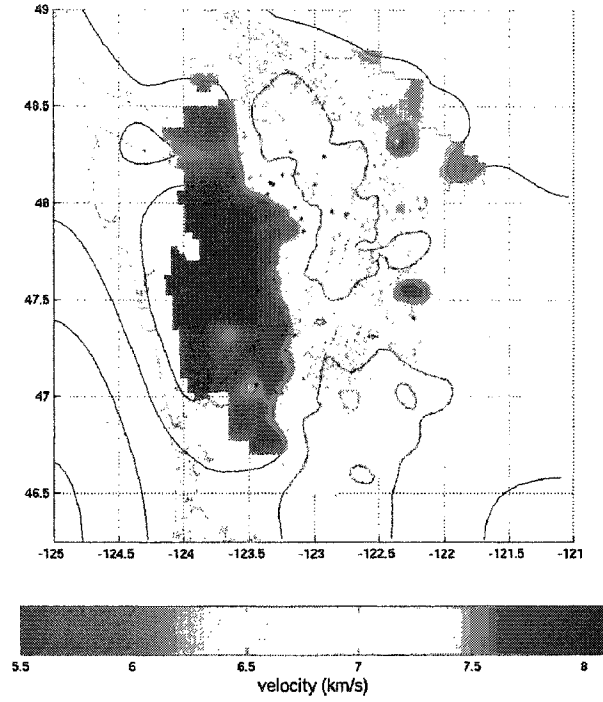
Figure 3.15: 40km depth section
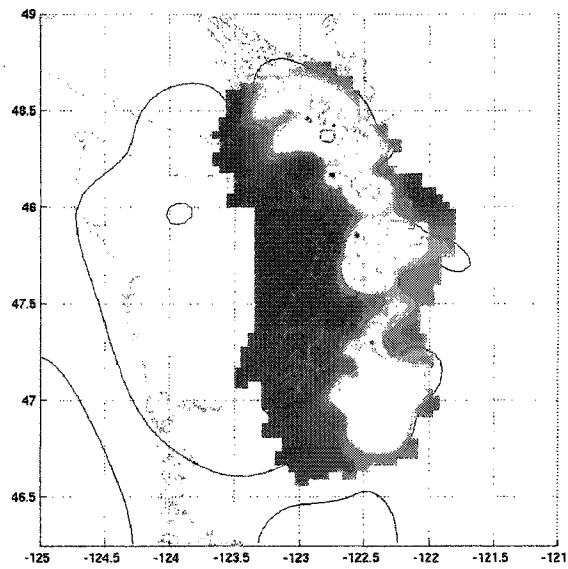
Figure 3.16: 50km depth section. See Figure 3.15 for color bar.

Chapter 4

Resolution and Error Analysis

One of the primary goals of this work is to describe the relationship between the subducting Juan de Fuca slab and the intraslab earthquakes, i.e. are the earthquakes in the subducted crust or mantle? To answer this question, we require knowledge about the fine-scale structure of the slab, i.e. it's location and velocity structure, and about the hypocentral locations of the intraslab earthquakes. These issues are questions of resolvability and error analysis and we perform four categories of analyses to determine our resolution: stability, velocity checkerboard tests, slab velocity resolution tests, and parameter sensitivity. These tests indicate that we have the necessary resolvability in velocity and that the relative error between the reflector position and intraslab earthquake locations is about 2km.

4.1 Stability

One issue in non-linear inversions is dependence on starting model. Linear inversions only have one minimum, so the final model is independent of starting position. Non-linear inversions, however, may have many local minima to which an inversion may converge. This possibility may lead to dependence of the final model on the starting model.

Our starting model consisted of a 1-D velocity model, network hypocenter locations, and a horizontal reflector at 20km depth. The final model, M_f, differed significantly from the

starting model. We tested the stability of the intraslab seismicity by moving the seismicity 10km shallower and 8km deeper than M_f and then re-inverting. When they were moved 10km shallower, the RMS deviations from M_f were 200m in epicenter, 700m in depth for the earthquakes, and 200m in reflector depth following 8 iterations. Mean deviations were 100m in epicenter, 50m in depth and 150m in reflector depth. Four earthquakes had depth deviations of more than 1km with the maximum deviation being nearly 10km. When the intraslab earthquakes were moved 8km deeper, the RMS deviations were 200m in epicenter, 600m in depth, and 200m in reflector depth after 4 iterations. Mean deviations in this scenario were 50m, 20m and 40m in epicenter, depth, and reflector depth respectively. Two earthquakes showed deviations of more than 1km in depth with a maximum deviation of 8km. We also moved the reflector deeper by 10km and re-inverted. The reflector returned to its original position with an RMS of 300m in the region of the model constrained by reflection data. Most of the deviation came from regions on the fringes of the model where data density is low and the smoothing has the most impact. The hypocenters deviated from M_f by less than 300m in this scenario.

To produce a more realistic model, we fixed the velocity at the bottom of the model (78km depth) to 8.1km/s. This avoids unrealistically high velocities extrapolated into regions with no constraints. We fixed the velocity at the bottom of the model to an unrealistically low 7.0km/s to test how much this boundary condition was affecting our model and find that the inclusion of this constraint does not change the model in ways that would affect our interpretation.

4.2   Velocity Checkerboard

Three different checkerboard tests were conducted to examine our resolution of the velocity structure. A checkerboard test consists of adding a regularly varying perturbation, which has the appearance of a checkerboard, to the M_f velocity model. Travel times through this perturbed model are then calculated and noise is added to simulate reality. Noise is randomly selected from Gaussian distributions whose half-widths are consistent with the

standard error estimates for the individual datum, scaled to the real RMS in the data. These simulated times are then used in an inversion using M_f as the starting velocity model. We then subtract M_f from the inversion results and compare the residual with the input perturbation pattern. With perfect ray coverage and appropriate smoothing constraints, the residual will exactly replicate the input perturbation. Due to imperfect coverage, however, perturbations may be smeared, displaced, or reduced in amplitude. Since our velocity model is three dimensional, our checkerboard test is 3-D as well. We use the product of three sinusoids each varying in the three orthogonal directions of the form $V_p = V_0(1 + A\sin(2\pi(x_0 + x)/x_L)\sin(2\pi(y_0 + y)/y_L)\sin(2\pi(z_0 + z)/z_L))$, where V_0 is the M_f velocity model, A is the amplitude of perturbation, x_L, y_L and z_L are the wavelengths of the perturbations in the x, y, and z directions respectively, and x_0, y_0 and z_0 are shifts in their respective directions. This equation provides for percent velocity perturbation to the background velocity, V_0, given by A. In all of our tests, A is set to 0.10, i.e. 10% velocity perturbation, and x_0, y_0 and z_0 are set to zero unless otherwise mentioned.

One of the tests consisted of a high-resolution checkerboard with 32km horizontal and 16km vertical wavelengths (Figure 4.1). The resolution (Figure 4.1) is generally very good (near 100% return) in the upper 20km where fixed sources are located and in regions of shallow North American crustal seismicity. However, the resolvability is poor at this scale under the Olympic Mountains and within the subducting slab, even in the vicinity of intraslab earthquakes.

Since we are primarily interested in the large scale structure of our model, we also conducted two tests at 64km horizontal and 32km vertical wavelengths. The only difference between these two tests is that $y_0 = 16$km for the second, i.e. they are offset by 16km in the N-S direction. The resolution for several depth sections are shown in Figures 4.2, 4.3, 4.4, and 4.5 and four cross sections are shown in Figures 4.6, 4.7, 4.8 and 4.9. In each of the cross sections, the one which has the highest amplitude input perturbation is displayed. Overall, the resolution is much improved at this scale with most regions replicating the pattern well and many showing good amplitude returns as well, especially in the center section which contains the most data (Figure 4.7). Our resolvability, however, is poor to nil east of the
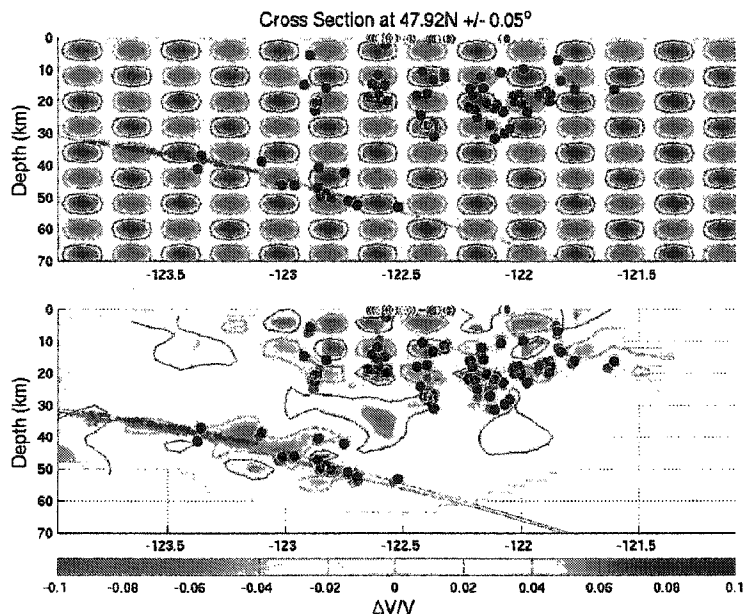
Figure 4.1: Example cross-section from the high-resolution velocity checkerboard test (section b in Figure 4.2). Input perturbation model (top) and retrieved model (bottom) with input hypocenter positions (black) and retrieved (magenta) connected by a thin yellow line, input reflector (red) and retrieved reflector (blue). Contours are at 0.025 $\Delta V/V$ intervals, excluding 0.0

shallow North American crustal events. Again, the resolution is excellent near the shallow seismicity and fixed sources. In the vicinity of the slab, near the intraslab seismicity and even beneath the reflector, the returned amplitudes and pattern are much improved at this scale and are comparable to the input. However, the resolution within the Olympic core, although improved at this scale, is only moderate. The pattern is well retrieved here, but amplitude returns are poor with a fair amount of smearing of structure.

Our resolvability at depth is strongly dependent on the concentration of intraslab earthquakes. To the south of the lineament of seismicity, concentration is low and, accordingly, resolvability is poor. The southern and central portions of the Olympic Peninsula exhibit the highest resolvability due to the sheer number of intraslab events there. However, our resolution decreases substantially to the north primarily due to the lack of events. The

shallow resolution in the north and south also suffers from the lack of seismicity in the region. The only saving grace for the upper 10 or so kilometers is the SHIPS active source lines within the Straits of Juan de Fuca and in the waterways surrounding the San Juan Islands in the north and the SW Washington line in the south. Seismicity in the west Rainier seismic zone and surrounding Mt. Saint Helens improve the shallow resolution in the southeastern portion of the model as well.

4.3 Slab Resolution

Overall, the checkerboard tests reveal good resolvability within our primary region of interest, i.e. within the subducting slab beneath the Olympic Peninsula, especially at the larger length scales. Although velocity checkerboard tests are important for understanding the resolvability of the velocity model, they only ascertain to what extent the model can "see" cubes on the scale of half a wavelength of the checkerboard. We expect, however, that the structure of the subducting slab should be nearly 1-D perpendicular to the slab surface. It is this type of slab resolvability that primarily interests us when interpreting the slab velocities in relation to the reflector and intraslab seismicity. We are especially interested in whether we could resolve a low velocity zone, if one existed, as has been observed in other subduction zones, albeit at depths greater than 50km (Section 5.5), but is not apparent in our results (Section 3.5).

To test our resolvability in the slab, we perturbed the M_f velocity model by -1km/s above the reflector in a 4km thick zone with 4km thick cosine tapers above and below, giving an effective width of $\sim$8km (Figure 4.10). Theoretical travel times were calculated through this perturbed model and noise added in the same manner as described in Section 4.2. This model was inverted with the simulated travel-time data and M_f as the starting model. Returned structure, although slightly smeared, and amplitude (Figure 4.10) indicate good resolution within the crustal portion of the slab in regions with intraslab seismicity. Most regions of the slab above the reflector with intraslab events recover at least 50% of the amplitude with several areas recovering 75%.
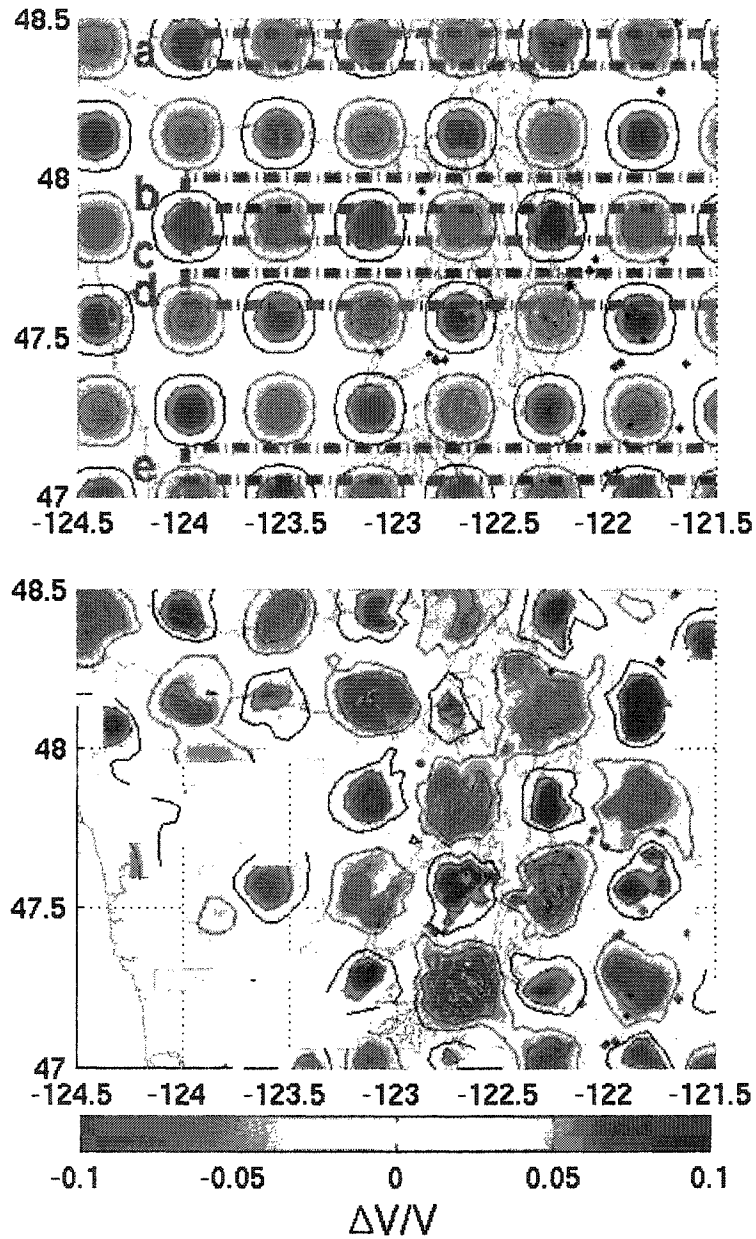
Figure 4.2: 5km depth section low resolution velocity checkerboard. Input (top) and retrieved model (bottom) with input hypocenters (black dots) and retrieved (magenta). Contours are at 0.025 $\Delta V/V$ intervals, excluding 0.0. Cross-sections are labeled by the boxes. Note that box d occupies the bottom half of box c.
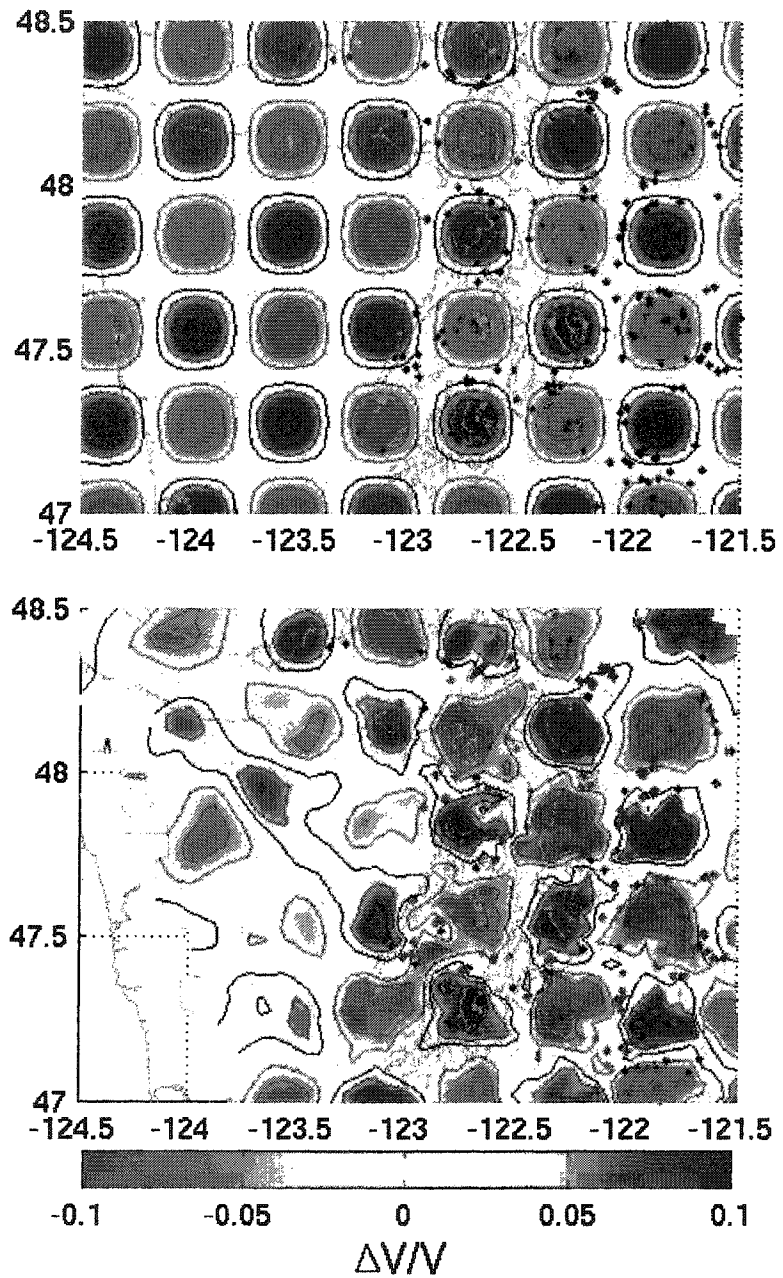
Figure 4.3: 16km depth section velocity checkerboard. See Figure 4.2 for key.
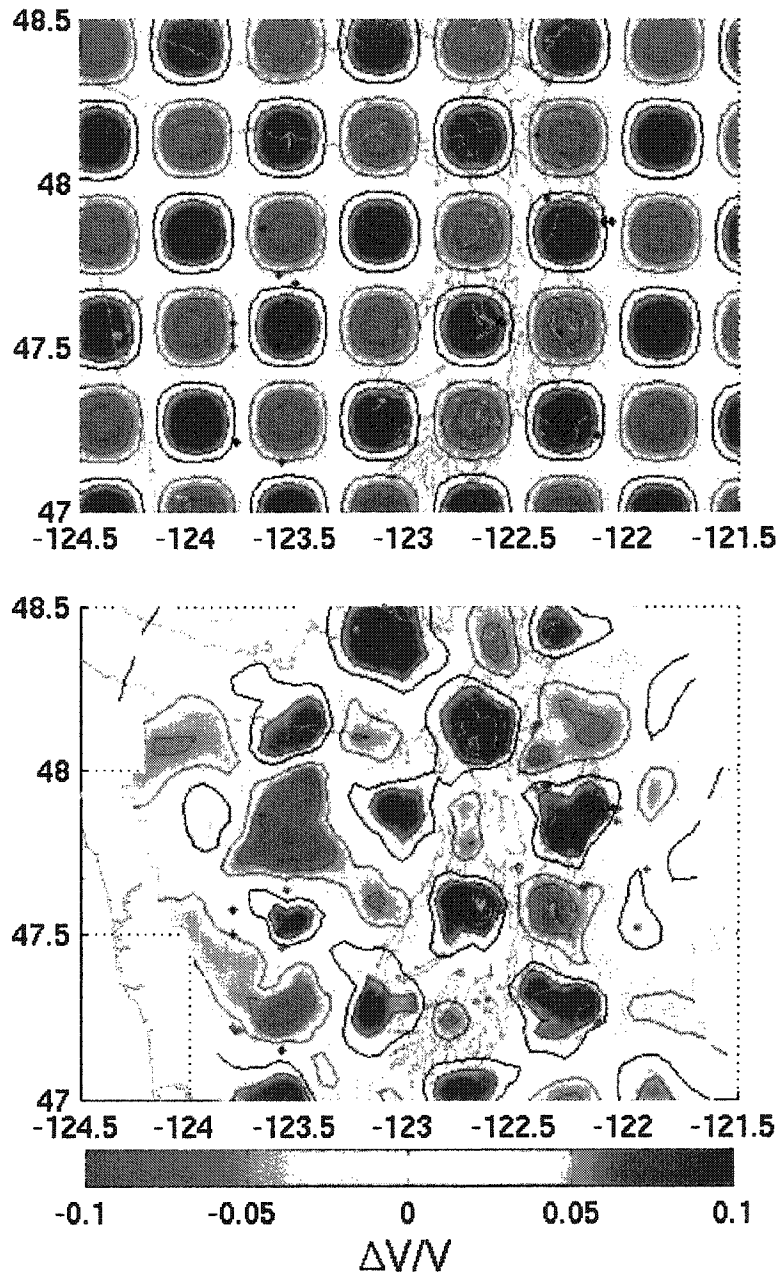
Figure 4.4: 32km depth section velocity checkerboard. See Figure 4.2 for key.
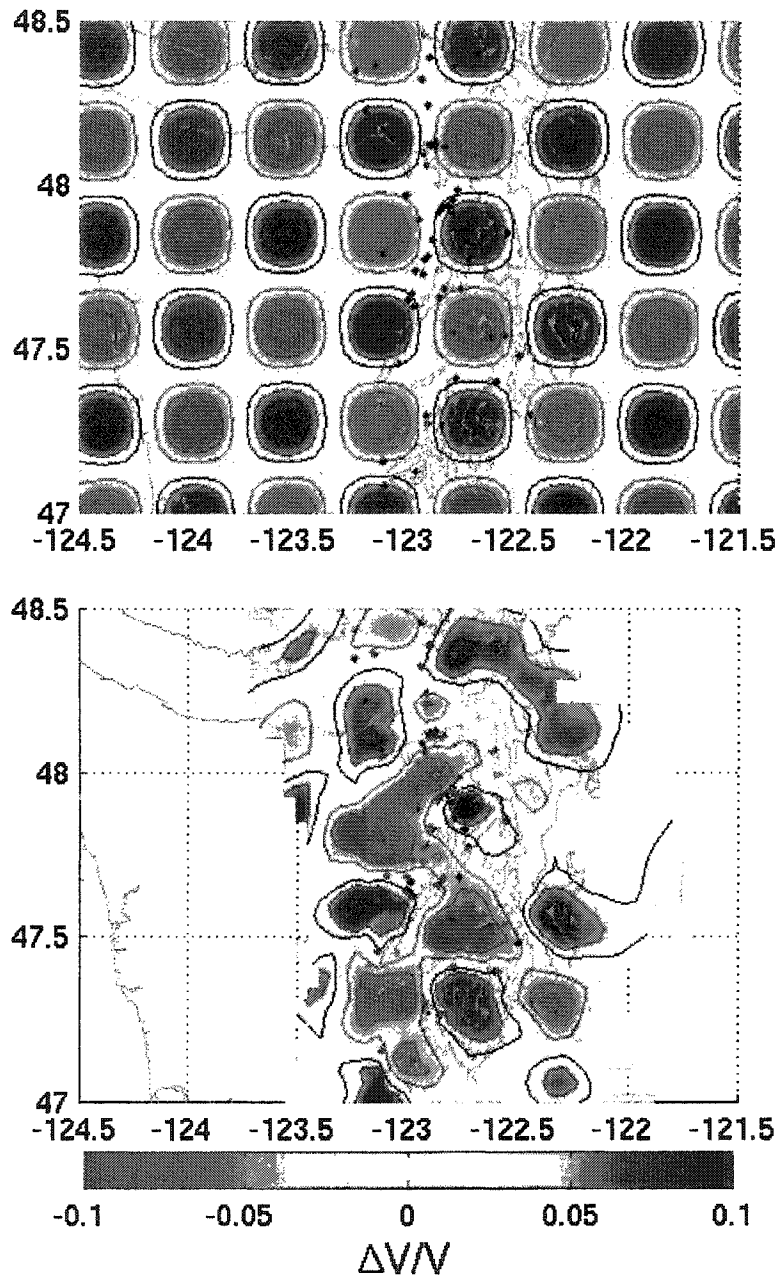
Figure 4.5: 48km depth section velocity checkerboard. See Figure 4.2 for key.
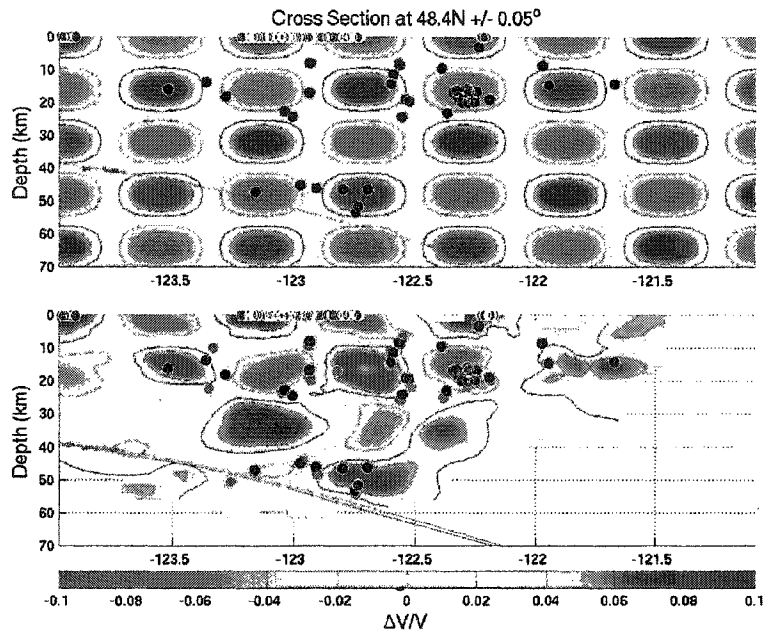
Figure 4.6: Cross-section from the low-resolution velocity checkerboard test (section a in Figure 4.2). See Figure 4.1 for key.
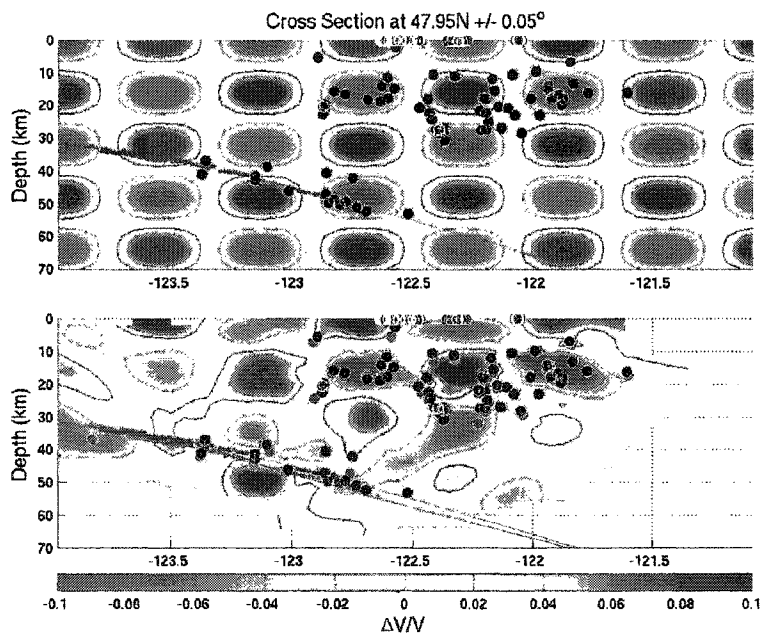
Figure 4.7: Cross-section from the low-resolution velocity checkerboard test (section b in Figure 4.2). See Figure 4.1 for key.
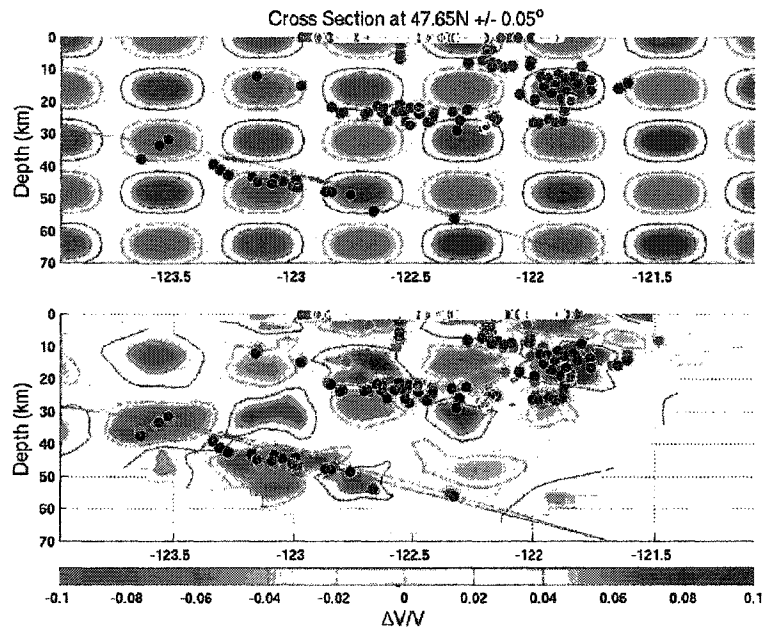
Figure 4.8: Cross-section from the low-resolution velocity checkerboard test (section d in Figure 4.2). See Figure 4.1 for key.
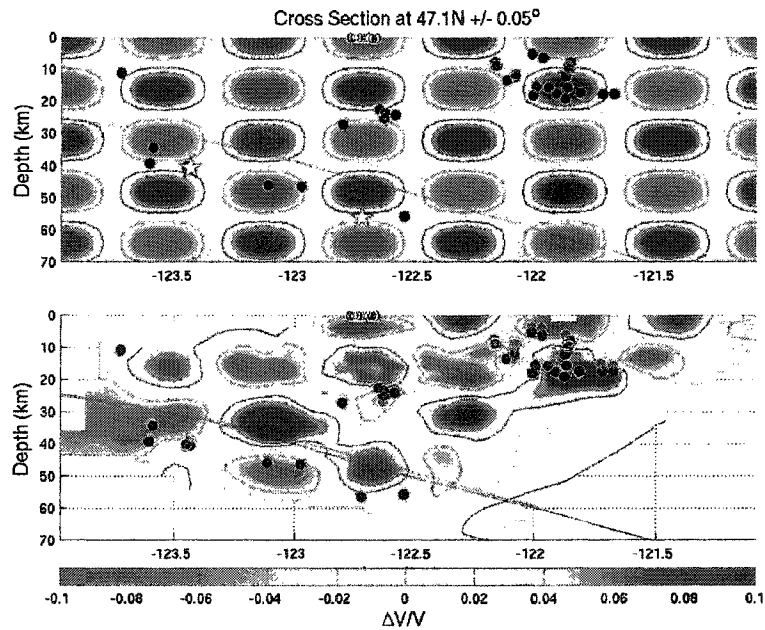
Figure 4.9: Cross-section from the low-resolution velocity checkerboard test (section e in Figure 4.2). See Figure 4.1 for key.
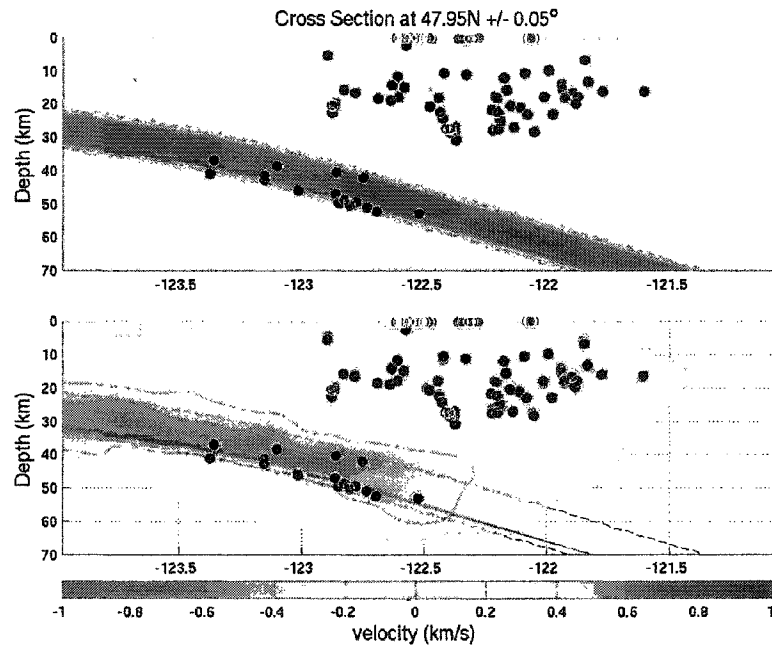
Figure 4.10: Slab velocity resolution above the reflector. Imposed perturbation to the M_f velocity model (top) and retrieved perturbation (bottom). Perturbations are coded according to color bar. Contours are at 0.25 km/s increments starting at -0.25 km/s. The dashed line in both figures encloses the perturbation envelope in top figure. Black circles, red line and red dots are M_f input hypocenters, reflector and bounce points respectively. Magenta circles, blue line and blue dots are retrieved hypocenters, reflector and bounce points respectively.
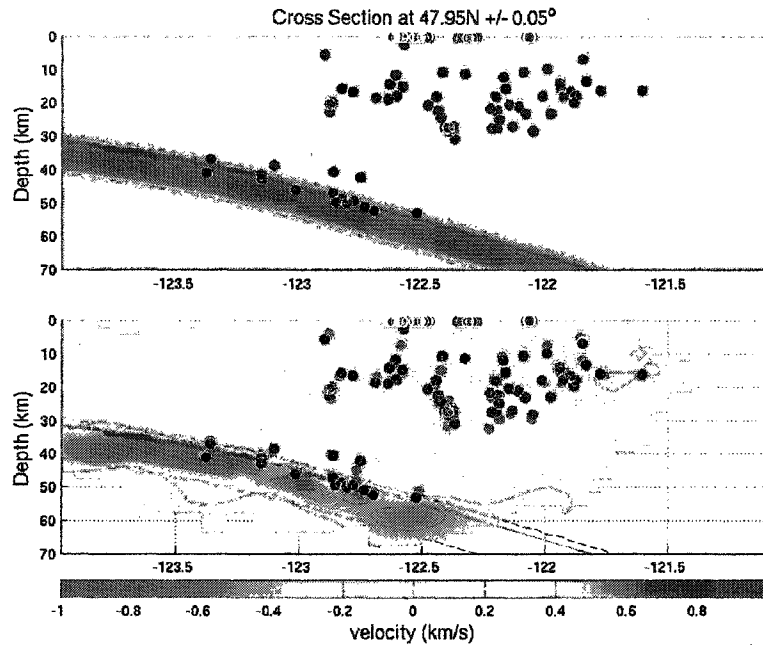
Figure 4.11: Slab velocity resolution below the reflector. Imposed perturbation to the M_f velocity model (top) and retrieved perturbation (bottom). See Figure 4.10 for key.

To determine the velocity resolution beneath the reflector, i.e. within the uppermost mantle portion of the slab, we performed the same test as above but, in this case, perturbed the structure beneath the reflector. The returned model from this test (Figure 4.11) actually indicates better resolvability beneath the reflector than above. The extent of the perturbation is confined to the appropriate region and only shows slight smearing due to smoothing. Much of the area recovers significantly over 50% amplitude, with a fairly large region recovering over 75% and up to 90% in places. We believe the reason for better resolution below the reflector is primarily due to the fact that, since it is a high velocity region in the model, rays from the intraslab earthquakes sample this region more than above the reflector and also that this perturbation pattern is more amenable to the smoothing constraints. In fact, the high density of rays beneath the reflector is clearly evident in a ray density plot (Figure 4.12). These tests indicate we have sufficient resolvability in velocities both above and below the reflector to support our interpretations.
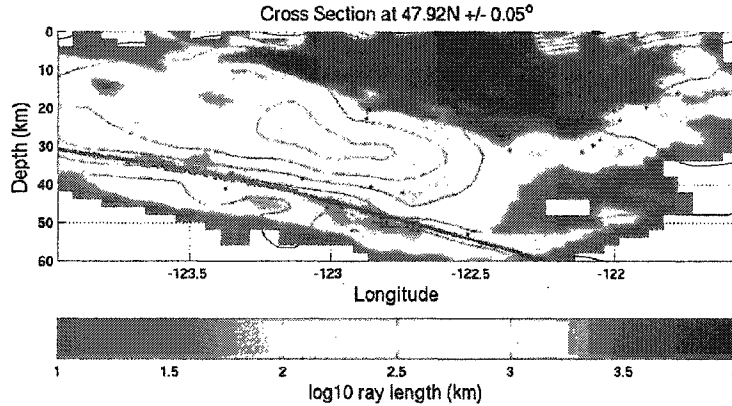
Figure 4.12: Example ray density cross-section. Densities are coded according to the color bar and are the sum of the weighted ray lengths at each node. Earthquakes (black dots), reflector (red line), bounce points (blue dots), and velocities (contours at 0.5km/s intervals) are also shown for reference.

4.4 Parameter Sensitivity

Several sensitivity tests were performed to determine the reliability of the intraslab earthquake and reflector positions. These include confidence ellipses for the earthquakes and also relative sensitivity measurements between the earthquakes and reflector.

4.4.1 Earthquake Confidence Ellipses

One standard means of evaluating individual earthquake error is by calculating error ellipses. In order to calculate an error ellipse, we computed the weighted variance of the travel-time residuals for an event hypothetically assuming that the event location was at each of the grid nodes within our model, giving a full range of possible x, y, and z locations. The optimal origin time for each grid node was determined by finding the time which gave a mean weighted residual of zero for that node. The error ellipse is defined as the region in space where the weighted variance is not significantly different from the M_f variance in a statistical sense. We used 95% confidence interval F-tests to determine the cutoff variance ratio significance levels, assuming errors in the data are statistically independent.
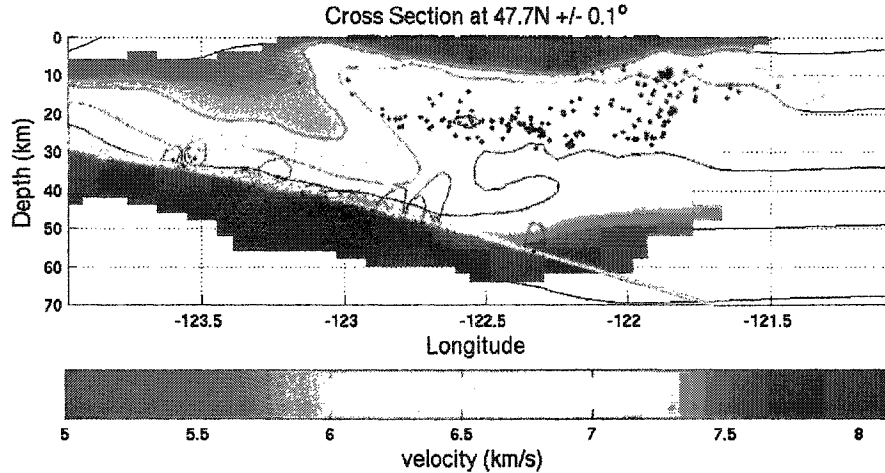
Figure 4.13: Error ellipses for the intraslab earthquakes (blue ellipses) in cross-section c of Figure 4.2. All other symbols are the same as Figure 4.1. Note: The reflector line represents a mean position over 0.2° latitude. Thus, the relative locations between the reflector and intraslab events may appear inaccurate. See Figure 3.5 for accurate relative locations.

As described in Section 2.2, we used the travel time calculated from the ray path instead of directly using the times from the finite-difference calculator due to accuracy concerns. However, because of the necessity of using a grid search in calculating the error ellipses, we could not employ the ray-path travel-time calculation scheme due to computational limitations and opted instead to utilize finite-difference times. This accounts for some of the discrepancy between the error ellipses and the M_f earthquake locations shown in Figure 4.13. Although a majority of the earthquakes have M_f locations much less than a grid node away from the minimum variance node determined by the grid search, a minor fraction had minima just beyond a grid node distance from the M_f position.

Overall, the intraslab earthquakes show error ellipses that are less than 2–3km in diameter. Some earthquakes, however, are exceptions showing ellipses with lengths of 10km or more. In general, ellipses for intraslab events occurring above the reflector do not appear significantly larger or smaller than mantle events. Most of the events show a characteristic bias in the ellipses to shallower depths. Although individual events could possibly locate on the opposite side of the reflector than they appear in M_f, the probability that they would

all locate at or beyond their ellipses, e.g. moving all the earthquakes below the reflector to above it, is very small and, indeed, as shown in the next section, not permitted by the data.

4.4.2 Relative Sensitivity

The inversion results, M_f, provide us with reflector and earthquake locations that minimize the misfit to the data and constraints, χ_f^2. However, since we are primarily interested in the relative positions of the intraslab earthquakes and the reflector, we desire to know what range of models yield χ^2 sufficiently close to χ_f^2 to be considered equivalent to M_f in a statistical sense. Instead of determining error estimates for each of the model parameters, as can be obtained from Jackknife [*Efron and Tibshirani*, 1993] or similar methods, we aim to answer specific questions such as "Can we find a statistically acceptable model with the reflector 5km shallower than M_f?" In order to answer this type of question we run a series of inversions, each fixing a particular set of parameters and allowing the remaining parameters to be free. For example, for the above question, we move the reflector up 5km, fix its position, invert for the remaining parameters, and then compare this model's variances to those of M_f.

For M_f, as described before, we use standard statistical weighting for our data, meaning each datum is weighted by the inverse of its estimated standard error. Since we have approximately four times less reflection data than deep earthquake data, the deep earthquakes as a whole will have more weight in the inversion than reflection data. Consequently, we might expect the deep earthquakes to control the structure to the extent that these tests will show strong reflector variance and weak earthquake dependence. Indeed, this is the picture that occurs. To alleviate this problem, we reweight the reflection data so that it has the same overall weight in the inversion as the deep earthquakes. We first run a full inversion with only the weights altered, allowing all parameters to adjust to the new weighting. The outcome is identical to M_f, i.e. after the first iteration, the change to M_f was within our convergence criteria (see Section 2.3.2). We then proceed with the above parameter fixing and inversion analysis with the reweighted reflection data.

We moved the deep earthquakes by $-5, -2, +2$, and $+5$km in depth, fix their depths and invert for all other parameters, including the latitudes, longitudes and origin times for the deep events. The variances of these tests relative to M_f are shown in Figure 4.14 independently for the intraslab earthquakes and reflector. Although the intraslab earthquake travel-time residual variance increases by nearly 40% over M_f when the events are fixed 5km shallower, which in itself is enough to disqualify this model, the reflection data, with a three-fold increase in variance, are indignantly opposed to the model. However, displacing the intraslab events 2km shallower rouses less, but still modest, protest from both sources. The variance for the intraslab events is increased by 20% while that of the reflector is up 25%. This level represents the maximum allowed movement shallower for the intraslab events on average. Now, if we force the intraslab events deeper than M_f, we actually observe that the model is better able to fit the reflection data than in M_f, but at the expense of the deep-event travel times. Even by moving the earthquakes down 2km, the variance for the earthquakes has increased by 25%, which limits the maximum depth extent of the earthquakes to this value. Thus, we have confined the average depths of the intraslab events to ± 2km of their M_f position. The sharp increase in velocity model roughness (Equation 2.5) beyond ± 2km also accords with this conclusion (Figure 4.15).

We perform the same test as above with the reflector by moving the reflector surface by $-5, -2, +2$, and $+5$km in depth, fixing the depth and inverting for all other parameters. Although the reflector surface is not allowed to move, the reflection ray paths are able to adjust the velocity model. One interesting aspect of the results from this test (Figure 4.14) is that the intraslab earthquakes travel-time residuals are virtually independent of the reflector position. The reflection data, however, are strongly influenced by reflector position, as expected. A 5km shallowing of the reflector causes the variance for the reflection data to increase over two-fold, ruling out this possibility. Moving the reflector up by 2km, on the other hand, only amounts to a 15% increase in variance and is, therefore, the maximum permissible. Moving the reflector deeper, however, increases the variance more dramatically. Even forcing it down by 2km results in an increase of variance of 50% which is intolerably large. Therefore, we interpolate that a deepening of ~ 1km would approximate
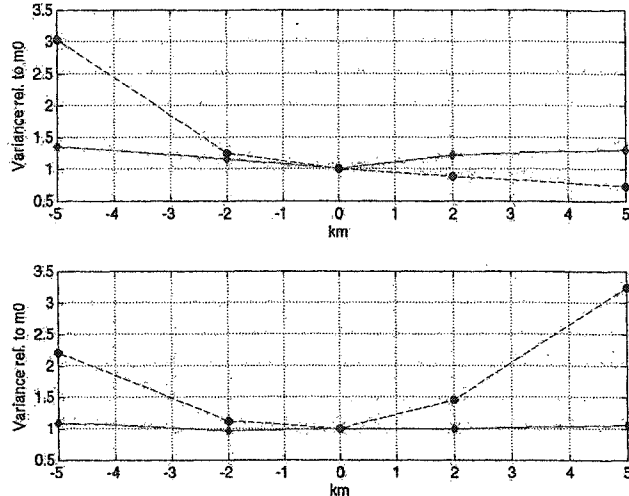
Figure 4.14: Variance ratios relative to M_f for the reflection (dashed) and intraslab earthquake (solid) travel-time data from variations in fixed intraslab earthquake depth (top) and fixed reflector depth relative to M_f (bottom) (see text).

the maximum displacement allowed by the data in that direction. Unlike in the fixed-depth earthquake test, the velocity model roughness is virtually independent of reflector position, only increasing by 1–2% over the range, but does have it's minimum at M_f.

According to standard F-tests, all of the variance increases shown in Figure 4.14 are statistically significant at high confidence levels. Indeed, even an increase of 5% in variance represents a statistically significant increase at 95% confidence for the earthquake data according to standard F-tests. However, F-tests assume statistical independence of the data, which obviously is not the case. Thus, we conservatively estimate that a 20% increase in variance represents a statistically significant level, which corresponds to a p-value of less than 0.1% for both the earthquake and reflector data according to the standard F-tests. To truly compare variances among the different models, technically the roughnesses of each of the models should be the same, which would involve adjusting the trade-off parameter multiple times to find the correct model. However, since all of the fixed-displacement tests generated models that are rougher than the best model (Figure 4.15), the misfit variances in a smoother model would be even larger than those presented here.
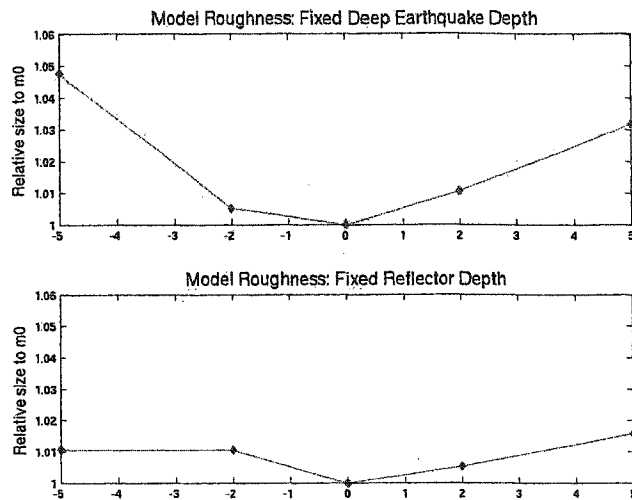
Figure 4.15: Velocity model roughnesses relative to M_f from variations in fixed intraslab earthquake depth (top) and fixed reflector depth relative to M_f (bottom) (see text).
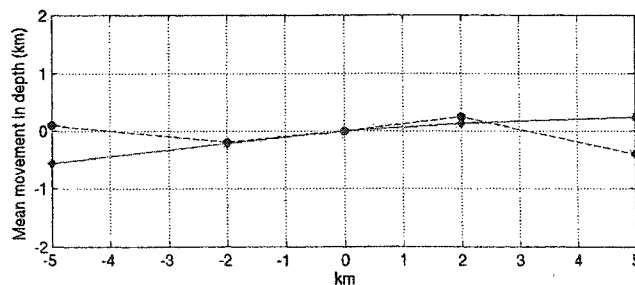
Figure 4.16: Mean displacements of the reflector depth for the fixed intraslab earthquake tests (dashed) and of the mean intraslab event depth for the fixed reflector depth tests (solid).

The interdependence of the reflector and deep earthquake positions on each other is also addressed by these tests (Figure 4.16). If the reflector position was completely tied to the location of the intraslab events or vice versa, then forcing the reflector up by 5km, as an example, would move the earthquakes up by 5km as well. In this case, absolute placement of these elements would be impossible and would call into question the reliability of the relative location of the velocities to the intraslab events and reflector. Obviously, the two data sets are coupled via the velocity structure, but the ability of each data set to independently determine its own location is what we ask here. When we fix the intraslab earthquake depths, we find that the reflector location varies only over a few hundred meters relative to M_f despite changes up to 5km in average intraslab earthquake depth (Figure 4.16). Likewise, the mean intraslab earthquake depth appears relatively insensitive to forced movements of the reflector, although the events do move in sympathy with the reflector. These tests indicate that the reflection and earthquake travel-time data are independently able to determine their average depths.

To test the reliability of the observation that the intraslab earthquakes are below the reflector in certain regions and above the reflector in others, we subdivided the results from the fixed earthquake and reflector tests into smaller regions based upon the latitude and longitude of the earthquake or bounce point. Thus, some regions contain earthquakes that are nearly all above the reflector and others contain events nearly all below. We then compared the variances on a region by region basis. In regions where intraslab earthquakes generally occur below the reflector, they mimic the composite results above. Regions where the earthquakes occur above the reflector show similar results, indicating the ±2km relative error between the reflector and intraslab earthquakes is a general characteristic of the constrained portion of the model.

4.5   Summary

In general, we have the necessary resolvability at the longer wavelengths we are interested in. The velocity structure both above and below the reflector is well resolved especially

in the vicinity of the intraslab earthquakes. The relative error between the reflector and intraslab earthquakes is excellent at ± 2km. Overall, these results allow us to define the precise interrelationship among the slab velocities, intraslab earthquake locations and the wide-angle reflector under the Olympic Peninsula.

Chapter 5

Interpretation

5.1 Introduction

Traditional brittle failure mechanisms of earthquake nucleation dictate that earthquake rupture will occur when the shear stress along a fault overcomes the frictional stress imposed by the normal stress along a fault, given by the Coulomb Failure Criterion (without cohesion) [*Lay and Wallace*, 1995] (Figure 5.1(left))

$$\tau = \mu\sigma \tag{5.1}$$

The normal stress to first order can generally be assumed to be equal to the lithostatic pressure, i.e. the weight of the rock above the fault. Near the surface, lithostatic stresses are relatively small and thus only small shear stresses are necessary to cause fault rupture. Below depths of about 30km, lithostatic stresses and the geothermal gradient conspire to decrease seismic potential according to this mechanism. At high P-T conditions, rocks subjected to deviatoric stresses would be expected to deform ductilely, not by brittle failure [*Kirby et al.*, 1991]. However, earthquakes do occur below this depth and indeed occur to a depth of almost 700km [*Frohlich*, 1989]. Although subducted lithosphere is expected to be cool relative to the surrounding mantle and thus stronger, close scrutiny reveals that the thermal effect is insufficient to produce the observed seismicity [*Kirby*, 1995]. Some other mechanism must be invoked to explain these deep earthquakes.
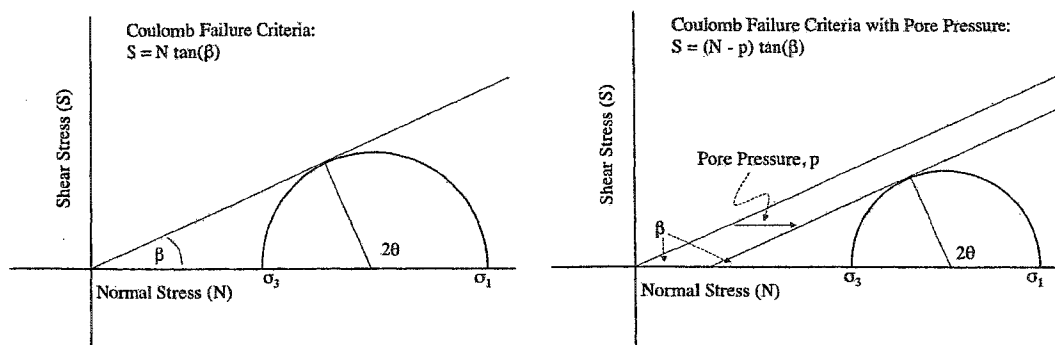
Figure 5.1: Mohr's circle diagrams (excluding cohesion) without pore pressure (left) and including pore pressure (right). $\tan(\beta)$ is the coefficient of friction; σ_1, the maximum compressive stress; σ_3, the minimum compressive stress; θ, the predicted fracture angle relative to the σ_1 direction.

In Cascadia, the intraslab events separate into two groups: those that occur below the reflector up-dip of the 45km reflector depth contour and those that lie above the reflector down-dip of this contour. We interpret the reflector as the subducted oceanic Moho. This places the up-dip events within the oceanic mantle and the down-dip events within the oceanic crust. Dehydration embrittlement, which asserts that volatiles released during metamorphic dehydration reactions reduce the effective normal stresses across faults, allowing slip [Kirby, 1987; Kirby et al., 1991], is invoked to explain both sets of earthquakes. Those events that occur below the Moho reflector within the subducting oceanic mantle are due to dehydration of serpentine, while those that occur within the subducting crust are associated with the basalt to eclogite dehydration reaction.

5.2 Current Intraslab Earthquake Hypotheses

5.2.1 Transformational Faulting

Kirby [1987] discovered a new faulting mechanism, which he dubbed transformational faulting, where a polymorphic phase transformation can cause catastrophic failure along a fault.

In his studies of ice and tremolite (a hydrous mantle mineral), seismic emissions occurred during the metastable transformation of these minerals to their higher pressure polymorphs under deviatoric loading.

Several laboratory experiments [e.g. *Green and Burnley*, 1989; *Houston and Green*, 1995; *Kirby*, 1995; *Kirby et al.*, 1991] suggest that transformational faulting due to the metastable conversion of olivine to spinel offers an explanation for the deepest seismicity. The cold interior of a subducting slab would kinetically hinder the equilibrium transformation of olivine to spinel, which should occur near 410km depth, to metastable depths. The required non-hydrostatic stresses are attributed to differential densities between the already transformed mantle and the cold metastable wedge [*Kirby et al.*, 1991].

5.2.2   Dehydration Embrittlement

Due to the abundance of water at the earth's surface, it is not surprising that many types of hydrous minerals can be found in nature. Hydrous minerals have water molecules incorporated into their crystalline structures, such as in tremolite, $Ca_2Mg_5Si_8O_{22}(OH)_2$ [*Kirby*, 1987]. Like all minerals, hydrous minerals are stable only within a certain range of P-T space. As temperatures increase, hydrous minerals tend to transform into minerals with less or no water content, thus making the newly unincorporated water available as free water in a process known as dehydration. Experiments on several hydrous minerals have shown that the dehydration process embrittles these minerals [*Kirby*, 1995]. For example, *Raleigh and Paterson* [1965] demonstrated that serpentine (a group of hydrous mantle minerals) displays brittle failure at room temperatures, progresses into a ductile regime at intermediate temperatures and reverts to brittle failure at high temperatures where observable dehydration is occurring (Figure 5.2).

The physical mechanism responsible for dehydration embrittlement is believed to be an increase in fluid pore pressure due to the expulsion of water from the mineral [*Kirby*, 1995].
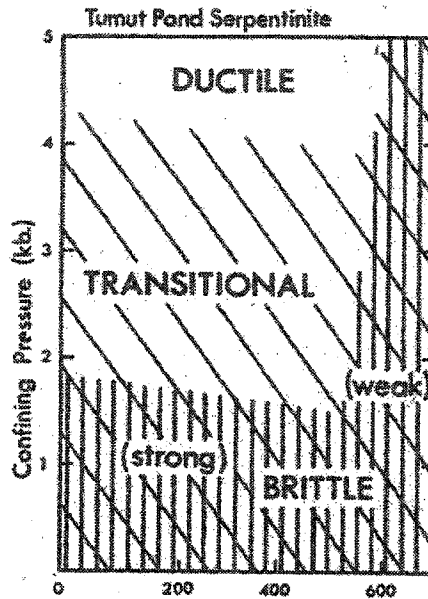
Figure 5.2: Schematic representation of serpentine dehydration embrittlement results taken from *Raleigh and Paterson* [1965]. Temperature (°C) shown along bottom.

If we modify Equation 5.1 to include pore pressure, p, we get (Figure 5.1(right))

$$\tau = \mu(\sigma - p) \tag{5.2}$$

Thus, the pore pressure effectively decreases the normal stress allowing fault rupture to occur even at relatively high lithostatic pressures. Evidence for this pore pressure effect in dehydration reactions was obtained by *Raleigh and Paterson* [1965] in their experiments on serpentine. They found that serpentine deformed ductilely even under dehydration conditions if fluids were allowed to escape. Therefore, slow fluid diffusion rates appear to be a necessary condition for dehydration embrittlement to occur.

At depths less than 250km, dehydration embrittlement associated with the transformation of the basaltic subducting oceanic crust to eclogite has been invoked as a cause of the shallowest intraslab seismicity [*Kirby*, 1995] although other dehydration reactions may also contribute, including mantle serpentine dehydration. The depth at which basalt changes to eclogite at equilibrium conditions is strongly temperature dependent (Figure 5.3) and may be delayed even further in cold slabs due to kinetic hindrance to much greater depths [*Hacker*, 1996].
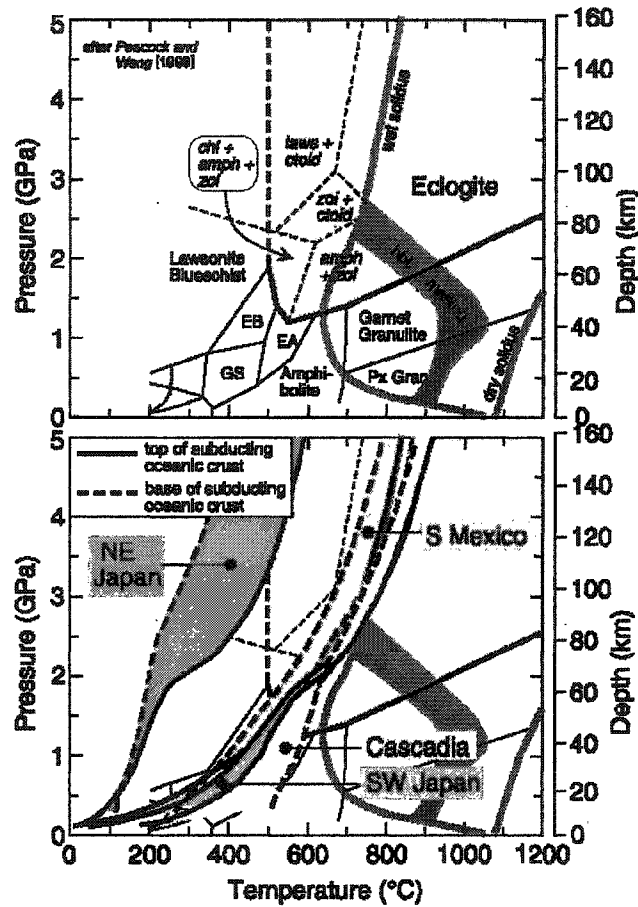
Figure 5.3: (top) Basalt to eclogite P-T diagram and (bottom) Calculated P-T paths for Cascadia (yellow), SW Japan (orange) and NE Japan (blue) obtained from *Peacock et al.* [2002]. For our interests here, basalt is shown unshaded and the eclogite field is shaded in light blue. Solid lines represent top of slab paths and dashed subducted Moho paths. See Figure 1 of *Peacock et al.* [2002] for further information.

The fluids effused from basalt dehydration is invoked as facilitating arc volcanism [e.g. *Kirby et al.*, 1996], and as the source of presumed forearc mantle wedge serpentinization [*Peacock and Hyndman*, 1999] (a review of seismological evidence for mantle wedge serpentinization in Cascadia is provided in *Brocher et al.* [2003]).

Seismologically, untransformed oceanic crust should have velocities less than 7km/s, while eclogitic rocks should have velocities exceeding 8km/s [*Hacker et al.*, 2002]. In addition, *Kirby et al.* [1996] predicted that a systematic variation in focal mechanisms through the subducted crust and into the uppermost subducted mantle may be observed based on the stresses calculated for the resulting densification of the subducting oceanic crust upon eclogitization. Eclogitic rocks are ~15% more dense than basaltic rocks [*Hacker*, 1996; *Kirby et al.*, 1996] and, thus, the oceanic crust must shrink upon transformation. However, the mantle undergoes no appreciable densification, and, assuming the slab oceanic crust and slab mantle do not delaminate, the slab mantle resists the shrinking of the crust. This process is illustrated in Figure 5.4. The final result is a transformed oceanic crust in extension and a much weaker compression within the uppermost subducted mantle. Thus, *Kirby et al.* [1996] predicts normal faulting type mechanisms within the oceanic crust and compressional events within the uppermost mantle.

5.3 Water Content of Oceanic Crust and Upper Mantle

One of the necessary conditions for dehydration embrittlement to occur is that hydrous minerals must be present in the oceanic crust and mantle. Our knowledge of the oceanic lithosphere is limited by the difficulties and expense of direct sampling. Much of our knowledge has been collected from ophiolites, which are believed to be obducted sections of oceanic crust. The limited samplings taken from oceanic drilling boreholes and dredgings and from seismological observations, however, indicate that most likely ophiolites are anomalous pieces of oceanic crust and do not represent the norm [*Coleman*, 1977]. Despite this shortcoming, ophiolites sufficiently mimic oceanic crust and are much more easily accessible for data collection than oceanic crust, making data from them invaluable to our
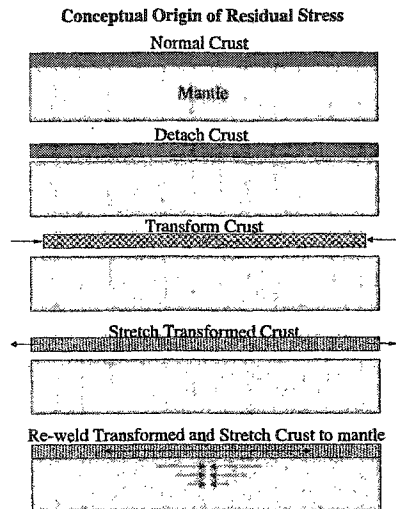
Figure 5.4: Conceptual model for the distribution of slab stresses due to the densification of the basaltic crust upon conversion to eclogite (see text; illustration taken from Kirby during a meeting on Cascadia at Univ. WA in spring 2001, unpublished).

understanding of oceanic crustal structure and formation [*Coleman*, 1977].

The basic structure of oceanic crust consists of a sediment layer, an extrusive volcanic layer primarily composed of pillow basalts, a sheeted dike sequence and a layer of gabbro. Beneath the gabbro is the oceanic Moho followed by peridotitic rocks of the mantle. The presumed structure has been primarily derived from ophiolites but has been supported from incomplete drill sections and dredgings [*Coleman*, 1977]. During and following formation, hydrothermal circulations alter the basic structure locally, forming hydrous minerals. Bulk water content estimates systematically show higher water content in ophiolites than oceanic crust, but tend to show the same variation in water content with higher concentrations in the basaltic layer to lower concentrations within the gabbroic and upper mantle portions [*Alt and Teagle*, 2000]. The mechanisms for hydration of the shallow layers of the oceanic crust are generally well understood, but those for hydrating the lower portions of the crust and mantle remain unclear [*Wang*, 2002], although ophiolites and corings demonstrate that hydration does take place at least into the uppermost portion of the mantle [e.g. *Alt and Teagle*, 2000]. *Peacock* [2001] and *Kirby et al.* [1996] suggested that deep cutting trench-rise normal faults

could allow water to invade the uppermost mantle, *Seno and Yamanaka* [1996] hypothesized water could be implanted in the mantle via plumes, and *Wang* [2002] speculated that the cooling lithosphere could introduce cracks within the mantle where serpentinization would occur. After an extensive literature search, *Hacker et al.* [2002] estimated $\sim 2\%$ weight H_2O for the upper basaltic layer and $\sim 1\%$ weight H_2O in the gabbroic and upper mantle layers. These are bulk constituent estimates and have considerable uncertainty and local variability, preferentially occurring within faulted and fractured zones [*Peacock*, 1996].

5.4 Stresses in Subducting Lithosphere

In addition to fluids, earthquakes associated with dehydration embrittlement require deviatoric stresses in order to occur (Equation 5.2). Deviatoric stresses within the subducting lithosphere include internally and externally imposed stresses and can affect subducting crust and mantle in different ways. Lithospheric bending creates tension in the subducting crust and top portion of the subducting lithospheric mantle and compression within the bottom portion of the mantle [e.g. *Turcotte and Schubert*, 1982]. Deeper, unbending stresses impose the opposite stress regime within the lithosphere. Buoyancy forces acting toward the center of the earth create "slab pull" tension everywhere within the subducting lithosphere, but the magnitude of this stress is dependent on slab dip, with steeply dipping slabs having larger slab-pull stresses than shallow dipping ones [e.g. *Turcotte and Schubert*, 1982]. Due to the curvature of the earth, trenches should delineate a concave land-ward curvature [*Turcotte and Schubert*, 1982], but several subduction zones, including Cascadia, have the opposite trench curvature, which creates membrane stresses within the slab [*Chiao and Creager*, 2002] (see Section 5.7.1). In addition, lithospheric stresses alternate between down-dip tension before megathrust events and compression afterwards due to the build-up and release of stress along the megathrust locked zone [*Wang et al.*, 1995]. Finally, self-induced stresses caused by the 15% volume reduction attendant the basalt to eclogite dehydration reaction creates tension within the crust and much weaker compression in the mantle (Section 5.2.2 and Figure 5.4). These stresses are outlined in Table 5.1.

Table 5.1: Summary of slab stresses

Type	Crust	Top of Mantle
Bending	Down-Dip Tension	
Unbending	Down-Dip Compression	
Slab Pull	Down-Dip Tension	
Membrane	Along-Arc Compression	
Megathrust	Down-Dip Tension before Down-Dip Compression after	
Basalt-Eclogite	In-Plane Tension	In-Plane Compression

5.5 Review of Previous Studies

An obvious corollary to the hypothesis that dehydration embrittlement associated with the basalt to eclogite transformation is the cause of shallow intraslab earthquakes is that the majority of the seismicity should occur within the subducted oceanic crust and that it should occur at the appropriate P-T conditions for the basalt to eclogite transformation. The former has been addressed by various seismological studies in Alaska, northeast Japan and southwest Japan.

5.5.1 Alaska

The Aleutian subduction zone represents an intermediate aged subduction zone with an age of approximately 60Ma for the subducting Pacific plate [*Mueller et al.*, 1996]. Intraslab seismicity is confined to depths less than 250km [*Abers*, 1992; *Helffrich and Abers*, 1997] and is separated into two planes: one near the top of the subducting slab and the deeper within the subducting mantle [*Abers*, 1992]. *Abers* [1992], relocating the best intraslab events in the context of a 3-D model, found that the upper plane of seismicity was generally confined to a zone less than 5km thick and appeared continuous with interplate thrust events up-dip. He interpreted the upper plane of seismicity as occurring primarily within the subducted crust. Further strengthening this claim, *Helffrich and Abers* [1997] modeled PS converted phases observed locally from intraslab events occurring within the upper plane of seismicity as a P-wave traveling within a low-velocity layer and converting to S at the top of the slab

under the station. In contrast, PS phases observed from lower plane events exhibited a high P velocity leg and then S conversion at the top of the slab. As the authors note, this is consistent with the upper plane of seismicity occurring within untransformed subducted oceanic crust to a depth of about 100km.

5.5.2 Northeast Japan

The 150Ma old Pacific plate subducts under NE Japan at a rate of ~8cm/yr, making it one of the oldest and fastest moving, and thus coldest, subduction zones in the world [*Mueller et al.*, 1996; *Igarashi et al.*, 2001]. The intermediate depth intraslab seismicity forms perhaps the best known double seismic zone in the world and extends to a depth of 200km, although deep seismicity occurs down to 670km [*Peacock and Wang*, 1999]. Several investigations of PS, SP, and ScSp conversions at the top of the subducting plate in the depth range 50km to 200km indicate the necessity of a low velocity zone immediately beneath the plate interface [*Hasegawa et al.*, 1978; *Matsuzawa et al.*, 1986, 1990; *Zhao et al.*, 1997] and tomography also reveals the presence of a thin low velocity layer beneath a forced discontinuity coincident with the top of the subducting slab [*Zhao et al.*, 1997]. In addition, *Igarashi et al.* [2001], using relative earthquake relocations and a new technique to determine focal mechanisms for small earthquakes, determined that the seismicity was actually composed of three planes. Although spatially indistinct, the upper plane of the double seismic zone consists of two planes distinguished by their focal mechanisms. The plane nearest the plate boundary (within 5km) tends to consist of normal faulting events (in the slab coordinate system) while the deeper layer primarily contains down-dip compressive events. These findings are concurrent with predictions based on the expected stress variations within transforming oceanic crust due to the basalt to eclogite phase transformation (see Section 5.2.2).

5.5.3 Southwest Japan

The southwest Japan subduction zone, where the 20Ma old Philippine Sea Plate subducts, is more thermally akin to Cascadia than the two subduction zones discussed above. Intraslab

seismicity generally extends to a depth of 60km but some regions exhibit seismicity down to 100km depth [*Shiono*, 1987; *Oda et al.*, 1990; *Seno et al.*, 2001]. Although most regions in southwest Japan exhibit only a single plane of seismicity, a double plane is observed where the Izu-Shichito Ridge is subducting under the Kanto district [*Seno et al.*, 2001]. Throughout the region with a single plane of seismicity, observations generally suggest the seismicity is occurring within the subducted oceanic crust. *Fukao et al.* [1983] and *Oda et al.* [1990] observed secondary arrivals consistent with trapped waves within a low velocity oceanic crust and used these observations to argue that these intraslab events are occurring within the oceanic crust. However, *Seno et al.* [2001] argues that at least some intraslab events do not occur within the subducted crust but within the subducted mantle since these events display no trapped phases. These authors interpret the mantle events as being associated with serpentine dehydration. Unfortunately, tomography [*Zhao et al.*, 2000] within the region is too low resolution to provide any definitive solutions to this problem, indicating a nearly 20km thick low-velocity zone encompassing the intraslab seismicity throughout most of southwest Japan [*Seno et al.*, 2001].

5.5.4 Comparison of NE and SW Japan

The majority of the intraslab seismicity discussed in the previous three sections appears to occur within the subducting oceanic crust, as predicted by the basalt to eclogite transformation, with the possible exception for SW Japan. One distinction that should be made among these three regions is the scale over which the various studies were performed. Both in Alaska and NE Japan, the region of interest extended to approximately 200km depth but with little attention focused on the upper 50km. However, nearly all the events in SW Japan, and in Cascadia as well, occur shallower than 60km.

Peacock and Wang [1999] address the question of whether the seismicity occurs under the appropriate P-T conditions for the basalt to eclogite transformation by comparing seismicity and calculated P-T paths in NE and SW Japan. Based on their thermal modeling, the NE Japan subducted oceanic crust begins to enter the eclogite field at $\sim$100km depth

and does not fully enter the eclogite field by their maximum modeling depth of 160km (Figure 5.3). In contrast, the SW Japan oceanic crust fully enters the eclogite field by 50–60km depth. These respective depths compare favorably with the maximum depth extent observed in NE and SW Japan (Sections 5.5.2 and 5.5.3). However, intraslab seismicity occurs in both of these subduction zones at depths shallower than expected for the basalt to eclogite transformation, suggesting that some other processes besides the basalt to eclogite transformation is controlling these events.

5.6 Interpretation

Although the basalt to eclogite phase transformation explains many of the first order observations in the shallow intraslab seismicity, it does not account fully for mantle earthquakes and earthquakes occurring outside the appropriate P-T conditions for the transformation. This has important earthquake hazard implications for Cascadia. If the basalt to eclogite transformation were the entire story, then the maximum earthquake one would expect would fit entirely within the oceanic crust, geometrically limiting the magnitude to ∼7. However, if other processes are involved such that intraslab earthquakes could occur within the subducted mantle, the maximum earthquake size could be an unit of magnitude greater.

We base our interpretation that the reflector is the subducted Moho on two major observations. First, the reflections are only seen at wide-angles (Section 2.1.2 and Figure 2.6), indicative that this reflection represents an increase in velocity. Although the smallest reflection incidence angles are about 50°, which would yield a 30% increase in velocity, the majority of rays reflect between 60°and 70°incidence, which computes to ∼15% increase in velocity, consistent with a jump from 7km/s to 8km/s. Secondly, the velocity model indicates strong increases in velocity with depth in the vicinity of the reflector, reaching typical mantle velocities just below the reflector (Section 3.5). We observe that the reflector lies between 7km/s up-dip and 8km/s down-dip (Chapter 3 and Figure 3.7). According to theoretical v_p calculations based on average hydrated oceanic crust (2% H_2O weight), oceanic crust should have velocities in the upper 6km/s range [Hacker et al., 2002] (Fig-
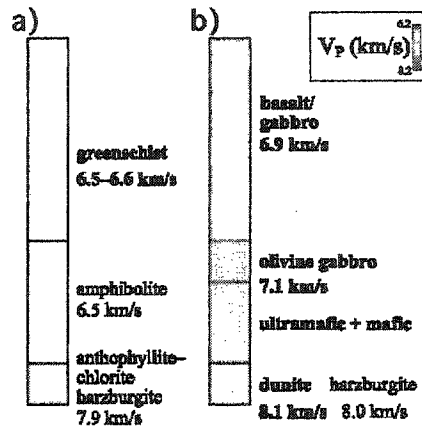
Figure 5.5: a) Calculated P velocities assuming $P_{H_2O} = P_{lithostatic}$ for hydrated oceanic crust and uppermost mantle (harzburgite portion). b) Calculated P velocities assuming anhydrous oceanic crustal and upper mantle mineralogy. Figure modified from *Hacker et al.* [2002].

ure 5.5). Variably hydrated upper mantle (0.5-1.5% H_2O weight) should have P-velocities in the upper 7km/s range. Once crustal eclogitization begins, crustal P-velocities will approach 8km/s, while dehydration of mantle will cause upper mantle velocities to approach typical mantle velocities of 8.1km/s. We would expect the Moho to lie in velocities which average the crustal and upper mantle velocities since our velocity model is smooth with no discontinuities. Thus, updip model Moho velocities, i.e. in regions containing completely untransformed crust, should approximate lower 7km/s while downdip velocities, in regions with transforming oceanic crust, should approach 8km/s. These conjectures agree well with the observed velocities at the reflector and, consistent with our interpretation that the reflector is the subducted oceanic Moho. Corroborating our interpretation, recently *Nedimovic et al.* [2002] reinterpreted the "F" reflector observed on LITHOPROBE data as the subducted Moho. This reflector is consistent in depth with our reflector where the data overlap. In addition, *Trehu et al.* [2002] interpreted the arrivals corresponding to our reflector as PmP arrivals and our interpretation is consistent with the general observation that oceanic Moho reflections are the most common observations at wide-angle (Brocher, personal communication).
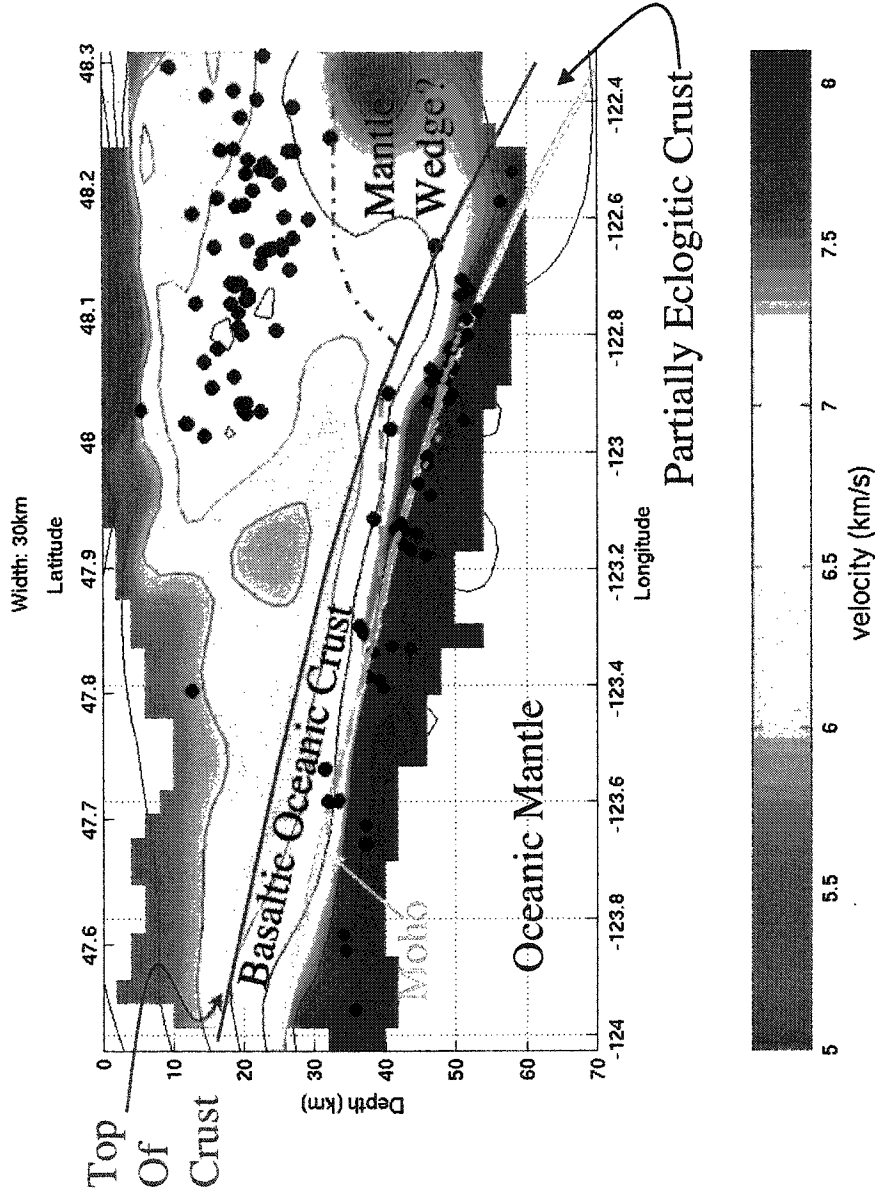
Figure 5.6: Same cross-section and symbols as Figure 3.6 with added interpretation. Red line (top of subducting slab) is drawn 7–8km above the reflector.
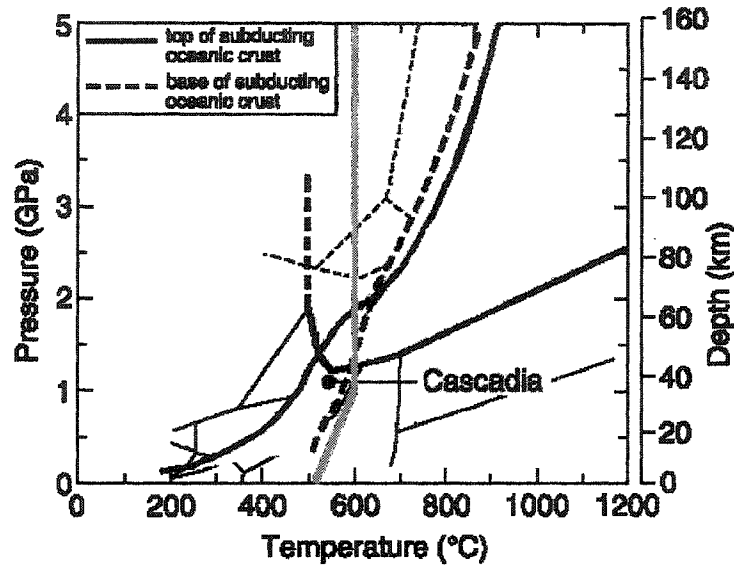
Figure 5.7: Same as Figure 5.3 except modified to only show Cascadia and to indicate the approximate serpentine dehydration curve (green line) [*Hacker et al.*, 2003].

Given the reflector is the oceanic Moho, this places the most up-dip seismicity as generally beneath the Moho and the down-dip seismicity as generally above the Moho. In fact, as discussed in the results and error analysis chapters (Chapters 3 and 4), no unambiguous intraslab events occur above the reflector where the reflector is shallower than 40km depth. Deeper than 40km, the seismicity becomes mixed and eventually tends to occur above the reflector at depths greater than 50km. Due to our decrease in resolution and lack of firm reflector constraint at depths much greater than 50km, the data do not necessarily preclude the possibility of events occurring beneath the reflector where the reflector is deeper than 50km, but it does necessitate earthquakes occurring above the reflector in that region. The most important observations are that the intraslab events occurring up-dip of the 40km reflector depth contour occur beneath the Moho and at 40km depth and greater, subducted crustal events begin to occur (Figure 5.6). The onset of oceanic crustal seismicity at 40km depth coincides well with the predicted depth for the onset of eclogitization from *Peacock et al.* [2002] for the thermal structure of Cascadia (Figure 5.7). This correlation is in accordance with dehydration embrittlement associated with the basalt to eclogite phase transformation.
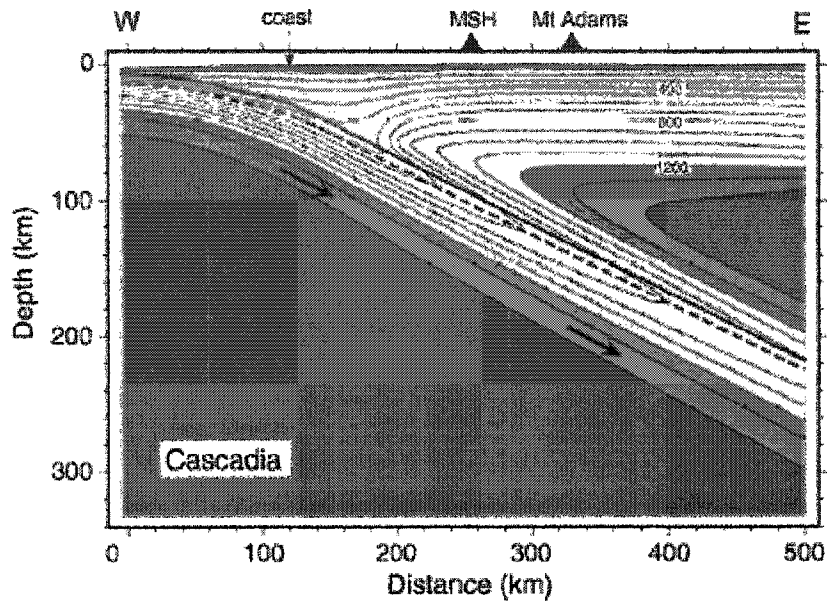
Figure 5.8: Calculated thermal model of Cascadia (temperatures in °C). Modified from *Peacock et al.* [2002].

The intraslab seismicity that occurs up-dip of 40km beneath the Moho, however, cannot be associated with the basalt to eclogite dehydration transformation. The uppermost mantle can be variably hydrated with 0.5–1.5% H_2O by weight. The hydrated portions of the uppermost mantle would consist of serpentine, which, as discussed in Section 5.2.2, has been observed to embrittle under dehydration conditions. Based on the thermal model produced by *Peacock et al.* [2002] for Cascadia, the predicted Moho temperatures should range from just over 500°C at 20km depth to 650°C at 60km (Figure 5.7). These P-T conditions coincide well with the dehydration conditions for antigorite, a major hydrous mineral constituent of serpentine [*Winter*, 2001, p. 600]. Thus, we interpret the intraslab events occurring beneath the Moho as slab mantle earthquakes associated with the serpentine dehydration reaction. It is also suggestive, as would be expected for a thermally controlled process like serpentine dehydration, that the migration of the mantle events toward the Moho, as discussed in Section 3.5, parallel the calculated isotherms for the slab (Figure 5.8).

Given our above interpretation, how well do the velocities fit in? One of the main reasons for

the interpretation of the reflector as the Moho relied upon the velocities in the vicinity of the reflector surface. Regarding the up-dip portion of the slab in Figure 5.6, the velocities above the reflector, which would correspond to the subducting crust assumed 7km thick, range from the lower 6km/s to lower 7km/s range, approximating well the expected P-velocities for hydrated basaltic oceanic crust. Beyond 40km depth, where crustal intraslab earthquakes begin occurring, the oceanic crustal velocities increase to low to mid 7km/s throughout, which is expected once portions of the crust begin converting to eclogite as evidenced by the earthquakes. Velocities below the reflector are roughly consistent with dehydrating uppermost mantle rocks, being greater than 7km/s throughout the cross section and near 8km/s in the most down-dip, and thus most anhydrous, portions.

The lack of a low velocity zone within our section, in contrast to the previously discussed subduction zones (Section 5.5), may derive from several causes. Due to the resolution tests of Section 4.3, we are certain that none exists. The most obvious explanation is that very little to none of our resolved portion of the slab underlies high velocity mantle material. Peridotite mantle rocks have velocities at about 8km/s. Thus, if untransformed basaltic oceanic crust, with velocities closer to 7km/s were surrounded by peridotite mantle, the subducting oceanic crust would appear as a low-velocity zone. Nowhere in the resolved portion of our model do we see velocities above the slab at 8km/s. Indeed, the majority of our resolved slab model underlies the very low velocity rocks of the Olympic core. A low-velocity zone exists ~10km above the reflector to the east of the Olympics where the wet metamorphic rocks may be underplating the Crescent basalts (Figure 5.6). Only at depths greater than about 30 or 40km in the eastern portion of the model would we expect to see North American mantle. However, in this region, where reasonably resolved, we see velocities in the low to mid 7km/s range above the slab. This low-velocity "mantle wedge" could be interpreted as accreted, partially subducted wet metamorphic rocks, or as a serpentinized (hydrated) mantle wedge. We prefer the hydrous mantle wedge interpretation due to several recent papers on serpentinization of the mantle wedge in Cascadia [*Bostock et al.*, 2002; *Brocher et al.*, 2003; *Blakely et al.*, 2002] and Japan [*Kamiya and Kobayashi*, 2000].

5.7 Discussion

To summarize, we interpret the imaged wide-angle reflector as the Moho of the subducting oceanic lithosphere with the up-dip intraslab earthquakes occurring within the uppermost subducted mantle associated with serpentine dehydration and, beginning at 40km depth, the onset of oceanic crustal events associated with the dehydration of basalt to eclogite. However, neither our results nor dehydration metamorphic petrology precludes the possibility of individual earthquakes occurring either in the subducted oceanic crust up-dip of 40km or of mantle earthquakes in the more down-dip regions [*Winter*, 2001].

Many possible dehydration reactions occur both within the basaltic composition oceanic crust [*Hacker*, 1996; *Peacock et al.*, 2002], although much smaller in magnitude in terms of water release than for eclogite, and within the peridotite composition mantle rocks [*Winter*, 2001, p. 600]. The dehydration reactions prior to eclogitization typically release only $\sim 0.1\%$ H_2O, whereas well over 1% water is released during eclogitization [*Hacker*, 1996; *Hacker et al.*, 2002]. The only crustal dehydration reaction that releases a comparable volume of water is conversion to amphibolite. However, only the very warmest subduction zones are expected to have geotherms that intersect the P-T stability field for amphibolite and, those that do, apparently undergo the reverse reaction, i.e. decrease of free water, and transform at very shallow depths [*Peacock et al.*, 2002]. Mantle dehydration reactions, on the other hand, indicate the possibility for nearly continuous dehydration to depths much greater than 60km depending on the thermal conditions [p. 600 *Winter*, 2001; *Meade and Jeanloz*, 1991].

Dehydration embrittlement requires deviatoric stresses to occur. Simple lithostatic pressure will eventually cause dehydration under appropriate P-T conditions but may not lead to brittle failure. Shear stresses are necessary to produce "seismic" sources just as they are for typical shallow events. One of the more interesting phenomena associated with the basalt to eclogite transformation is that it produces its own stress field in response to the 15% volume reduction involved in the conversion (see Section 5.2.2 and Figure 5.4). In addition,

the densification of the oceanic crust after eclogitization has been hypothesized to cause increased dip to the slab due to increased negative buoyancy relative to the surrounding mantle [*Hacker*, 1996]. This increase in dip creates additional bending stresses within the slab. Thus, the basalt to eclogite transformation itself can provide additional stresses that could induce further seismicity. Bending stresses and volume accommodation stresses caused by the basalt to eclogite transformation also contribute to deviatoric stresses in the mantle allowing earthquakes associated with serpentine dehydration embrittlement, which does not produce a significant self-induced stress field, to occur within the mantle.

5.7.1   Distribution of Intraslab Seismicity

Our model reasonably explains the occurrence of both intraslab mantle and crustal events in a general sense. However, how can we explain the high seismicity rates observed under the Olympic Peninsula and the marked lack of intraslab seismicity within Oregon?

Olympic Peninsula

Intraslab seismicity rates are relatively high under the Olympic Peninsula and NW Washington compared to rates both to the north in British Columbia and south into Oregon (Figure 1.3). This region of high seismicity rates occurs near a concave seaward bend in the deformation front of the subducting Juan de Fuca plate. The bend in the subduction zone creates a space problem with the subducting lithosphere. Just as pleats in a tablecloth must appear at the corners of a table due to excess material there, the subducting lithosphere must accommodate the excess material cause by the bend in the subduction zone. The geometrical and strain implications of this are addressed by *Chiao and Creager* [2002] using a membrane strain approximation. They impose slab geometry boundary conditions along the deformation front and along two cross sections under Oregon and Vancouver Island and solve for the membrane geometry and slab particle paths within that geometry that minimizes the total dissipation power assuming a viscous rheology. They found that
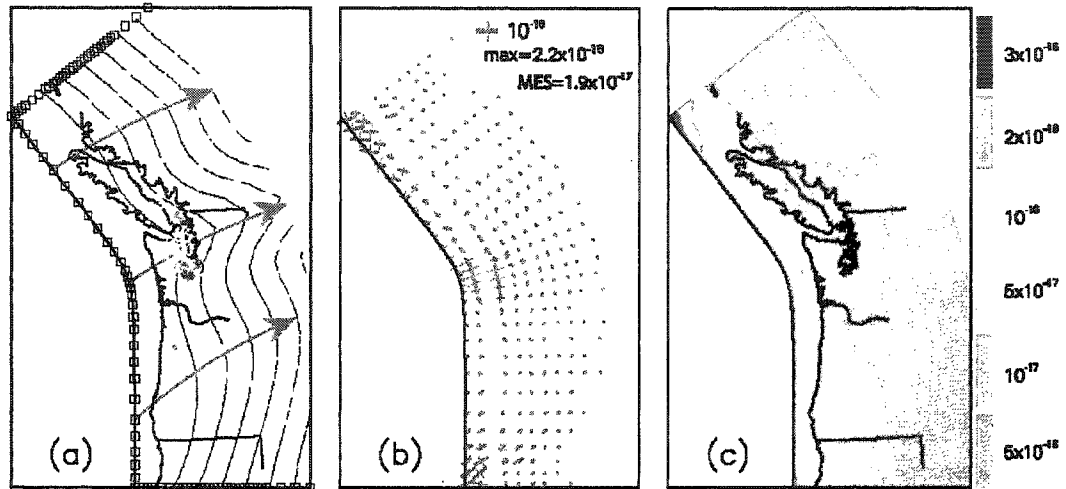
Figure 5.9: a) Depth contours (30km intervals) showing computed slab geometry that minimizes the deformation rate, intraslab events, and three inferred particle paths. b) Principle axes of calculated membrane strain rates (bold red bars show compression and thin blue lines show extension). c) Calculated membrane strain rates for Cascadia (see text). Color bar at right indicates strain rate (s^{-1}). Modified from *Chiao and Creager* [2002].

geometrically the slab would develop a "pleat", or up-warp, under the Olympic Peninsula with very shallow dip and the highest strain rates in their model confined to this region (Figure 5.9). Geometrically, their results accord with our results and with previous work (see Section 1.3). The high strain rates under the Olympic Peninsula predicted by their model also help explain the high seismicity rates there.

Oregon

Intraslab seismicity rates in Oregon are excessively low. South of the lineament of seismicity which contains the Nisqually event (see Section 1.3), intraslab seismicity rates drop off dramatically relative to the high rates under the Olympics, but intraslab events are not uncommon under SW Washington. However, south of Portland, only a handful of intraslab events have occurred. From an hazards perspective, an important question is whether our

observations to the present represent the status quo or should we expect a large event in the future to fill the gap?

Based on our model of dehydration embrittlement, we suggest several possible causes of this seismic quiescence. One of the most obvious is that the subducting lithosphere could be less hydrated under Oregon than elsewhere. Although it is difficult to imagine significant variations in the water concentrations of the volcanics where hydrothermal circulation and cracking would be most pervasive, it is possible that the lower layers, including the gabbro and upper mantle, could remain fairly hydrothermally unaltered and thus remain nearly anhydrous. The lack of serpentine in unaltered upper mantle would preclude mantle earthquakes and the upward percolation of fluids that would be liberated during mantle dehydration into the overlying oceanic crustal layers would be absent. In experiments performed on basalts, *Hacker* [1996] found that dry basalt was severely kinetically hindered in transformation to eclogite, i.e. it did not transform at laboratory time scales even under strong overstepping conditions, whereas basalt wetted at 1% weight H_2O transformed readily. Thus, the possible lack of upward percolating water from the mantle could inhibit transformation of basalt to eclogite until depths where temperatures make the rocks too weak to support significant earthquakes. There is good evidence, however, from central Oregon that the mantle wedge is partially serpentenized [*Bostock et al.*, 2002; *Brocher et al.*, 2003], which indicates that dehydration has occurred there at least in the past if not at present.

Due to the nearly iso-thermal serpentine dehydration curve (Figure 5.2), slight changes in the thermal structure in the Oregon portion of Cascadia could greatly reduce or eliminate mantle earthquakes there. A slight rise in temperature in Oregon could push the serpentine dehydration line to intersect the subducted Moho at much shallower depths than under the Olympic Peninsula and moderate increases in temperature could preclude the initial formation of significant quantities of serpentine (Figure 5.7). However, warming of the lithosphere would not greatly affect the basalt to eclogite reaction within the subducting crust.

Another interesting possibility is based on observations made by *Raleigh and Paterson* [1965] during their experiments on serpentine. If the fluids escape during dehydration, instead of being confined to the sample under pressure, serpentine remained ductile even under dehydration conditions. They attributed this to the inability to build up pore pressures. According to this hypothesis, if the fluids migrate rapidly from the dehydrating regions, the basalt or serpentine would deform plastically in response to stresses rather than undergoing brittle failure and, therefore, earthquakes would not occur. However, due to the high lithostatic pressures present where dehydration would be occurring, it seems improbable that fluid migration rates would be sufficiently high to activate this mechanism.

Finally, another obvious cause for the lack of seismicity within Oregon is that there may be less stress within the slab there. *VanDecar* [1991] and *VanDecar et al.* [1993] suggested, based on tomographic modeling of the deeper portions of Cascadia, that beneath approximately 100km depth the subducting slab has broken off. This would greatly reduce the slab pull stresses within the slab perhaps to the point that the stresses are insufficient to produce earthquakes. However, regardless of the mechanisms that are producing seismic quiescence in Oregon, we still expect basalt to eventually transform to eclogite and the resulting 15% volume reduction would still produce a stress field within the slab, assuming the transforming oceanic crust does not delaminate from the slab. Perhaps this self-induced stress field is insufficient on its own to induce deviatoric stresses capable of triggering earthquakes especially in a low pore pressure environment or may be delayed to sufficiently high P-T conditions that plasticity is the primary means of deformation.

British Columbia

The intraslab events under British Columbia separate into two bands (Figure 1.5). The western band consists of events which occur generally shallower than 40km depth [*Rogers et al.*, 1990], but whose locations are highly uncertain due to the fact they lie largely offshore. The eastern band is generally coincident with the Strait of Georgia and lies between 60km and 70km depth [*Cassidy and Waldhauser*, 2002]. These two bands merge into one under

the Olympic Peninsula. According to our hypothesis, the western band of seismicity would be related to serpentine dehydration and, therefore, should be confined to the subducted mantle. Conversely, the eastern band would be related to the basalt to eclogite reaction within the subducted crust. Unlike under the Olympics, where the slab is at a shallow dip, the slab under British Columbia is more steeply dipping [*Trehu et al.*, 2002], which would cause the slab there to be colder at a given depth than in NW Washington. The colder slab could kinetically hinder the basalt to eclogite reaction to occur at a much greater depth than the equilibrium conditions would predict [*Hacker*, 1996].

Corroborating our conjecture for the eastern band, *Cassidy and Waldhauser* [2002], using double-difference earthquake relocation, and *Cassidy and Ellis* [1993], using receiver functions, concluded that the intraslab seismicity under the Strait of Georgia primarily occurred within the subducted oceanic crust. Interestingly, in SW Washington, *Parsons et al.* [1998] interpreted the bulk of catalog intraslab earthquakes, which generally are confined to depths shallower than 40km, as occurring within the subducted mantle. Our interpretation reconciles these two apparently contradictory conclusions: the up-dip (western) intraslab events occur within the subducted mantle, while the down-dip events occur primarily within the crust.

Seismic Lineament

A seismic lineament aligned approximately parallel to the relative plate motion direction bounds the high seismicity rate region of the Olympic Peninsula to the south and contains both the largest magnitude and deepest intraslab events in Cascadia (see Section 1.3). *Kirby et al.* [1996] explained similar lineaments observed in the Nazca subduction zone in South America as resulting from subducted seamounts or volcanic chains inferred from extrapolated paths of existing chains. Presumably, these regions of the oceanic crust are more hydrated and/or thicker than normal oceanic crust due to volcanism and, thus, require longer times to dehydrate or warm to dehydration temperatures [*Kirby et al.*, 1996]. The Juan de Fuca plate, however, has very few seamounts and the mirror side (Pacific) of the
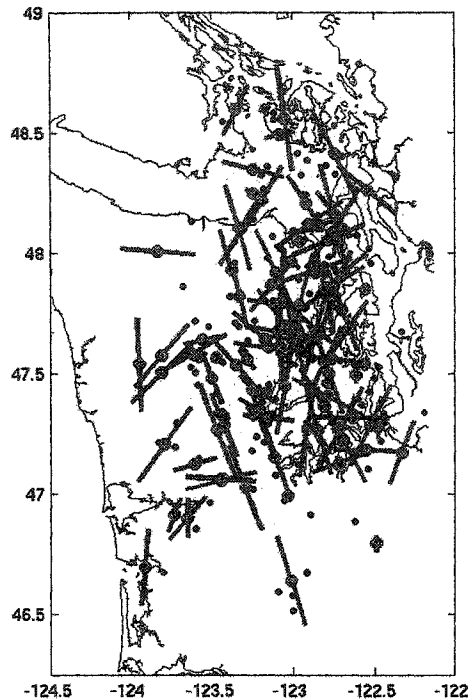
Figure 5.10: Intraslab earthquake T-axes projected onto the reflector surface. Intraslab events with no focal mechanisms are shown as black dots.

ridge does not reveal a volcanic chain in a position corresponding to the observed seismic lineament.

Within this seismic lineament, the largest events appear at the base of the microseismicity (see Section 1.3 and Figure 1.4). Double difference relocations of a small group of intraslab events in SW British Columbia [*Cassidy and Waldhauser*, 2002] show the same pattern. They interpreted the deepest events, which contain the three largest events, as occurring within the subducting mantle and the smaller events as occurring in the subducting crust. *Wang* [2002], based on modeling of stresses within the subducting lithosphere from slab bending, unbending and dehydration, argued that the oceanic crust is much weaker than the subducting mantle and thus cannot support large events whereas the more structurally intact mantle would be able to accumulate larger stresses, and thus contain larger earthquakes.
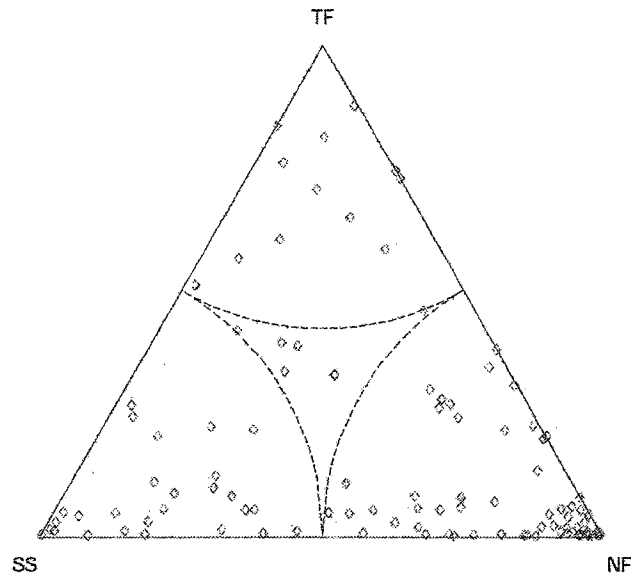
Figure 5.11: Triangle plot of slab geometry corrected focal mechanisms based on P and T axes orientations relative to the slab. SS: strike-slip; TF: thrust faulting; NF: normal faulting. Focal mechanisms that fall in the center of the triangle are ambiguous in type.

5.7.2 Focal Mechanisms

A detailed study of focal mechanisms for intraslab earthquakes in Cascadia has not been completed, although the studies by *Ma et al.* [1996] and *Ludwin et al.* [1991] are important first steps, and is certainly one of the areas where future work could concentrate. The PNSN routinely determines first motion focal mechanisms for any event with sufficient data coverage to calculate a reliable mechanism. Approximately 100 of the intraslab events we included in our inversion had catalog focal mechanisms. After rotating into the slab coordinate system, the distribution of T-axes in map view appear chaotic but clearly indicate in-plane tension (Figure 5.10), confirming the results of *Ma et al.* [1996]. To identify if any preference for event type (normal, strike slip, or reverse) exists, we plot the focal mechanisms using a scheme similar to *Igarashi et al.* [2001]. The three "pure" event types form the points of the triangle in Figure 5.11. The bottom edge, represents all focal mechanisms with T-axes parallel to the reflector surface. At the top of the triangle, which represents pure thrust motion, the T-axes are normal to the reflector surface. Points within the triangle, represent
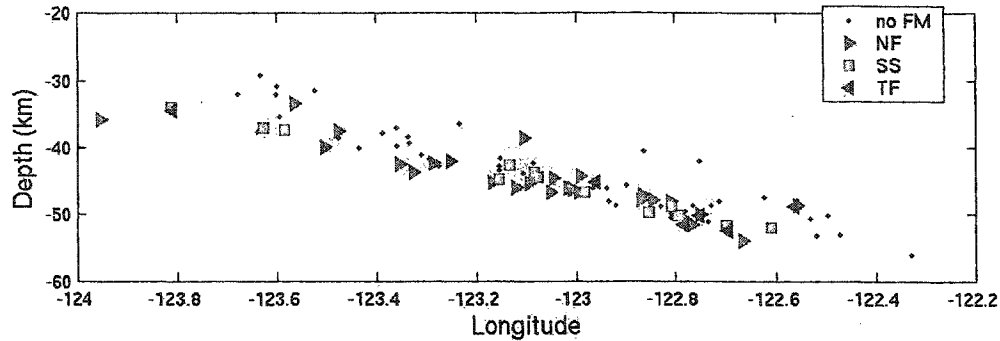
Figure 5.12: Cross-section of intraslab earthquakes and associated focal mechanism type. noFM: no focal mechanism available; SS: strike-slip; TF: thrust faulting; NF: normal faulting.

intermediate T-axis dip angles. P-axes dip angles vary from $0°$ on the left edge to $90°$ at "NF." In this way, we find nearly 60% of the events are normal faulting events and about 25% are strike slip (Figure 5.11). No clear spatial correlation of event type to location in map view or north-south cross section is evident. However, in east-west cross section, a subtle pattern is apparent (Figure 5.12). The strike-slip events appear to be confined to a narrower zone than the other types of events. This is especially clear in histograms of event depth relative to the reflector divided among the three event types (Figure 5.13). The strike-slip events cluster primarily within 2–3 km of the reflector with the exception of a few updip events that appear deeper where the reflector position is less well constrained. The reason for this clustering of strike slip events is unclear, although the predominance of strike slip and normal faulting intraslab events has also been noted in SW Japan [Shiono, 1987].

5.7.3 Hazard Implications

From a hazards perspective, the occurrence of earthquakes within the subducting mantle may pose increased risks. If the only operating nucleation process for intraslab earthquakes was related to the basalt to eclogite transformation, the earthquakes would primarily be confined to the subducting crust. Under these circumstances, the maximum magnitude
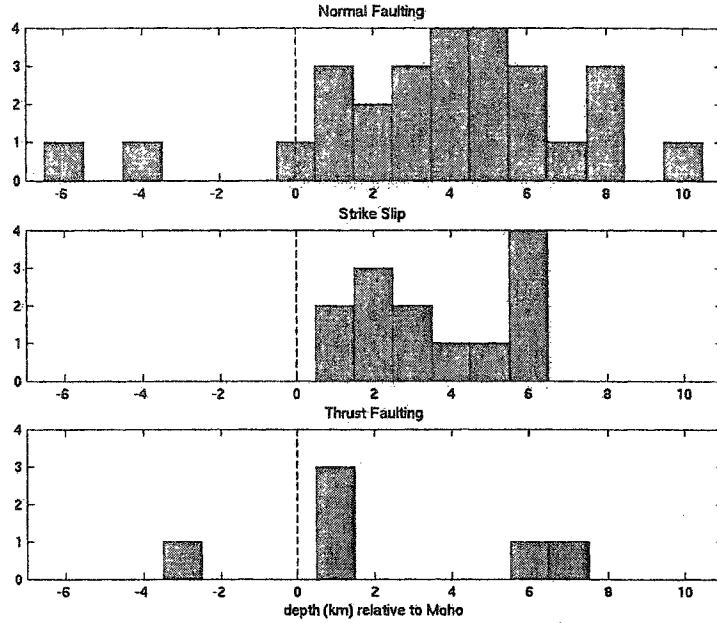
Figure 5.13: Intraslab earthquake focal mechanism type distribution relative to the reflector. Distances are relative to the reflector with negative distances being above the reflector.

event that could be expected would be limited geometrically by what size event could fit within the crust. Using standard aspect ratios, if we assume the width of the fault is about twice the crustal thickness, i.e. the fault dips at $\sim 30°$, the length of the fault is about twice its width, and a slip of 1.5m, giving $w = 15$km, $l = 30$km, and $d = 1.5$m. Since $M_0 = \mu lwd = 2e^{19}$N-m, we estimate $M_w = 2\log(M_0)/3 - 6.06 = 6.8$ as the largest magnitude earthquake that could fit entirely within the subducting crust. However, if earthquakes can rupture through the mantle lithosphere then the maximum possible magnitude may be much larger.

A secondary hazard implication derives from the high-amplitude energy observed in the wide-angle reflection data. Beyond the critical angle, the reflections from the subducting Moho are often much larger in amplitude than the direct arrivals themselves. Thus, including slab wide-angle reflections in ground motion models may be an important element in determining maximum accelerations of regional earthquakes, most notably, a megathrust event. The source for a megathrust event would be ideally situated to utilize the strong

amplification effect of the wide-angle reflections, especially from waves that reflect from the earth's free surface such as PP or SS.

5.7.4   Consequences

Recent observations from SW British Columbia and Western Washington GPS stations reveal the presence of episodic slow slip events, with a repeat time of about 14 months, that apparently coincide with the plate interface [*Dragert et al.*, 2001; *Miller et al.*, 2002]. These events produce about 2cm of thrust-type slip extending down from the the down-dip edge of the megathrust zone and propagate a few hundred km along strike from the Olympic Mountains into southern or central Vancouver Island over a few week period. Moreover, recently discovered deep tremor events, which are non-impulsive sources detected at 2 to 6Hz, are coincident in space and time with the slow slip events in Cascadia [*Rogers and Dragert*, 2003]. First discovered in SW Japan, *Obara* [2002] interpreted these events as likely caused by some form of fluid driven process. The collocation of these deep-creep events within the region interpreted in our model to be undergoing transformation of basalt to eclogite suggests that these events are controlled by fluids released by this transformation.

In addition, fluids released from the subducting plate would be expected to infiltrate the overlying continental mantle, producing a serpentinized mantle wedge. Indeed, evidence from several geophysical source strongly suggest the presence of such a mantle wedge in Cascadia [*Bostock et al.*, 2002; *Brocher et al.*, 2003]. The lack of a well-defined continental Moho reflector west of the Cascades and the presence of low wave speeds ($\sim$7km/s) at 35–45km depth in our model are also consistent with high concentrations of serpentinite within the mantle wedge.

Chapter 6

Conclusion

6.1 Summary

We have presented results from an inversion of direct and reflection travel-time data for 3-D P-wave velocity structure, local earthquake hypocenters, and subducting Juan de Fuca Moho reflector geometry in NW Washington. In summary, the major points are:

6.1.1 Data

- 91,000 first-arrival travel times from four active-source experiments. These consist of the 1991 Western Cascades, 1995 SW Washington, 1998 Wet SHIPS, and 1999 Dry SHIPS experiments. The 1998 Wet SHIPS experiment, contributing the vast majority of the data used in the inversion, consisted of nearly 30,000 air-gun sources detonated within the inland waterways of NW Washington and SW British Columbia to over 200 land-based stations.

- 27,000 first-arrival times from over 1400 high-quality local earthquakes, repicked from the Pacific Northwest Seismograph Network catalog.

- nearly 1200 wide-angle reflection times consistent in time and slowness with expected reflections from the subducting Juan de Fuca plate.

6.1.2 Method

- Model parameters are 3-D P-wave slowness structure, earthquake hypocenter locations (in space and time), and reflector geometry. The model covers the region between 46.25°and 49°N, 121°and 125°W, and between −8km and 78km depth.

- We regularize the problem by minimizing the secondary order spatial derivatives of the slowness structure and reflector surface. We also impose a very weak constraint to stabilize the earthquake problem by asking the relocations be small between iterations.

- Reflection bounce points are determined by finding the point corresponding to the minimum reflection travel time on the reflector surface.

- The reflector surface is relocated according the local vertical reflection travel time gradient at the bounce point locations.

- Reflected rays are allowed to adjust the slowness structure in the same way first-arrival rays do.

- This is an iterative non-linear inversion procedure, which stably converges after several iterations.

6.1.3 Results

- RMS travel-time residuals in the final model are 0.09s, 0.12s, and 0.08s for the active-source, earthquake, and reflection data respectively, amounting to 98.7% and 91.0% variance reductions for the active-source and earthquake data.

- The fact that reflections are only observed at wide-angle, which is indicative of an increase in velocity with depth across the reflector, and that model results indicate a strong velocity gradient in the vicinity of the reflector leading to ∼8km/s velocities just below the reflector, lead us to the interpretation that the reflector is the Moho of the subducting Juan de Fuca plate.

- Relocated intraslab seismicity separate into two groups based on the reflector depth contour. Those up-dip of the 45km depth contour occur below the reflector within the subducting oceanic mantle. Those down-dip of this contour generally lie above the reflector, within the subducting oceanic crust.

- These results are consistent with serpentine dehydration reactions within the mantle and the basalt to eclogite reaction within the crust being the causes of the intraslab seismicity. The concurrence of the onset of oceanic crustal events and of the predicted onset of the basalt to eclogite reaction at about 40km depth, corroborates these interpretations.

6.1.4   Error Analysis

- Our results require precise knowledge of the interrelations among the velocities, intraslab earthquake locations, and the reflector.

- Standard velocity checkerboard tests reveal we have the necessary resolvability, returning strong pattern matching and adequate amplitude throughout the regions of interest. Resolution is especially good in the shallow structure where we have active-source and shallow North American crustal earthquakes and within the slab where we have intraslab seismicity.

- To investigate our ability to resolve velocities in the vicinity of the reflector, we added an 8km thick -1km/s perturbation to the model parallel to and above the reflector. We can resolve velocities well, returning close to 75% amplitude and showing little smearing in regions containing intraslab events.

- A similar test for velocities below the reflector reveal little smearing and near 90% amplitude return there.

- We perform intraslab earthquake and reflector parameter tests to investigate the relative error between the two. In these tests, we fix the reflector or intraslab earthquake depths at $-5, -2, +2$ or $+5$km relative to the final model, re-invert, and compare vari-

ances. Results indicate that we can resolve the average depth of the intraslab events relative to the reflector to within about ±2km.

6.1.5 Discussion

- Pore pressure caused by volatiles released during metamorphic dehydration reactions allows fault slip according to the dehydration embrittlement hypothesis. Thus, both fluids and deviatoric stresses within the slab are necessary for intraslab earthquake nucleation.

- Although observations in other subduction zones present evidence that many of the intraslab earthquakes are occurring within the subducting crust associated with the basalt to eclogite transformation reaction, this explanation does not explain all of the intraslab seismicity. According to our results, seismicity occurring shallower than the onset of the basalt to eclogite reaction may be related to mantle dehydration reactions.

- Our results suggest that the lack of intraslab seismicity within Oregon must be related either to a shortage of water or weaker stresses in the subducting lithosphere. It is unlikely that the oceanic crust escapes being at least somewhat hydrated and, thus, it must dehydrate at some point during subduction, but perhaps it does so aseismically.

- The high intraslab seismicity rates observed under the Olympic Peninsula agree well with the predicted area of high strain rates associated with membrane strains caused by the concave oceanward trench curvature [*Chiao and Creager*, 2002].

- We suggest the shallow western band of intraslab seismicity observed off SW British Columbia corresponds to mantle deserpentinization reactions, while those events in the deeper, eastern band generally occur within the subducting crust due to eclogitization.

- The lineament of seismicity containing the largest and deepest events in Cascadia is similar in pattern to other lineaments observed in other subduction zones, which have been interpreted as regions of higher subducted slab hydration [*Kirby et al.*, 1996].

- Catalog focal mechanisms, when oriented into the slab coordinate system, reveal a preponderance of normal-faulting and strike-slip events, i.e. in-plane tension. Slab pull and bending stresses can roughly explain the tension.

- If intraslab earthquakes were completely contained within the subducting crust, the maximum magnitude one would expect would be limited geometrically by what would geometrically fit in the crust to about M7. However, since our results indicate the presence of mantle earthquakes, there is the geometric possibility that a much larger event could occur.

- Observationally, the wide-angle reflections often had much larger amplitudes than those of direct arrivals. From a hazards perspective, a megathrust earthquake could produce waves ideally situated to take advantage of this amplification effect [*Shragge et al.*, 2002], meaning that more damage could be caused from these slab reflected waves than from the direct waves.

- Recent observations of episodic slow-slip [*Dragert et al.*, 2001; *Miller et al.*, 2002] and tremor [*Rogers and Dragert*, 2003] events appear to coincide spatially with an area in our model we interpret as undergoing transformation of basalt to eclogite, consistent with these events being caused by some form of fluid process.

- The presence of a serpentinized mantle wedge in Cascadia, as would be expected as fluids released from the dehydrating oceanic slab infiltrate the overlying mantle, is strongly suggested from several geophysical sources [*Brocher et al.*, 2003] and is supported by low velocities in our model between 35km and 45km depth.

6.2 Future Directions

Although there are many possible and fruitful directions that could be taken, one of the most nagging unanswered questions concerns the structure of the seismic lineament, which contains the largest events such as the Nisqually earthquake, and the lack of intraslab seismicity in Oregon. Why are the large events concentrated in this lineament? Should

we prepare for large intraslab events in Oregon or is the present quiescence status quo? The tools developed during this research, if applied to these areas, could provide valuable information concerning the subducting slab structure. Besides providing slab geometry and location relative to the intraslab events, changes in waveform characteristics or reflectivity among regions could provide insight into changes in the roughness of the slab or possibly pinpoint areas with high fluid content. For example, as one crosses the seismic lineament, do the reflections cease, become more incoherent, increase in amplitude, etc? By incorporating velocity structure, can we say the subducted crust is thicker in this zone? We can ask similar questions concerning the subducted crustal structure in Oregon. Unfortunately, the lack of intraslab seismicity in Oregon itself hampers research due to the lack of deep velocity constraint. An (or multiple) experiment(s) similar to Wet SHIPS along the coast stretching from just south of the Olympics into Oregon would at least provide detailed upper continental crustal structure and information on the variations in the reflectivity of the subducting lithosphere. The hopefully upcoming CASSIS experiment in SW British Columbia offers the possibility of extending our map of NW Washington into this area as well.

In addition, precise double-difference intraslab earthquake relocations such as performed in Canada by *Cassidy and Waldhauser* [2002] and on the Nisqually earthquake and its aftershocks by *Creager and Xu* [2002] could provide better insight into the relationship between larger events and the microseismicity. Better and more focal mechanism solutions such as done by *Igarashi et al.* [2001] on small events in NE Japan hold the promise of clearly defining the spatial interrelationship among the different source types, allowing us to have a firmer understanding of the stress state within the slab. Inclusion of slab reflected waves from earthquakes, although allowing less resolvability, does permit a mapping of the slab geometry outside the expense of active-source experimentation (presently unpublished work by Guy Medema). A very serious shortcoming in the PNSN catalog data presently is the low number of S-wave picks. As more S-wave data becomes available from 3-component stations, tomography and earthquake relocations incorporating S travel times would prove invaluable for interpreting structure and its relation to the hypocenters by providing increased accuracy

in hypocentral locations and by providing information on Poisson ratios that can help discriminate rock types. Inclusion of reflection data in such an inversion would greatly enhance our view of the structure of the subducting lithosphere.

Bibliography

Abers, G. A., Relationship between shallow- and intermediate-depth seismicity in the eastern Aleutian subduction zone, *Geophys. Res. Lett.*, *19*, 2019–2022, 1992.

Aki, K., and P. G. Richards, *Quantitative Seismology: Theory and Methods*, vol. 1, W.H. Freeman, 1980.

Alt, J. C., and D. A. Teagle, Hydrothermal alteration and fluid fluxes in ophiolites and oceanic crust, in *Ophiolites and Oceanic Crust: New Insights from Field Studies and the Ocean Drilling Program*, edited by Y. Dilek, E. Moores, D. Elthon, and A. Nicolas, no. 349 in Geological Society of America Special Paper, pp. 273–282, 2000.

Atwater, B. F., and H. E. Hemphill, Recurrence intervals for great earthquakes in coastal Washington, *Geol. Soc. Am.*, *29*, 131, 1997.

Blakely, R., T. Brocher, and R. Wells, Cascadia gravity and magnetic anomalies delineate hydrated forearc mantle, *EOS, Trans. Am. Geophys. Un.*, *83*, Fall Meet. Suppl., Abstract S21C-04, 2002.

Bostock, M. G., R. D. Hyndman, S. Rondenay, and S. M. Peacock, An inverted continental Moho and serpentinization of the forearc mantle, *Nature*, *417*, 536–538, 2002.

Brandon, M. T., and A. R. Calderwood, High-pressure metamorphism and uplift of the Olympic subduction complex, *Geology*, *18*, 1252–1255, 1990.

Brocher, T., T. Pratt, K. Miller, A. Trehu, C. Snelson, C. Weaver, K. Creager, R. Crosson, U. ten Brink, M. Alverez, S. Harder, and I. Asudeh, *Report for Explosion and Earthquake Data Acquired in the 1999 Seismic Hazards Investigation in Puget Sound (SHIPS), Washington*, U.S. Geological Survey Open-File Report 00-318, 2000.

Brocher, T., T. Parsons, R. Blakely, N. Christensen, M. Fisher, R. Wells, U. ten Brink, T. Pratt, R. Crosson, K. Creager, N. Symons, L. Preston, T. van Wagoner, K. Miller, C. Snelson, A. Trehu, V. Langenheim, G. Spence, K.Ramachandran, R. Hyndman, D. Mosher, B. Zelt, and C. Weaver, Upper crustal structure in Puget lowland, Washington: Results from the 1998 seismic hazards investigation in Puget Sound, *J. Geophys. Res.*, *106*, 13,541–13,564, 2001.

Brocher, T. M., T. Parsons, K. C. Creager, R. S. Crosson, N. P. Symons, G. Spence, B. C. Zelt, P. T. C. Hammer, R. D. Hyndman, D. C. Mosher, A. M. Trehu, K. C. Miller, U. S. ten Brink, M. A. Fisher, T. L. Pratt, M. G. Alvarez, B. C. Beaudoin, and C. S. Weaver, *Wide-Angle Seismic Recordings from the 1998 Seismic Hazards Investigation in Puget Sound (SHIPS), Western Washington and British Columbia*, U.S. Geological Survey Open-File Report 99-314, 1999.

Brocher, T. M., T. Parsons, A. M. Trehu, C. M. Snelson, and M. A. Fisher, Seismic evidence for widespread serpentinized forearc upper mantle along the Cascadia margin, *Geology*, *31*, 267–270, 2003.

Cassidy, J. F., and R. M. Ellis, S wave velocity structure of the northern Cascadia subduction zone, *J. Geophys. Res.*, *98*, 4407–4421, 1993.

Cassidy, J. F., and F. Waldhauser, Precise relocations of slab seismicity in the northern Cascadia subduction zone, in *The Cascadia Subduction Zone and Related Subduction Systems - Seismic Structure, Intraslab Earthquakes and Processes, and Earthquake Hazards*, edited by S. Kirby, K. Wang, and S. Dunlop, U.S. Geological Survey Open-File Report 02-328 and Geological Survey of Canada Open File 4350, pp. 69–73, 2002.

Chiao, L.-Y., and K. C. Creager, Geometry and membrane deformation rate of the subducting Cascadia slab, in *The Cascadia Subduction Zone and Related Subduction Systems - Seismic Structure, Intraslab Earthquakes and Processes, and Earthquake Hazards*, edited by S. Kirby, K. Wang, and S. Dunlop, U.S. Geological Survey Open-File Report 02-328 and Geological Survey of Canada Open File 4350, pp. 47–54, 2002.

Choy, G. L., and J. L. Boatwright, Global patterns of radiated seismic energy and apparent stress, *J. Geophys. Res.*, *100*, 18,205–18,228, 1995.

Choy, G. L., J. L. Boatwright, and S. Kirby, *The Radiated Seismic Energy and Apparent Stress of Interplate and Intraslab Earthquakes at Subduction Zone Environments: Implications for Seismic Hazard Estimation*, U.S. Geological Survey Open File Report 01-0005, 2001.

Coleman, R. G., *Ophiolites*, vol. 12 of *Minerals and Rocks*, Springer-Verlag, 1977.

Creager, K. C., and Q. Xu, The 2001 M_w 6.8 Nisqually earthquake and its aftershocks, *EOS, Trans. Am. Geophys. Un.*, *83*, Fall Meeting Suppl., Abstract S21C–10, 2002.

Crosson, R., Crustal structure modeling of earthquake data 2. Velocity structure of the Puget Sound region, Washington, *J. Geophys. Res.*, *81*, 3047–3054, 1976.

Crosson, R. S., and T. Owens, Slab geometry of the Cascadia subduction zone beneath Washington from earthquake hypocenters and teleseismic converted waves, *Geophys. Res. Lett.*, *14*, 824–827, 1987.

Dragert, H., R. D. Hyndman, G. C. Rogers, and K. Wang, Current deformation and the width of the seismogenic zone of the northern Cascadia subduction thrust, *J. Geophys. Res.*, *99*, 653–668, 1994.

Dragert, H., K. Wang, and T. S. James, A silent slip event on the deeper Cascadia subduction interface, *Science*, *292*, 1525–1528, 2001.

Efron, B., and R. J. Tibshirani, *An Introduction to the Bootstrap*, vol. 57 of *Monographs on Statistics and Applied Probability*, chap. The Jackknife, Chapman and Hall, 1993.

Frohlich, C., The nature of deep-focus earthquakes, *Ann. Rev. Earth Planet. Sci.*, *17*, 227–254, 1989.

Fukao, Y., S. Hori, and M. Ukawa, A seismological constraint on the depth of basalt-eclogite transition in a subducting oceanic crust, *Nature*, *303*, 413–415, 1983.

Green, H., II, and P. Burnley, A new self-organizing mechanism for deep-focus earthquakes, *Nature*, *341*, 733–737, 1989.

Hacker, B. R., Eclogite formation and the rheology, buoyancy, seismicity, and H_2O content of oceanic crust, in *Subduction: Top to Bottom*, edited by G. Bebout, D. Scholl, S. Kirby, and J. Platt, Geophysical Monograph 96, pp. 337–346, American Geophysical Union, 1996.

Hacker, B. R., G. A. Abers, and S. M. Peacock, Theoretical mineralogy, density, seismic wavespeeds and H_2O content of the Cascadia subduction zone, with implications for intermediate-depth seismicity and earthquake hazard, in *The Cascadia Subduction Zone and Related Subduction Systems - Seismic Structure, Intraslab Earthquakes and Processes, and Earthquake Hazards*, edited by S. Kirby, K. Wang, and S. Dunlop, U.S. Geological Survey Open-File Report 02-328 and Geological Survey of Canada Open File 4350, pp. 133–137, 2002.

Hacker, B. R., G. A. Abers, and S. M. Peacock, Subduction factory 1. Theoretical mineralogy, densities, seismic wave speeds, and H_2O contents, *J. Geophys. Res.*, *108*, 2029, doi:10.1029/2001JB001,127, 2003.

Hasegawa, A., N. Umino, and A. Takagi, Double-planed deep seismic zone and upper mantle structure in the northeastern Japan Arc, *Geophys. J. R. Astron. Soc.*, *54*, 281–296, 1978.

Helffrich, G., and G. A. Abers, Slab low-velocity layer in the eastern Aleutian subduction zone, *Geoph. J. Int.*, *130*, 640–648, 1997.

Hole, J., Nonlinear high-resolution three-dimensional seismic travel time tomography, *Geoph. J. Int.*, *97*, 6553–6562, 1992.

Hole, J., and B. Zelt, 3-D finite-difference reflection traveltimes, *Geoph. J. Int.*, *121*, 1995.

Houston, H., and H. Green, II, The mechanics of deep earthquakes, *Ann. Rev. Earth Planet. Sci.*, *23*, 169–213, 1995.

Igarashi, T., T. Matsuzawa, N. Umino, and A. Hasegawa, Spatial distribution of focal mechanisms for interplate and intraplate earthquakes associated with the subducting

Pacific plate beneath the northeastern Japan arc: A triple-planed deep seismic zone, *J. Geophys. Res.*, *106*, 2177–2191, 2001.

Kamiya, S. I., and Y. Kobayashi, Seismological evidence for the existence of serpentinized wedge mantle, *Geophys. Res. Lett.*, *27*, 819–822, 2000.

Kirby, S., Intraslab earthquakes and phase changes in subducting lithosphere, *Rev. Geophys. Suppl.*, *U.S. National Report to International Union of Geodesy and Geophysics 1991–1994*, 287–297, 1995.

Kirby, S., E. R. Engdahl, and R. Denlinger, Intermediate-depth intraslab earthquakes and arc volcanism as physical expressions of crustal and uppermost mantle metamorphism in subducting slabs, in *Subduction: Top to Bottom*, edited by G. Bebout, D. Scholl, S. Kirby, and J. Platt, Geophysical Monograph 96, pp. 195–214, American Geophysical Union, 1996.

Kirby, S., K. Wang, and S. Dunlop (Eds.), *The Cascadia Subduction Zone and Related Subduction Systems - Seismic Structure, Intraslab Earthquakes and Processes, and Earthquake Hazards*, U.S. Geological Survey Open-File Report 02-328 and Geological Survey of Canada Open File 4350, 2002.

Kirby, S. H., Localized polymorphic phase transformations in high-pressure faults and applications to the physical mechanism of deep earthquakes, *J. Geophys. Res.*, *92*, 13,789–13,800, 1987.

Kirby, S. H., Earthquake hazard appraisal in subduction zones: Intraslab earthquakes are undervalued as hazards relative to interplate thrust earthquakes, *EOS, Trans. Am. Geophys. Un.*, *80*, Fall Meet. Suppl., Abstract F651, 1999.

Kirby, S. H., W. B. Durham, and L. A. Stern, Mantle phase changes and deep-earthquake faulting in subducting lithosphere, *Science*, *252*, 216–225, 1991.

Lay, T., and T. C. Wallace, *Modern Global Seismology*, vol. 58 of *International Geophysics Series*, Academic Press, 1995.

Ludwin, R. S., C. S. Weaver, and R. S. Crosson, Seismicity of Washington and Oregon, in *Neotectonics of North America*, edited by D. B. Slemmons, E. R. Engdahl, M. D. Zoback, and D. D. Blackwell, vol. Decade Map Volume 1, pp. 77–97, Geological Society of America, 1991.

Ma, L., R. S. Crosson, and R. S. Ludwin, Western Washington earthquake focal mechanisms and their relationship to regional tectonic stress, in *Assessing Earthquake Hazards and Reducing Risk in the Pacific Northwest*, edited by A. M. Rogers, T. J. Walsh, W. J. Kockelman, and G. R. Priest, pp. 257–283, U. S. Geological Survey Professional Paper, 1996.

Matsuzawa, T., N. Umino, A. Hasegawa, and A. Takagi, Upper mantle velocity structure estimated from PS-converted waves beneath the north-eastern Japan Arc, *Geophys. J. R. Astron. Soc.*, *86*, 767–787, 1986.

Matsuzawa, T., T. Kono, A. Hasegawa, and A. Takagi, Subducting plate boundary beneath the northeastern Japan arc estimated from SP converted waves, *Tectonophysics*, *181*, 123–133, 1990.

Meade, C., and R. Jeanloz, Deep-focus earthquakes and recycling of water into the earth's mantle, *Science*, *252*, 68–72, 1991.

Miller, K. C., R. G. Keller, J. M. Gridley, J. H. Luetgert, W. D. Mooney, and H. Thybo, Crustal structure along the west flank of the Cascades, western Washington, *J. Geophys. Res.*, *102*, 17,857–17,873, 1997.

Miller, M. M., T. Melbourne, D. J. Johnson, and W. Q. Sumner, Periodic slow earthquakes from the Cascadia subduction zone, *Science*, *295*, 2423, 2002.

Mueller, R. D., P. W. Sloss, and National Geophysical Data Center, Age of the ocean floor, map, 1996.

Nedimovic, M., K. Ramachandran, and R. Hyndman, Deep structure of the Northern Cascadia subduction zone from reflections, tomography and seismicity studies, *EOS, Trans. Am. Geophys. Un.*, *83*, Fall Meeting Suppl., Abstract T51E–05, 2002.

Obara, K., Nonvolcanic deep tremor associated with subduction in southwest Japan, *Science*, *296*, 1679–1681, 2002.

Oda, H., T. Tanaka, and K. Seya, Subducting oceanic crust on the Philippine Sea plate in Southwest Japan, *Tectonophysics*, *172*, 175–189, 1990.

Paige, C., and M. Saunders, LSQR: An algorithm for sparse linear equations and sparse least squares, *ACM Trans. on Math. Soft.*, *8*, 43–71, 1982.

Parker, R. L., *Geophysical Inverse Theory*, Princeton University Press, 1994.

Parsons, T., A. M. Trehu, J. H. Luetgert, K. C. Miller, F. Kilbride, R. E. Wells, M. A. Fisher, E. R. Flueh, U. S. ten Brink, and N. I. Christensen, A new view into the Cascadia subduction zone and volcanic arc: Implications for earthquake hazards along the Washington margin, *Geology*, *26*, 199–202, 1998.

Peacock, S. M., Thermal and petrologic structure of subduction zones, in *Subduction: Top to Bottom*, edited by G. Bebout, D. Scholl, S. Kirby, and J. Platt, Geophysical Monograph 96, pp. 119–133, American Geophysical Union, 1996.

Peacock, S. M., Are the lower planes of double seismic zones caused by serpentine dehydration in subducting oceanic mantle?, *Geology*, *29*, 299–302, 2001.

Peacock, S. M., and R. D. Hyndman, Hydrous minerals in the mantle wedge and the maximum depth of subduction thrust earthquakes, *Geophys. Res. Lett.*, *26*, 2517–2520, 1999.

Peacock, S. M., and K. Wang, Seismic consequences of warm versus cool subduction metamorphism: Examples from southwest and northeast Japan, *Science*, *286*, 937–939, 1999.

Peacock, S. M., K. Wang, and A. M. McMahon, Thermal structure and metamorphism of subducting oceanic crust: Insight into Cascadia intraslab earthquakes, in *The Cascadia Subduction Zone and Related Subduction Systems - Seismic Structure, Intraslab Earthquakes and Processes, and Earthquake Hazards*, edited by S. Kirby, K. Wang, and S. Dunlop, U.S. Geological Survey Open-File Report 02-328 and Geological Survey of Canada Open File 4350, pp. 123–126, 2002.

Raleigh, C., and M. Paterson, Experimental deformation of serpentinite and its tectonic implications, *J. Geophys. Res.*, *70*, 3965–3985, 1965.

Ramachandran, K., Velocity of SW British Columbia and NW Washington from 3-D non-linear seismic tomography, Ph.D. thesis, University of Victoria, 2001.

Rogers, G., and H. Dragert, Episodic tremor and slip on the Cascadia subduction zone: The chatter of silent slip, *Science*, *300*, 1942–1943, 2003.

Rogers, G. C., and R. S. Crosson, Intraslab earthquakes beneath Georgia Strait/Puget Sound, in *The Cascadia Subduction Zone and Related Subduction Systems - Seismic Structure, Intraslab Earthquakes and Processes, and Earthquake Hazards*, edited by S. Kirby, K. Wang, and S. Dunlop, U.S. Geological Survey Open-File Report 02-328 and Geological Survey of Canada Open File 4350, pp. 65–67, 2002.

Rogers, G. C., C. Spindler, and R. D. Hyndman, Seismicity along the Vancouver Island LITHOPROBE corridor, in *Proceedings of the Project LITHOPROBE: Southern Canadian Cordillera Transect Workshop*, pp. 166–169, University of Calgary, Calgary, Alberta, 1990.

Satake, K., K. Shimazaki, Y. Tsuji, and K. Ueda, Time and size of a giant earthquake in Cascadia inferred from Japanese tsunami records of January 1700, *Nature*, *379*, 246–249, 1996.

Schimmel, M., and H. Paulssen, Noise reduction and detection of weak, coherent signals through phase-weighted stacks, *Geoph. J. Int.*, *130*, 497–505, 1997.

Seno, T., and Y. Yamanaka, Double seismic zones, compressional deep outer-rise events, and superplumes, in *Subduction: Top to Bottom*, edited by G. Bebout, D. Scholl, S. Kirby, and J. Platt, Geophysical Monograph 96, pp. 347–355, American Geophysical Union, 1996.

Seno, T., D. Zhao, Y. Kobayashi, and M. Nakamura, Dehydration of serpentinized slab mantle: Seismic evidence from southwest Japan, *Earth Plan. Space*, *53*, 861–871, 2001.

Shiono, K., Seismicity of the SW Japan arc — subduction of the young Shikoku Basin, *Mod. Geol.*, *12*, 449–464, 1987.

Shragge, J., M. Bostock, and G. C. Rogers, Modeling post-critical Moho reflections from intraslab earthquakes in the Cascadia subduction zone, in *The Cascadia Subduction Zone and Related Subduction Systems - Seismic Structure, Intraslab Earthquakes and Processes, and Earthquake Hazards*, edited by S. Kirby, K. Wang, and S. Dunlop, U.S. Geological Survey Open-File Report 02-328 and Geological Survey of Canada Open File 4350, pp. 43–45, 2002.

Symons, N., Seismic velocity structure of the Puget Sound region from 3-D non-linear tomography, Ph.D. thesis, University of Washington, 1998.

Thurber, C. H., Hypocenter-velocity structure coupling in local earthquake tomography, *Phys. Earth Plan. Int.*, *75*, 55–62, 1992.

Trehu, A. M., I. Asudeh, T. M. Brocher, J. H. Luetgert, W. D. Mooney, J. L. Nabelek, and Y. Nakamura, Crustal architecture of the Cascadia forearc, *Science*, *266*, 237–243, 1994.

Trehu, A. M., T. M. Brocher, K. C. Creager, M. A. Fisher, L. A. Preston, G. Spence, and the SHIPS98 Working Group, Geometry of the subducting Juan de Fuca plate: New constraints from SHIPS98, in *The Cascadia Subduction Zone and Related Subduction Systems - Seismic Structure, Intraslab Earthquakes and Processes, and Earthquake Hazards*, edited by S. Kirby, K. Wang, and S. Dunlop, U.S. Geological Survey Open-File Report 02-328 and Geological Survey of Canada Open File 4350, pp. 25–32, 2002.

Turcotte, D. L., and G. Schubert, *Geodynamics Applications of Continuum Physics to Geological Problems*, John Wiley and Sons, 1982.

U.S. Geological Survey, *The Universal Transverse Mercator (UTM) Grid*, Fact Sheet - U.S. Geological Survey, 2001.

van Wagoner, T. M., R. S. Crosson, K. C. Creager, G. F. Medema, L. A. Preston, N. P. Symons, and T. M. Brocher, Crustal structure and relocated earthquakes in the Puget

Lowland, Washington from high-resolution seismic tomography, *J. Geophys. Res.*, *107*, doi:10.1029/2001JB000,710, 2002.

VanDecar, J., M. Bostock, R. Crosson, and K. Creager, How does a subduction zone die? reconciling the dynamic and kinematic observations of Cascadia tectonic evolution, *EOS, Trans. Am. Geophys. Un.*, *74*, Fall Meeting Suppl., Abstract p. 92, 1993.

VanDecar, J. C., Upper-mantle structure of the Cascadia subduction zone from nonlinear teleseismic travel time inversion, Ph.D. thesis, University of Washington, 1991.

Vidale, J., Finite-difference calculation of traveltimes, *Bull. Seism. Soc. Am.*, *78*, 2062–2076, 1988.

Vidale, J., Finite-difference calculation of traveltimes in three dimensions, *Geophysics*, *55*, 521–526, 1990.

Wang, K., Unbending combined with dehydration embrittlement as a cause for double and triple seismic zones, *Geophys. Res. Lett.*, *29*, 1889, doi:10.1029/2002GL015,441, 2002.

Wang, K., T. Mulder, G. C. Rogers, and R. D. Hyndman, Case for very low coupling stress on the Cascadia subduction fault, *J. Geophys. Res.*, *100*, 12,907–12,918, 1995.

Wilson, D. S., The Juan de Fuca plate and slab: Isochron structure and Cenozoic plate motions, in *The Cascadia Subduction Zone and Related Subduction Systems - Seismic Structure, Intraslab Earthquakes and Processes, and Earthquake Hazards*, edited by S. Kirby, K. Wang, and S. Dunlop, U.S. Geological Survey Open-File Report 02-328 and Geological Survey of Canada Open File 4350, pp. 9–12, 2002.

Winter, J. D., *An Introduction to Igneous and Metamorphic Petrology*, Prentice Hall, 2001.

Zhao, D., T. Matsuzawa, and A. Hasegawa, Morphology of the subducting slab boundary in the northeastern Japan arc, *Phys. Earth Plan. Int.*, *102*, 89–104, 1997.

Zhao, D., M. Di, F. Ochi, and T. Seno, Dehydration and earthquakes of the Philippine Sea slab (2) Evidence from seismic tomography, *Abstr. Seism. Soc. Jpn.*, 2000.

Vita

Leiph Preston was born in Tulsa, Oklahoma. At Purdue University in West Lafayette, Indiana, he earned a Bachelor of Science degree in Physics. In 2003 he earned a Doctor of Philosophy at the University of Washington, Seattle in Geophysics.